Reducing the Societal Costs of Traumatic Brain Injury:

Astrocyte-Based Therapeutics and Functional Injury Tolerance of the Living Brain

Woo Hyeun Kang

Submitted in partial fulfillment of the
requirements for the degree of
Doctor of Philosophy
in the Graduate School of Arts and Sciences

COLUMBIA UNIVERSITY

2015

ABSTRACT

Reducing the Societal Cost of Traumatic Brain Injury: Astrocyte-Based Therapeutics and Functional Injury Tolerance of the Living Brain

Woo Hyeun Kang

Approximately 1.7 million traumatic brain injuries (TBI) occur annually in the United States, with an annual estimated societal cost of at least $76.5 billion. Addressing the growing TBI epidemic will require a multi-pronged approach: developing novel treatment strategies and enhancing existing preventative measures. The specific aims of this thesis are: (1) to modulate astrocyte activation as a potential therapeutic strategy post-TBI, (2) to determine the relationship between tissue deformation and alterations in electrophysiological function in the living brain, and (3) to investigate underlying mechanisms of functional changes post-TBI by utilizing stretchable microelectrode arrays (SMEAs).

In response to disease or injury, astrocytes become activated in a process called reactive astrogliosis. Activated astrocytes generate harmful radicals that exacerbate brain damage and can hinder regeneration of damaged neural circuits by secreting neuro-developmental inhibitors and glycosaminoglycans (GAGs). Since mechanically-activated astrocytes upregulate GAG production, delivery of GFP-TAT, a mock therapeutic protein conjugated to the cell-penetrating peptide TAT, increased significantly after activation. A TAT-conjugated peptide JNK inhibitor was delivered to activated astrocytes and significantly reduced activation. These results suggest a potentially new, targeted therapeutic utilizing TAT for preventing astrocyte activation with the possibility of limiting off-target, negative side effects.

While modulating astrocyte activation is a promising treatment strategy for TBI, effective therapeutic treatments are still lacking. Preventing TBI, by developing more effective safety systems, remains crucial. We determined functional tolerance criteria for the hippocampus and cortex based on alterations in electrophysiological function in response to controlled mechanical stimuli. Organotypic hippocampal and cortical slice cultures were mechanically injured at tissue strains and strain rates relevant to TBI, and changes in electrophysiological function were quantified. Most changes in electrophysiological function were dependent on strain and strain rate in a complex, nonlinear manner. Our results provide functional data that can be incorporated into finite element (FE) models to improve their biofidelity of accident and collision reconstructions.

TBI causes alterations in macroscopic function and behavior, which can be characterized by alterations in electrophysiological function in vitro. We utilized a novel in vitro platform for TBI research, the SMEA, to investigate the effects of TBI on pharmacologically-induced, long-lasting network synchronization in the hippocampus. Mechanical stimulation of organotypic hippocampal slice cultures significantly disrupted this network synchronization 24 hours after injury. Our results suggest that the ability of the hippocampal neuronal network to develop and sustain network synchronization was disrupted after mechanical injury, while also demonstrating the utility of the SMEA for TBI research.

Herein, we identified a novel therapeutic strategy for treating the deleterious effects of astrocyte activation post-TBI. We also developed tolerance criteria relating mechanical injury parameters to electrophysiological function, an important step in developing more accurate computational simulations of TBI. Equipping FE models with new information on the functional response of the living brain will enhance their biofidelity, potentially leading to improved safety

systems while reducing development costs. Finally, we utilized a novel in vitro TBI research platform, the SMEA, to investigate the effects of TBI on long-lasting network synchronization in the hippocampus. Compared to more labor intensive in vivo approaches, the ability of the SMEA to efficiently test TBI hypotheses within a single organotypic slice culture over extended durations could increase the speed of drug discovery through high-content screening. This multi-pronged approach is necessary to address the growing public health concern of TBI.

Table of Contents

List of Figures

List of Tables

List of Equations

1 Introduction

Traumatic brain injury (TBI) is a growing, global public health concern, affecting nearly 10 million people annually worldwide (Hyder *et al.*, 2007, Gean and Fischbein, 2010). In the United States alone, the incidence of TBI has risen from 1.4 million in 2002 (Langlois *et al.*, 2006, Elkin *et al.*, 2011b) to an estimated 1.7 million in 2006 (Faul *et al.*, 2010), with corresponding increases in emergency department visits (1.111 million to 1.365 million), hospitalizations (235,000 to 275,000), and deaths (50,000 to 52,000). Additionally, the societal cost of TBI in the United States, including medical costs and lost productivity, is estimated to have risen from $60 billion in 2000 to $76.5 billion in 2006 (Finkelstein *et al.*, 2006). Despite the worsening burden to society, treatment options for TBI remain relatively limited or ineffective (Exo *et al.*, 2009, Kolias *et al.*, 2013), while clinical trials for new therapies have been unsuccessful in mitigating the devastating secondary effects of TBI (Maas *et al.*, 1999, Maas *et al.*, 2010). The National Institute of Neurological Disorders and Stroke (NINDS) stressed the need to identify meaningful pathophysiological mechanisms of TBI, and more importantly, to generate drug candidates capable of specifically targeting these mechanisms (Narayan *et al.*, 2002). Due to their emerging role in the harmful secondary effects of TBI, astrocytes may be a promising therapeutic target, with the potential for fewer side effects compared to targeting neurons directly (Hamby and Sofroniew, 2010, Kimelberg and Nedergaard, 2010). New treatment and delivery strategies centered on glial-based targets could potentially lead to modulation of the cellular pathways involved in the secondary injury cascade of TBI.

However, in light of the struggles to develop effective drug therapeutics for TBI, efforts to prevent TBI remain central to reducing its societal costs (Hillary *et al.*, 2001, Nirula *et al.*,

2004, Moss *et al.*, 2014). Finite element (FE) models are useful tools in testing safety systems for the prevention of TBI (Aare *et al.*, 2004). Combined with FE models of automobiles or safety equipment, FE models of the brain have the potential to significantly reduce the cost of safety systems engineering by simulating and optimizing the injury-reducing performance of new designs before expensive prototypes need to be produced. The performance of new designs can be tested under a wide range of impact and loading scenarios before costly crash tests are performed, reducing the number of crash tests necessary. Ultimately, the optimized development and testing process could lead to safer cars and protective equipment, with shorter development cycles at reduced cost.

Currently, the outputs of FE models are capable of describing the mechanical events that occur during a TBI in human brain (Kleiven and Hardy, 2002, Takhounts *et al.*, 2003, Roth *et al.*, 2010), as well as in pig (Coats *et al.*, 2012) and rat brain (Lamy *et al.*, 2013, Mao *et al.*, 2013). However, developing effective and accurate FE models requires a fundamental understanding of injury mechanisms to translate the effects of mechanical stimuli to biologically relevant responses. For example, neuronal cell death is a major contributor to the devastating effects of TBI (Rink *et al.*, 1995, Clark *et al.*, 2000, Sato *et al.*, 2001, Stoica and Faden, 2010). Anatomical, region-specific tolerance criteria relating mechanical parameters of strain and strain rate to the biological outcome of cell death have been developed previously for TBI (Cater *et al.*, 2006, Elkin and Morrison, 2007). Adding cell death tolerance criteria data to existing FE models is the first step in making the models more biofidelic. However, loss of neuronal or glial cells alone cannot adequately describe the dysfunctional behavior of the brain after TBI (Lyeth *et al.*, 1990, D'Ambrosio *et al.*, 1998, Santhakumar *et al.*, 2000). The synaptic function of neurons within the electrophysiological circuitry of the brain continues to operate among the surviving

injured and dysfunctional neurons. Because functional changes based on electrophysiology cannot be explained solely by the post-traumatic death of neurons, quantification of functional deficits has the potential to provide unique information about the post-traumatic effects of mechanical injury.

1.1 Astrocyte Activation

In the healthy central nervous system (CNS), astrocytes contribute essential support for proper neuronal function (Falsig *et al.*, 2004, Sofroniew, 2005). When subjected to CNS insults, such as ischemia (Panickar and Norenberg, 2005, Barreto *et al.*, 2011), neurodegenerative disease (Eng and Ghirnikar, 1994, Maragakis and Rothstein, 2006), or trauma (Cullen *et al.*, 2007, Kim *et al.*, 2012), astrocytes become activated and undergo a phenotypic change characterized by proliferation, altered morphology, and increased gene expression, particularly for glial fibrillary acidic protein (GFAP) and vimentin (Fawcett and Asher, 1999, Pekny and Nilsson, 2005). Activated astrocytes are the principal component of the glial scar, a cellular barrier formed after CNS injury with both beneficial and detrimental effects (Ridet *et al.*, 1997, Rolls *et al.*, 2009). The glial scar is important for removing dead and damaged tissue, generating a barrier across the injured area to prevent the spread of damage, and shielding the damaged area from infectious agents (Stichel and Muller, 1998, Roitbak and Sykova, 1999, Silver and Miller, 2004). However, activated astrocytes within the glial scar also hinder regeneration and remyelination by increasing production of extracellular matrix (ECM) proteoglycans (Smith-Thomas *et al.*, 1994, Zhang *et al.*, 2006, Properzi *et al.*, 2008) and secreting harmful neuro-developmental inhibitors (Wada *et al.*, 1998a, Wanner *et al.*, 2008, Jones and Bouvier, 2014),

which negatively impact regeneration by preventing growth cone extension (McKeon *et al.*, 1991, McKeon *et al.*, 1995, Toy and Namgung, 2013). In addition, activated astrocytes generate radicals with the potential to damage neural cells, including superoxide, peroxides, and nitric oxide (NO), via upregulation of inducible nitric oxide synthase (iNOS) (Salvemini *et al.*, 1992, Molina *et al.*, 1998, Johnstone *et al.*, 1999) through activation of the mitogen-activated protein kinases (MAPKs) c-Jun N-terminal kinase (JNK), p38 MAPK and extracellular signal-regulated kinase (ERK) (Hua *et al.*, 2002).

1.2 Role of MAPK Signaling Pathways in Astrocyte Activation

Regulation of the MAPKs JNK, p38, and ERK may play a central role in astrocyte activation (Otani *et al.*, 2002, Guan *et al.*, 2006b, Hsiao *et al.*, 2007). These MAPKs are activated by a variety of stimuli, such as mechanical trauma (Mandell *et al.*, 2001, Raghupathi *et al.*, 2003), spinal cord injury (Crown *et al.*, 2006, Stirling *et al.*, 2008), ischemia and reperfusion (Namura *et al.*, 2001, Guan *et al.*, 2006a), and cytokine (Waetzig *et al.*, 2005, Munoz *et al.*, 2007) and lipopolysaccharide (LPS) stimulation (Bhat *et al.*, 1998, Nakajima *et al.*, 2004). Inhibition of MAPK cascades by the small molecule inhibitors of p38 (Piao *et al.*, 2003, Yoo *et al.*, 2008), JNK (Hua *et al.*, 2002, Guan *et al.*, 2006a), and ERK (Mandell *et al.*, 2001, Maddahi and Edvinsson, 2010) decreased the stimulated upregulation of iNOS *in vitro*.

Although specific inhibitors for p38, JNK, and ERK exist, they may act on downstream or upstream targets along the pathways, or act on other, non-target signaling pathways, with unknown consequences to astrocytes or unwanted off-target effects on other cell types within the brain. SB203580, commonly utilized as a specific inhibitor of p38-MAPK, is highly selective

not only for the p38 homologs p38α (Young *et al.*, 1997) and p38β (Kumar *et al.*, 1997), but also at least two non-p38 kinases as well: c-RAF and JNK2β1 (de Laszlo *et al.*, 1998). In terms of cell type specificity, SB203580 has been shown to regulate tumor necrosis factor-alpha (TNF-α), an inflammatory cytokine produced by astrocytes after injury, in different ways in human microglia and human astrocytes (Lee *et al.*, 2000). SP600125, a specific inhibitor of JNK, is highly selective for JNK1, -2, and -3 isoforms with >20-fold selectivity compared to a range of other kinases (Bennett *et al.*, 2001). However, SP600125 is not specific for any single JNK isoform, particularly JNK1, which has been implicated as the major mediator of iNOS induction in glial cells (Pawate and Bhat, 2006). In addition, SP600125 has also been found to partially inhibit p38-MAPK (Bennett *et al.*, 2001). U0126 blocks the activation of ERK by selectively inhibiting the upstream MAP kinase kinases MEK1 and MEK2 (Favata *et al.*, 1998), but does not act directly on ERK. The non-specificity and potential for off-target effects limit the utility of small molecule inhibitors of p38, JNK, and ERK as effective therapeutics in mitigating the harmful effects of astrocyte activation.

1.3 Glycosaminoglycans and TAT Transduction

Much of the negative effects of astrocyte activation are associated with the increased production of glycosaminoglycans (GAG) and NO, among other changes in their physiology. Increased production of extracellular GAG is known to be inhibitory to neurite outgrowth (Verna *et al.*, 1989, Fernaud-Espinosa *et al.*, 1994). GAGs form a significant component of the glial scar and cause growth cone collapse, preventing regeneration (Dou and Levine, 1995). Increased expression of iNOS (Lee *et al.*, 1995), and the subsequent over-production of NO (Wada *et al.*,

1998a, Wada *et al.*, 1998b), can cause cell death due to subsequent nitrosylation of proteins (Wada *et al.*, 1998b). Preventing significant increases in GAG and NO levels as a result of astrocyte activation after TBI, or downregulating harmful levels of GAG and NO back to pre-injury levels after TBI, may be beneficial in controlling the detrimental consequences of astrocyte activation after TBI. Small molecule inhibitors of the MAPK signaling pathways implicated in astrocyte activation are not effective as therapies for the reasons stated above. Therefore, a targeted therapeutic, specific for only activated astrocytes, may be necessary for successful clinical translation.

The cell-penetrating peptide (CPP) from the transactivator of transcription (TAT) protein of human immunodeficiency virus (HIV-1) is known to cross cell plasma membranes (Frankel and Pabo, 1988, Green and Loewenstein, 1988). Whereas the 86 amino acid, full length HIV-1 TAT has been implicated in neurodegeneration and neuroinflammation (Williams *et al.*, 2009), the CPP TAT (hereafter referred to as TAT-peptide) is an 11 amino acid peptide which is non-toxic, non-inflammatory, and capable of cellular transduction (Vives *et al.*, 1997). The TAT-peptide is believed to transduce across cell plasma membranes via an electrostatic interaction with cell surface proteoglycans (Tyagi *et al.*, 2001, Brooks *et al.*, 2005). Previously, we reported that the transduction efficiency of TAT-peptide is dependent on cellular GAG content (Simon *et al.*, 2009). By taking advantage of increased GAG levels due to astrocyte activation after TBI, it may be possible to deliver a TAT-conjugated therapeutic cargo to modulate astrocyte activation after TBI. This delivery strategy also has the potential of specificity for activated astrocytes, limiting unwanted off-target effects of less specific therapeutics.

1.4 Functional Tolerance Criteria

The development of improved preventative measures against TBI first requires identification of tolerance criteria, or the maximum safe stress or strain for a given tissue (Zhang *et al.*, 2004, Yao *et al.*, 2007). Because brain tissue is a viscoelastic material, its biological response to mechanical trauma may be dependent on the dynamic properties of the applied mechanical stimulus, *e.g.* strain and strain rate (Arbogast and Margulies, 1998, Thibault and Margulies, 1998, Darvish and Crandall, 2001, Prange and Margulies, 2002). Previous studies suggest that TBI is the result of brain tissue deformation in excess of 10% strain at strain rates greater than 10 s^{-1} (Margulies *et al.*, 1990, Margulies and Thibault, 1992, Meaney *et al.*, 1995, Morrison *et al.*, 1998, Morrison *et al.*, 2003). Work performed previously in our group supported these hypotheses by assessing cell death criteria for the hippocampus (Cater *et al.*, 2006) and cortex (Elkin and Morrison, 2007). These previous studies demonstrated that cell response was dependent on the specific parameters of the applied mechanical stimulus.

Although TBI is known to cause cell death within specific brain regions (Hicks *et al.*, 1993, Raghupathi *et al.*, 2002), cell death does not always correlate with functional deficits and *vice versa* (Gurkoff *et al.*, 2006, Browne *et al.*, 2011, Khuman *et al.*, 2011). Because functional alterations based on electrophysiological function cannot be explained solely by the post-traumatic death of neurons, quantification of functional deficits has the potential to provide unique information about the post-traumatic effects of mechanical injury. TBI has been shown to cause alterations in intracellular signaling cascades (Dash *et al.*, 2002, Mori *et al.*, 2002, Atkins *et al.*, 2007a, Atkins *et al.*, 2009, Dash *et al.*, 2011), receptor subunit expression (Kumar *et al.*, 2002, Osteen *et al.*, 2004, Giza *et al.*, 2006, Kharlamov *et al.*, 2011), receptor function (Zhang *et al.*, 1996, Tavalin *et al.*, 1997, Lea *et al.*, 2002), and neuron morphology (Saatman *et al.*, 1998, Posmantur *et al.*, 2000, Schwarzbach *et al.*, 2006, Gao and Chen, 2011, Gao *et al.*,

2011), all of which affect function of neurons in the absence of significant cell death. The cumulative effect of these more subtle changes can be measured and quantified by electrophysiological measures of neuronal network function.

Once functional tolerance criteria of living brain are determined, predictive mathematical functions describing the region-specific electrophysiological response of brain tissue to precisely controlled mechanical stimuli can be generated to equip next-generation FE models of TBI (Takhounts *et al.*, 2008). Currently, FE models of the head exist that can predict tissue deformation in response to traumatic mechanical loads (Willinger *et al.*, 1999, Zhang *et al.*, 2001a, Zhang *et al.*, 2001b, Kleiven and Hardy, 2002, Mao *et al.*, 2006), but are not equipped to predict the tissue's biological response, *i.e.* brain tissue function as it relates to electrophysiological function. Equipping FE models with data sets of functional information, in addition to existing data sets of material properties and cell death, will enhance the predictive capability of existing FE models.

1.5 Microelectrode Arrays

The interface between electronic circuitry and neural tissue or cells is most often achieved through a matrix or array of electrodes. By recording from many electrodes simultaneously, the information content of the neural signal is greatly increased over that of single electrodes (Mehring *et al.*, 2003, Cohen and Nicolelis, 2004, Carmena *et al.*, 2005). Given the distributed processing and storage of information in the brain, recording from an extended network of interacting neurons may be more effective at capturing the dynamics of large neuronal populations and functional assemblies of neurons that are activated in a

coordinated manner than single electrode interfaces (Engel *et al.*, 2001, Harris *et al.*, 2003). Unlike single electrode recordings, the long-range connectivity of neural networks can be studied with these electrode arrays due to their ability to simultaneously record from multiple sites, providing insight into neuronal information processing and function (Kralik *et al.*, 2001, Diogo *et al.*, 2003). Contemporary multielectrode arrays (MEAs) allow for simultaneous recording from up to 256 discrete locations with recording bandwidths of up to 30 kHz (Charvet *et al.*, 2010). Higher order behaviors are likely to depend on this type of ensemble network behavior rather than the activity of individual neurons (Deadwyler and Hampson, 1995, Doetsch, 2000).

To facilitate coupling of MEAs to neural tissue and the study of neuronal networks, a multitude of MEA concepts and designs have been applied to *in vivo* neural tissue, *in vitro* cell culture, and brain slice electrophysiology. Electrodes have been fabricated from many materials including gold, platinum, iridium, titanium nitride, silicon, carbon, and conductive polymers (Nisch *et al.*, 1994, Thiebaud *et al.*, 1999, Yu *et al.*, 2007). Planar electrodes patterned on flat, most often rigid substrates are designed for extracellular stimulation and recording *in vitro* of various types of tissues or cells (Oka *et al.*, 1999, Yu and Morrison, 2010).

Material	**Young's Modulus (E)**
Brain	3 kPa (Elkin *et al.*, 2011a, Elkin *et al.*, 2011b)
Peripheral Nerve	575 kPa (Borschel *et al.*, 2003)
Spinal Cord	650 kPa (Bilston and Thibault, 1996)
Polydimethylsiloxane (PDMS)	1 MPa (Walker *et al.*, 2004)
Polyimide	2.8 GPa (McClain *et al.*, 2011)

Parylene C	4.8 GPa (Shih *et al.*, 2004)
Bone	16 GPa (Rho *et al.*, 1993)
Thin-film Gold	55 GPa (Espinosa and Prorok, 2003)
Glass	76 GPa (Chen *et al.*, 1995)
Platinum	165 GPa (Merker *et al.*, 2001)
Silicon	170 GPa (Hopcroft *et al.*, 2010)

Table 1.1 Typical Young's modulus (E) for SMEA materials and neural tissues.

Less rigid arrays for *in vivo* implantation that integrate stiff components on flexible polymer substrates such as polyimide have been developed but with Young's modulus (E) of approximately 3 GPa (Cheung *et al.*, 2007). Small flexion of these flexible MEAs can be achieved without altering their functionality (Suo *et al.*, 1999). However, even these flexible MEAs are much stiffer than neural tissues and cannot withstand mechanical strains in excess of 1-2% (Pashley, 1960, Chiu *et al.*, 1994, Spaepen, 2000, Lacour *et al.*, 2010). Flexible MEAs are not compliant enough to tolerate the large mechanical deformations necessary to induce TBI (Morrison *et al.*, 1998, Cater *et al.*, 2006, Elkin and Morrison, 2007, Hyder *et al.*, 2007). The modulus mismatch between rigid MEAs (E of tens to hundreds of GPa), flexible MEAs (E on the order of GPa) (McClain *et al.*, 2011), and brain tissue (E of approximately 3 kPa) (Elkin *et al.*, 2011a, Elkin *et al.*, 2011b) poses many acute and chronic problems, stemming from implantation trauma, interfacial strains, and micromotion damage (Biran *et al.*, 2005, Polikov *et al.*, 2005, Subbaroyan *et al.*, 2005, Cheung *et al.*, 2007) (Table 1.1).

1.6 Stretchable Microelectrode Arrays as an *In Vitro* Platform for TBI Research

Stretchable MEAs (SMEAs) have utility for *in vitro* studies to understand mechanotransduction, the cellular pathways by which mechanical stimuli are transduced into intracellular signaling cascades. Many of these *in vitro* systems apply mechanical stimulation by deformation (stretch) of an elastic substrate on which the cells or tissue grow. Such systems have found utility in the study of TBI (Morrison *et al.*, 1998, Hyder *et al.*, 2007), which is caused by rapid deformation of the brain, including stretch, compression, and shear strain (Cater *et al.*, 2006, Elkin and Morrison, 2007). As described above, most contemporary MEAs are rigid and therefore not compatible with these injury models, making it difficult to study the effects of mechanical injury on electrophysiological function of the neuronal network. While it is possible to injure neural tissue after removing it from an MEA, recording from the same locations and the same population of neurons after injury would be challenging. An SMEA embedded in the elastic substrate lifts these limitations because the tissue remains adhered to the SMEA before, during, and after stretch injury (Yu *et al.*, 2009a). In addition, long-term studies involving multiple electrophysiological recordings within the same tissue slice is made possible due to the ability to maintain culture sterility.

1.7 Significance

Traumatic brain injury (TBI) is a growing, global public health concern, affecting nearly 10 million people annually worldwide (Hyder *et al.*, 2007, Gean and Fischbein, 2010). In the United States alone, the incidence of TBI continues to rise, from 1.4 million in 2002 (Langlois *et al.*, 2006, Elkin *et al.*, 2011b) to 1.7 million in 2006 (Faul *et al.*, 2010), with corresponding

increases in emergency department visits (1.111 million to 1.365 million), hospitalizations (235,000 to 275,000), and deaths (50,000 to 52,000). The societal cost of TBI in the United States, including medical costs and loss of productivity, continues to rise as well, from $60 billion in 2000 to $76.5 billion in 2006 (Finkelstein *et al.*, 2006).

Despite the rising incidence and worsening burden to society of TBI, drug treatment options remain limited or ineffective, with all drug candidates failing in clinical trials (Reinert and Bullock, 1999, Georgiou and Manara, 2013, Li *et al.*, 2014). A major challenge of small molecule therapeutics for TBI remains the lack of specificity to particular neural cell types, while novel protein-based therapeutics suffer from the inability to overcome the barrier of the cellular membrane. Additionally, the National Institute of Neurological Disorders and Stroke (NINDS) stressed the need to identify meaningful pathophysiological mechanisms of TBI, and more importantly, to generate drug candidates capable of specifically targeting these mechanisms (Narayan *et al.*, 2002). Delivering drugs that act on specific intracellular signaling pathways, with reduced side effects, could be an effective strategy to ameliorate the deleterious secondary effects of TBI. As astrocytes have emerged as more than just neuronal support cells, they may be a promising therapeutic target due to the potential for fewer side effects compared to targeting neurons directly (Choo *et al.*, 2013).

Due to the paucity of effective drug therapeutics for TBI, improving safety measures and protective equipment will be paramount to reducing the frequency and severity of TBI. In combination with FE models of automobiles or safety equipment, FE models of the brain have the potential to significantly reduce the cost of safety systems engineering by enabling the simulation and optimization of new safety designs before expensive prototypes need to be produced. The injury reducing performance of new safety designs under a wide range of impact

and loading scenarios can be computationally modeled and assessed before expensive crash tests are performed, reducing the number of crash tests necessary. Quantifying alterations in the electrophysiology of brain tissue after mechanical injury, and developing mathematical equations capable of predicting this behavior, will equip FE models of the brain with new information on the functional response of the living brain to precise injury parameters, in addition to existing data on material properties and cell death. The functional data will enhance the accuracy of FE models, potentially leading to improved safety systems at reduced cost.

TBI results in brain dysfunction, a consequence of brain tissue deformation. Brain tissue strain and strain rate are significant predictors of injury in the brain after TBI (Cater *et al.*, 2006, Elkin and Morrison, 2007). Thus, a research platform that can combine mechanical injury with functional outcomes will be helpful in elucidating TBI pathology. SMEAs have potential as a new *in vitro* platform for TBI research within a single package. SMEAs represent the convergence of multiple paradigms of neurophysiology relevant to TBI: electrophysiology, mechanical stimulation, pharmacological intervention, and temporal development. The ability to perform robust experiments involving multiple research paradigms within the same tissue slice will enable the investigation of TBI mechanisms and pathologies that have previously been difficult, potentially boosting the rate of novel drug therapeutic screening and discovery.

2 Attenuation of Astrocyte Activation by TAT-Mediated Delivery of a Peptide JNK Inhibitor[1]

2.1 Introduction

In the healthy central nervous system (CNS), astrocytes contribute essential support for proper neuronal function (Falsig *et al.*, 2004, Sofroniew, 2005). When subjected to insults, such as ischemia, neurodegenerative disease, or trauma, astrocytes become activated and undergo a phenotypic change characterized by proliferation (Dong and Benveniste, 2001, Sofroniew, 2005), altered morphology (Laird *et al.*, 2008), and increased gene expression, particularly for glial fibrillary acidic protein (GFAP) and vimentin (Pekny and Nilsson, 2005). Activated astrocytes are important for removing dead and damaged tissue, generating a barrier across the injured area to prevent the spread of damage, and shielding the dam[1]aged area from infectious agents (Stichel and Muller, 1998, Silver and Miller, 2004, Sofroniew, 2005). However, activated astrocytes also hinder regeneration and remyelination by increasing production of extracellular matrix (ECM) proteoglycans to form a glial scar (Smith-Thomas *et al.*, 1994, Zhang *et al.*, 2006, Properzi *et al.*, 2008) and secreting harmful neuro-developmental inhibitors (Chung and Benveniste, 1990, Aloisi *et al.*, 1992, Wada *et al.*, 1998a, Zhang *et al.*, 2006, Wanner *et al.*, 2008), which negatively impact regeneration by preventing growth cone extension (McKeon *et al.*, 1991, Smith-Thomas *et al.*, 1994, McKeon *et al.*, 1995). In addition, activated astrocytes generate radicals with the potential to damage neural cells, including superoxide, peroxides, and nitric oxide (NO), via upregulation of inducible nitric oxide synthase (iNOS) (Salvemini *et al.*,

[1] A modified version of this chapter previously appeared in print: Kang, W.H., Simon, M.J., Gao, S., Banta, S. and Morrison, B. (2011). Attenuation of Astrocyte Activation by TAT-Mediated Delivery of a Peptide JNK Inhibitor. J Neurotrauma 28, 1219-1228. Reprinted with permission by Mary Ann Liebert, Inc.

1992, Molina *et al.*, 1998, Johnstone *et al.*, 1999, Laird *et al.*, 2008) through activation of the mitogen-activated protein kinases (MAPKs) c-Jun N-terminal kinase (JNK), p38 MAPK and extracellular signal-regulated kinase (ERK) (Hua *et al.*, 2002).

We hypothesized that activated astrocytes could be targeted by the cell-penetrating peptide (CPP) from the transactivator of transcription (TAT) protein from the human immunodeficiency virus (HIV-1) through their increased expression of glycosaminoglycans (GAGs), since the first step in TAT transduction is an electrostatic interaction with the cell surface (Tyagi *et al.*, 2001, Brooks *et al.*, 2005). The CPP TAT is non-toxic and non-inflammatory (Vives *et al.*, 1997) unlike the full-length TAT protein (Williams *et al.*, 2009). Cultured astrocytes were activated with a well-characterized *in vitro* mechanical stretch injury model (Morrison *et al.*, 2003), the proinflammatory cytokine interleukin (IL)-1β, or lipopolysaccharide (LPS). Activation was measured via functional changes, specifically production of nitrite, the oxidation product of NO (Murphy *et al.*, 1993) and GAG content. We observed significant increases of nitrite and GAG content in mechanically and chemically stimulated astrocytes and an increase in green fluorescence protein (GFP)-TAT transduction. Inhibition of JNK, p38 MAPK, or ERK pathways by small molecule inhibitors significantly reduced activation and significantly decreased GFP-TAT transduction. TAT-mediated delivery of a JNK peptide inhibitor to mechanically or chemically stimulated astrocytes significantly prevented activation. Our results highlight the potential of TAT-mediated cargo delivery to target activated astrocytes, to deliver a biologically active cargo, and to directly modify the gliotic response to activating stimuli. Such a strategy could hold therapeutic benefit for multiple CNS diseases and injury.

2.2 Materials and Methods

2.2.1 Cell Culture

All protocols involving animals were approved by the Columbia University IACUC. Purified astrocyte cultures were prepared as previously reported (Simon *et al.*, 2009). Briefly, cortices of 8- to 10-day old Sprague-Dawley rat pups were digested with papain, triturated, and plated into T75 tissue culture flasks. After 1 h incubation, the flasks were vigorously shaken to remove non-adherent cells, and the media was discarded. The enriched astrocytes (> 90%) were grown in DMEM (Sigma-Aldrich, St. Louis, MO) with 10% heat-inactivated newborn calf serum, 1 mM glutamine, 10mM HEPES and 10 mg/mL gentamicin for 2 weeks as previously described (Simon *et al.*, 2009, Li *et al.*, 2010a). The astrocytes were then treated with trypsin/EDTA (Sigma/Aldrich, St. Louis, MO) for 5 min and replated onto either uncoated, tissue culture 24-well plates at a density of 30,000 cells per well or onto highly stretchable, silicone membranes (Specialty Manufacturing Inc., Saginaw, MI) coated with laminin, poly-D-lysine, and gelatin attached to custom-made stainless steel wells at a density of 5,000 cells per cm^2 (Morrison *et al.*, 2003). The astrocytes were then cultured for an additional 2 days before experimentation.

2.2.2 Mechanical Stretch Injury of Astrocytes

Astrocytes on silicone membranes were subjected to a single 30% equi-biaxial stretch injury at a strain rate of 20 s^{-1} using a well-characterized stretch injury device (Morrison *et al.*, 2003). These injury parameters were chosen to induce a moderate level of injury (Cater *et al.*, 2006). Strain and strain rate were verified with high speed video analysis (Cater *et al.*, 2006).

The cells were analyzed for nitrite, GAG, DNA or GFP-TAT transduction 48 h following injury (*vide infra*).

2.2.3 Chemical Stimulation of Astrocytes

Astrocytes were stimulated with 20 ng/mL murine IL-1β (Invitrogen, Carlsbad, CA) or 2 μg/mL LPS (Sigma-Aldrich, St. Louis, MO) for 48 h. Cells were analyzed for nitrite, GAG, DNA or GFP-TAT transduction.

2.2.4 Inhibition of Mechanical Activation

To verify the involvement of MAPK pathways in astrocyte activation in response to mechanical stretch injury, astrocytes were pretreated for 1 h (Hua *et al.*, 2002) with either 20 μM (Nakajima *et al.*, 2004, Yoo *et al.*, 2008) SB203580 (Sigma), SP600125 (Sigma), or U0126 (Sigma) to inhibit specific MAPK according to previously published methods (Hua *et al.*, 2002, Nakajima *et al.*, 2004, Yoo *et al.*, 2008). A pretreatment paradigm was utilized to confirm involvement of specific pathways and not to demonstrate therapeutic potential. For the TAT-JNK inhibitor delivery studies, astrocytes were treated with either 3 μM TAT-JNK inhibitor (Axxora, San Diego, CA), L-TAT control peptide (Axxora, San Diego, CA), GFP-TAT, or the TAT peptide utilized in our previous study (Gao *et al.*, 2009) (hereafter referred to as mTAT) immediately following mechanical injury to more closely model a post-injury treatment paradigm. The half maximal inhibitory concentration (IC_{50}) of the TAT-JNK inhibitor is 1 μM as previously determined from JNK inhibition assays *in vitro* (Borsello *et al.*, 2003). The

concentration of the TAT-JNK inhibitor necessary for sufficient intracellular inhibition was based on previous delivery studies of GFP-TAT (Gao *et al.*, 2009, Simon *et al.*, 2009). The inhibitors then remained within the medium until nitrite, GAG, DNA or GFP-TAT transduction was quantified at 48 h.

2.2.5 Inhibition of Chemical Activation

To verify the involvement of the MAPK pathways in astrocyte activation in response to chemical stimuli, astrocytes were pretreated for 1 h (Hua *et al.*, 2002) with either 20 μM (Nakajima *et al.*, 2004, Yoo *et al.*, 2008) SB203580 (Sigma), SP600125 (Sigma), or U0126 (Sigma) to inhibit specific MAPK before chemical stimulation with either 20 ng/mL murine IL-1β (Kim *et al.*, 2006) (Invitrogen, Carlsbad, CA) or 2 μg/mL LPS (Nakajima *et al.*, 2004) (Sigma-Aldrich, St. Louis, MO). These pretreatment paradigms have been used before to verify the involvement of MAPK cascades in chemically mediated astrocyte activation (Hua *et al.*, 2002, Nakajima *et al.*, 2004, Kim *et al.*, 2006, Yoo *et al.*, 2008). For the TAT-JNK inhibitor delivery studies, astrocytes were chemically stimulated as above and either 3 μM TAT-JNK inhibitor (Axxora, San Diego, CA), L-TAT control peptide (Axxora, San Diego, CA), GFP-TAT or mTAT was added concurrently. The chemical stimulators and inhibitors then remained within the medium until nitrite, GAG, DNA or GFP-TAT transduction was quantified at 48 h.

2.2.6 Quantification of Nitrite

Nitrite production was chosen as a functional measure of astrocyte activation, specifically as a surrogate marker of NO overproduction as a result of iNOS expression, which is known to exacerbate brain injury (Wada *et al.*, 1998b). Nitrite content was quantified 48 h after astrocyte activation because previous studies have shown that iNOS expression, NO production and hence nitrite content are robustly increased at this time point (Yoo *et al.*, 2008). Nitrite content was measured in triplicate for each well using the Griess reagent (Invitrogen). Equal volumes of N-(1-naphthyl)ethylenediamine and sulfanilic acid were mixed together to form the Griess reagent. 150 µL of cell supernatant or $NaNO_2$ standard was mixed with 130 µL of deionized water and 20 µL of Griess reagent in a 96-well plate. After 30 min incubation in the dark at room temperature, sample absorbance was measured in a spectrophotometric microplate reader (Molecular Devices) at 548 nm and converted to nitrite content with the standards. Nitrite content was normalized to total DNA content using the Quant-iT Picogreen dsDNA assay (Invitrogen). For the inhibitor studies, the average µmol nitrite/ng DNA was normalized to the average µmol nitrite/ng DNA in uninjured or unstimulated, control cells to account for any basal effects of inhibitors on unactivated cells.

2.2.7 Quantification of GAG

Cellular GAG content was quantified 48 h after astrocyte activation as previous studies have shown that GAG production is consistently increased at this time point after activation *in vitro* (Smith-Thomas *et al.*, 1994, Zhang *et al.*, 2006, Properzi *et al.*, 2008). Increased GAG production as a result of injury has been shown to be inhibitory to neurite outgrowth and recovery (Smith-Thomas *et al.*, 1994). To determine cellular GAG content, cells were incubated

in 500 μL of lysis buffer (0.1 M sodium acetate buffer, pH 5, containing 5 mM EDTA, 5 mM cysteine HCl, and 0.6 U papain/mL) overnight at 37°C. Cells were sonicated and analyzed using the 1,9-dimethylmethylene blue (DMMB, Sigma) dye-binding assay and compared to prepared GAG standards (Farndale *et al.*, 1986). GAG content was normalized to total DNA content using the Quant-iT Picogreen dsDNA assay (Invitrogen). For the inhibitor studies, the average μg GAG/ng DNA was normalized to the average μg GAG/ng DNA in uninjured, unstimulated, control cells to account for basal effects of MAPK inhibitors on unactivated cells.

2.2.8 Quantification of Protein Transduction into Primary Astrocytes

The GFP-TAT construct has been described previously and consisted of an 11 amino acid peptide flanked by glycines (GYGRKKRRQRRRG) fused to the C-terminus of the GFP protein (Simon *et al.*, 2009). Protein transduction of GFP or GFP-TAT was quantified in triplicate as previously reported (Gao *et al.*, 2009, Simon *et al.*, 2009). Briefly, astrocyte cultures were incubated with either 3 μM GFP or GFP-TAT for 4 h, as our previous studies have demonstrated that this duration and concentration yielded maximal uptake of the constructs (Gao *et al.*, 2009). Cells were washed in PBS and treated with trypsin/EDTA (Sigma) for 5 min to remove protein bound to the surface of the cells, centrifuged, and resuspended in 250 μL PBS. Protein transduction was quantified with a FACSCanto II flow cytometer (Becton Dickinson) by calculating the percent increase in geometric mean fluorescence (excitation 488 nm, emission 530/30 nm) above that of cells treated with GFP only, to account for GFP and background autofluorescence. For the inhibitor studies, the average fold change of each injured or stimulated, experimental group was normalized to the average fold change of uninjured or

unstimulated groups to account for any basal effects of inhibitors on unactivated cells. A total of 10,000 events per sample were counted.

2.3 Results

2.3.1 Mechanical Activation of Astrocytes

Mechanical stretch significantly increased nitrite content after injury compared to uninjured controls (Figure 2.1A). GAG content increased significantly after injury compared to uninjured controls (Figure 2.1B). Mechanical injury increased GFP-TAT transduction more than twofold compared to uninjured controls (Figure 2.1C). These results indicate that our *in vitro* model of stretch injury activated astrocytes, and that GFP-TAT preferentially transduced activated astrocytes.

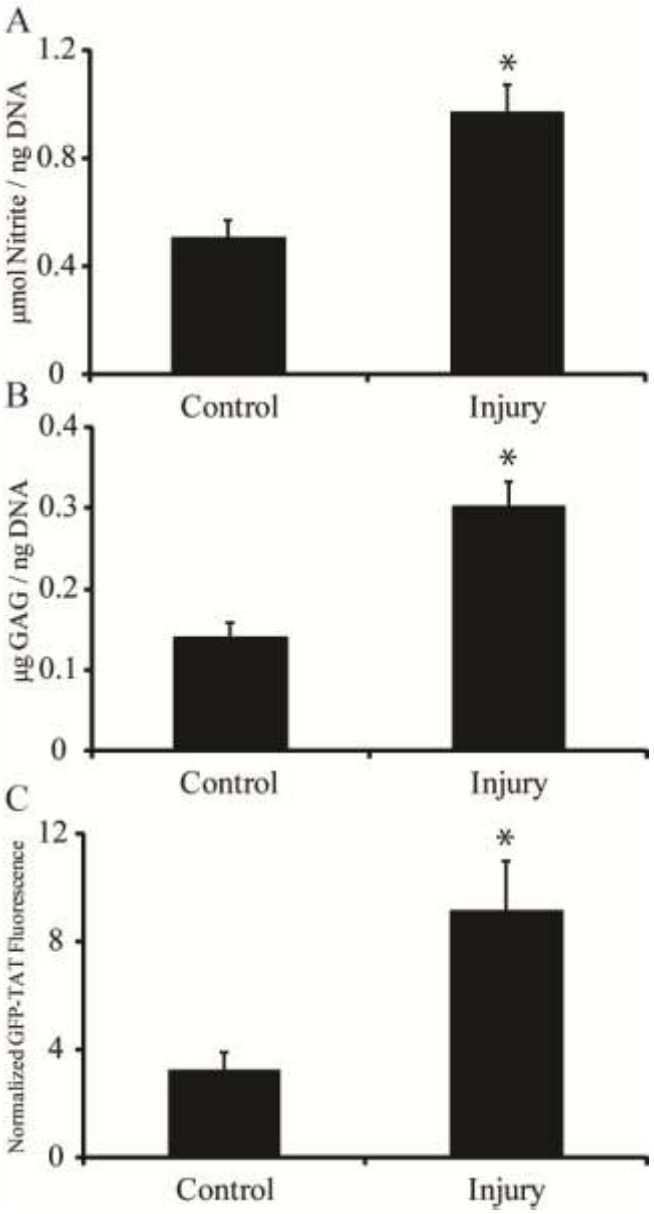

Figure 2.1 Effects of mechanical stretch injury. (**A**) Nitrite content, normalized to DNA content, increased significantly in stretch-injured astrocytes compared to uninjured controls ($n \geq 26$). (**B**) GAG content, normalized to DNA content, increased significantly in injured astrocytes compared to uninjured controls ($n \geq 26$). (**C**) GFP-TAT transduction increased significantly in stretch-injured astrocytes compared to uninjured controls ($n \geq 10$; $^*p < 0.05$; mean ± standard error of the mean; GFP-TAT, green fluorescence protein-transactivator of transcription; GAG, glycosaminoglycans).

2.3.2 IL-1β and LPS Activation of Astrocytes

Both IL-1β and LPS treatment significantly increased nitrite content of astrocyte cultures compared to untreated controls (Figure 2.2A). GAG content increased significantly in IL-1β and LPS treated astrocytes compared to untreated controls (Figure 2.2B). In both IL-1β and LPS stimulated astrocytes, GFP-TAT transduction increased significantly compared to untreated controls (Figure 2.2C) indicating that GFP-TAT preferentially transduced activated astrocytes.

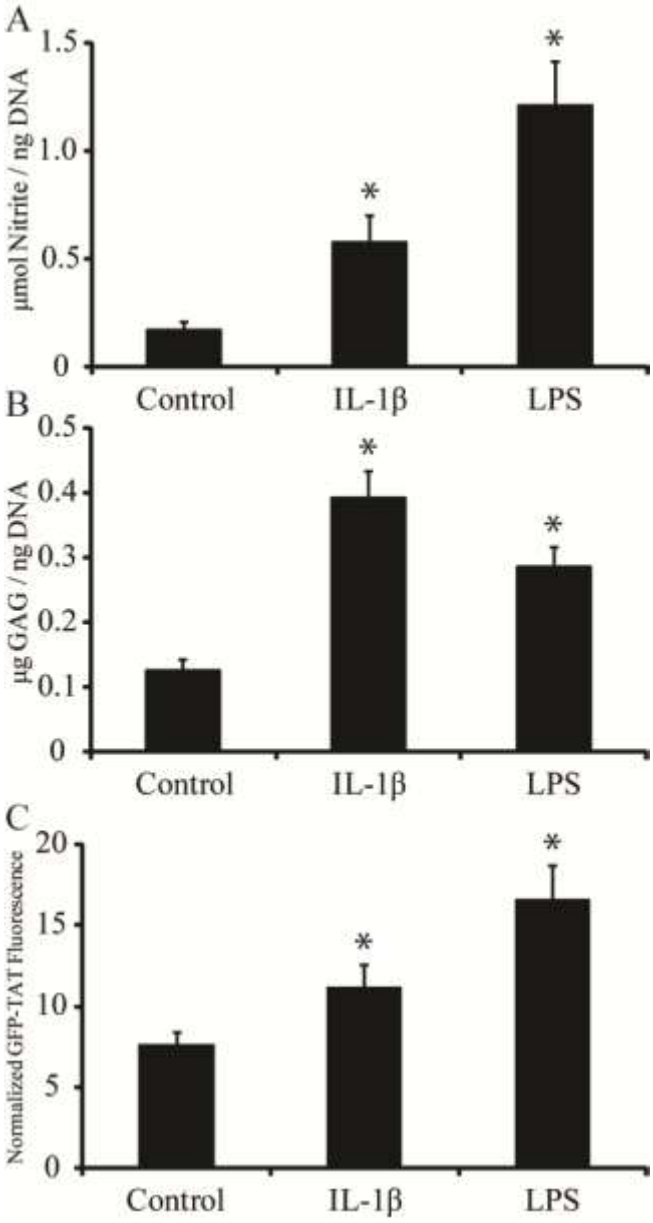

Figure 2.2 Cytokine and LPS-mediated activation of astrocytes. (**A**) Both IL-1β and LPS treatment significantly increased nitrite content, normalized to DNA content ($n \geq 31$). (**B**) GAG content increased significantly after IL-1β and LPS stimulation ($n \geq 30$). (**C**) GFP-TAT transduction increased significantly after IL-1β or LPS treatment ($n \geq 18$; $^*p < 0.05$ compared to vehicle-treated, unstimulated cultures; mean ± standard error of the mean; IL-1β, interleukin IL-1β; LPS, lipopolysaccharide; GAG, glycosaminoglycans; GFP-TAT, green fluorescence protein-transactivator of transcription).

2.3.3 Inhibition of Mechanical Activation via MAPK Antagonism

Pretreatment of astrocytes with either 20 μM of SB203580, SP600125 or U0126 for 1 h before mechanical injury significantly attenuated nitrite production (Figure 2.3A). GAG content in injured astrocytes was also decreased significantly after pretreatment with either SB203580, SP600125 or U0126 (Figure 2.3B). GFP-TAT transduction was significantly reduced in injured astrocytes pretreated with MAPK inhibitors compared to untreated, injured astrocytes (Figure 2.3C).

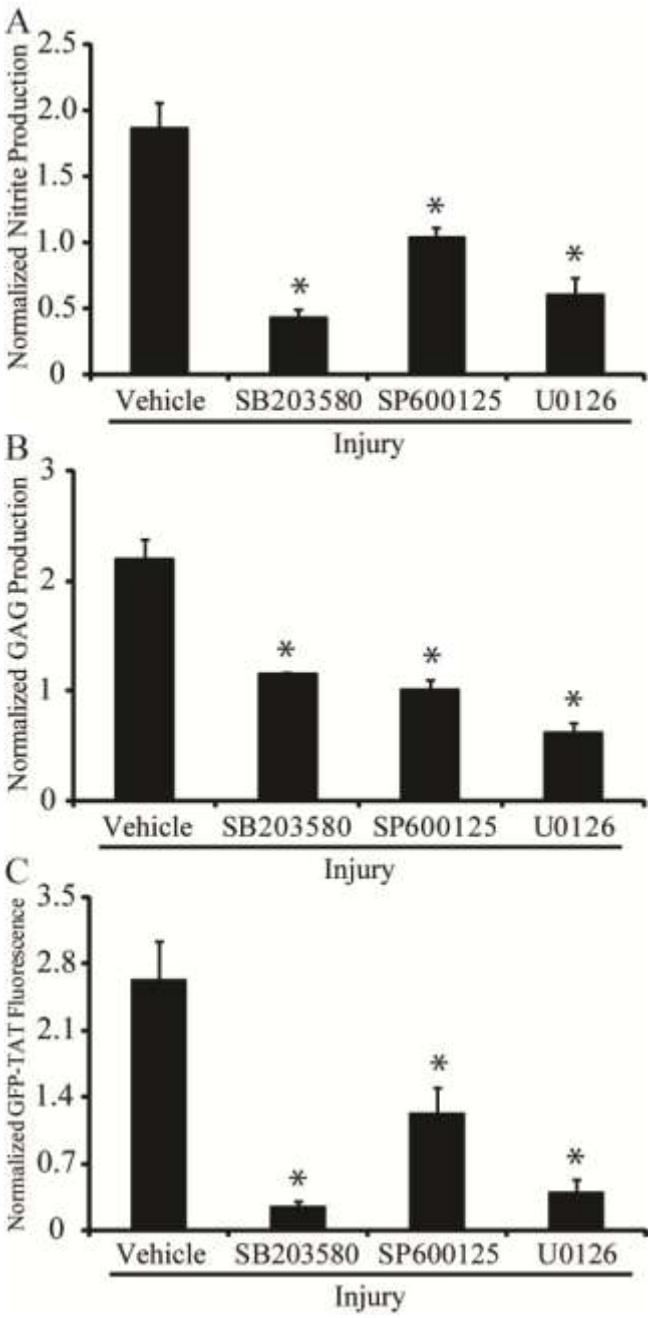

Figure 2.3 Effect of MAPK inhibition on mechanical activation. (**A**) The post-traumatic increase of nitrite content was significantly attenuated by MAPK inhibition ($n \geq 3$). (**B**) The post-traumatic increase of GAG content was significantly attenuated by MAPK inhibition ($n \geq 3$). (**C**) The increase in post-traumatic GFP-TAT transduction was attenuated by MAPK inhibition ($n \geq 4$; $^*p < 0.05$ compared to

injured, vehicle-treated cultures; mean ± standard error of the mean; MAPK, mitogen-activated protein kinase; GAG, glycosaminoglycans; GFP-TAT, green fluorescence protein-transactivator of transcription).

2.3.4 Inhibition of IL-1β and LPS Activation via MAPK Antagonism

After IL-1β or LPS stimulation, nitrite content was significantly decreased by MAPK inhibition with either SB203580, SP600125, or U0126 compared to stimulated cultures receiving vehicle (Figure 2.4A, D). GAG content was significantly reduced in chemically stimulated cultures pretreated with either SB203580, SP600125, or U0126 compared to vehicle treated cultures (Figure 2.4B, E). GFP-TAT transduction was significantly decreased in IL-1β and LPS stimulated astrocytes pretreated with either SB203580, SP600125, or U0126 (Figure 2.4C, F).

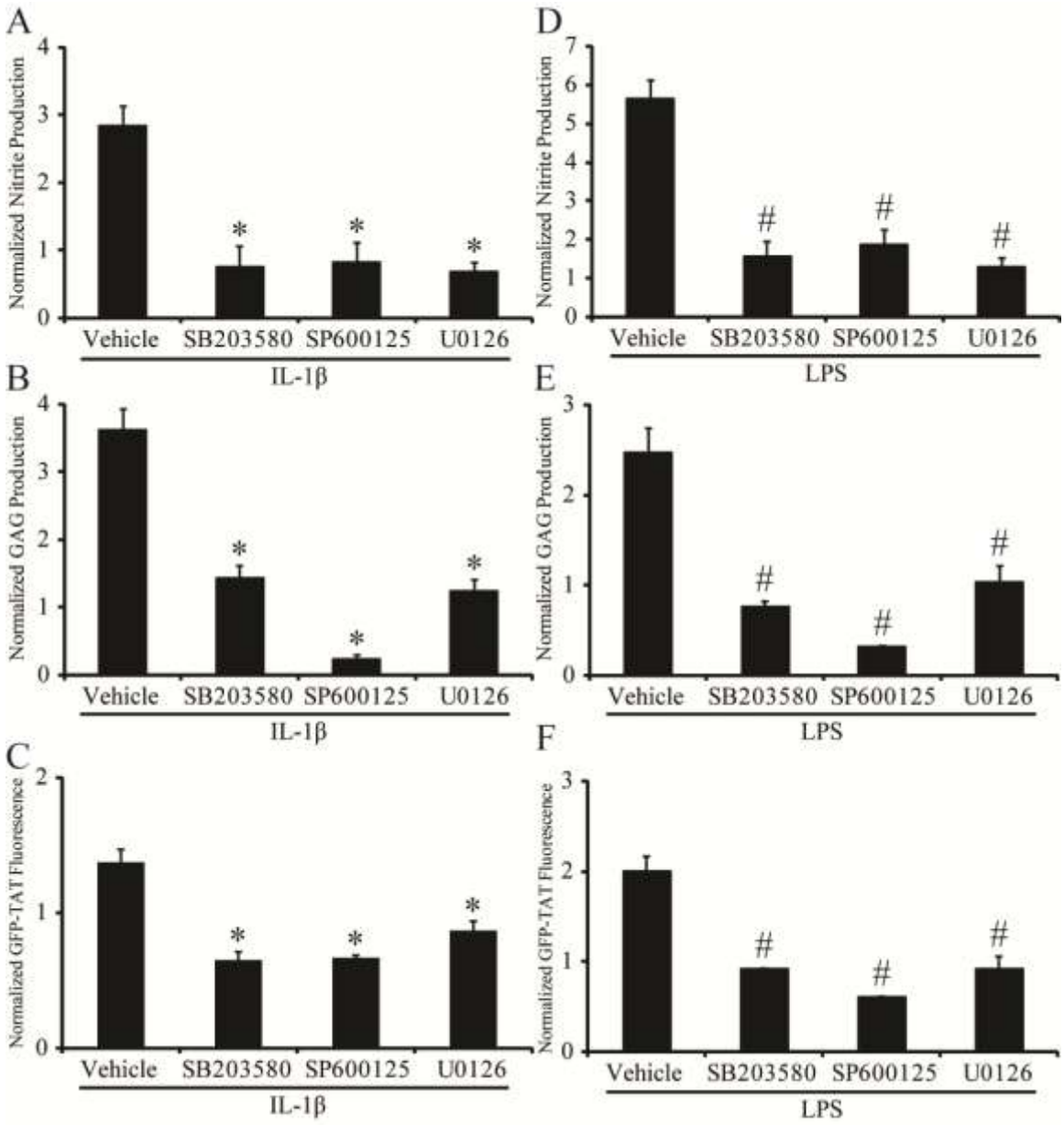

Figure 2.4 Effect of MAPK inhibition on IL-1β- and LPS-mediated activation. (**A**) The IL-1β-stimulated increase of nitrite content was significantly attenuated by MAPK inhibition ($n \geq 3$). (**B**) The IL-1β-stimulated increase of GAG content was significantly attenuated by MAPK inhibition ($n \geq 4$). (**C**) The IL-1β-stimulated increase in GFP-TAT transduction was significantly attenuated by MAPK inhibition ($n \geq 3$). (**D**) The LPS-stimulated increase of nitrite content was significantly attenuated by MAPK inhibition ($n \geq 3$). (**E**) The LPS-stimulated increase of GAG content was significantly attenuated by MAPK inhibition ($n \geq 3$). (**F**) The LPS-stimulated increase in GFP-TAT transduction was significantly

attenuated by MAPK inhibition ($n \geq 3$; *$p < 0.05$ compared to IL-1β + vehicle; #$p < 0.05$ compared to LPS + vehicle; mean ± standard error of the mean; MAPK, mitogen-activated protein kinase; IL-1β, interleukin IL-1β; LPS, lipopolysaccharide; GFP-TAT, green fluorescence protein-transactivator of transcription; GAG, glycosaminoglycans).

2.3.5 Inhibition of Activation via a TAT-JNK Peptide Inhibitor

Treating cultures with the TAT-JNK peptide inhibitor immediately after mechanical stretch injury significantly prevented the injury-induced increase of nitrite (Figure 2.5A) and GAG (Figure 2.5B) content measured 48 h after injury. GFP-TAT, L-TAT control peptide, and mTAT had no effect on nitrite (Figure 2.5A) or GAG (Figure 2.5B) production after mechanical stretch injury. Treating cultures with the TAT-JNK inhibitor also prevented the IL-1β and LPS induced increase of nitrite (Figure 2.5C, E) and GAG (Figure 2.5D, F) content measured 48 h after stimulation. GFP-TAT, L-TAT control peptide, and mTAT did not significantly alter nitrite (Figure 2.5C, E) or GAG (Figure 2.5D, F) production after IL-1β or LPS stimulation.

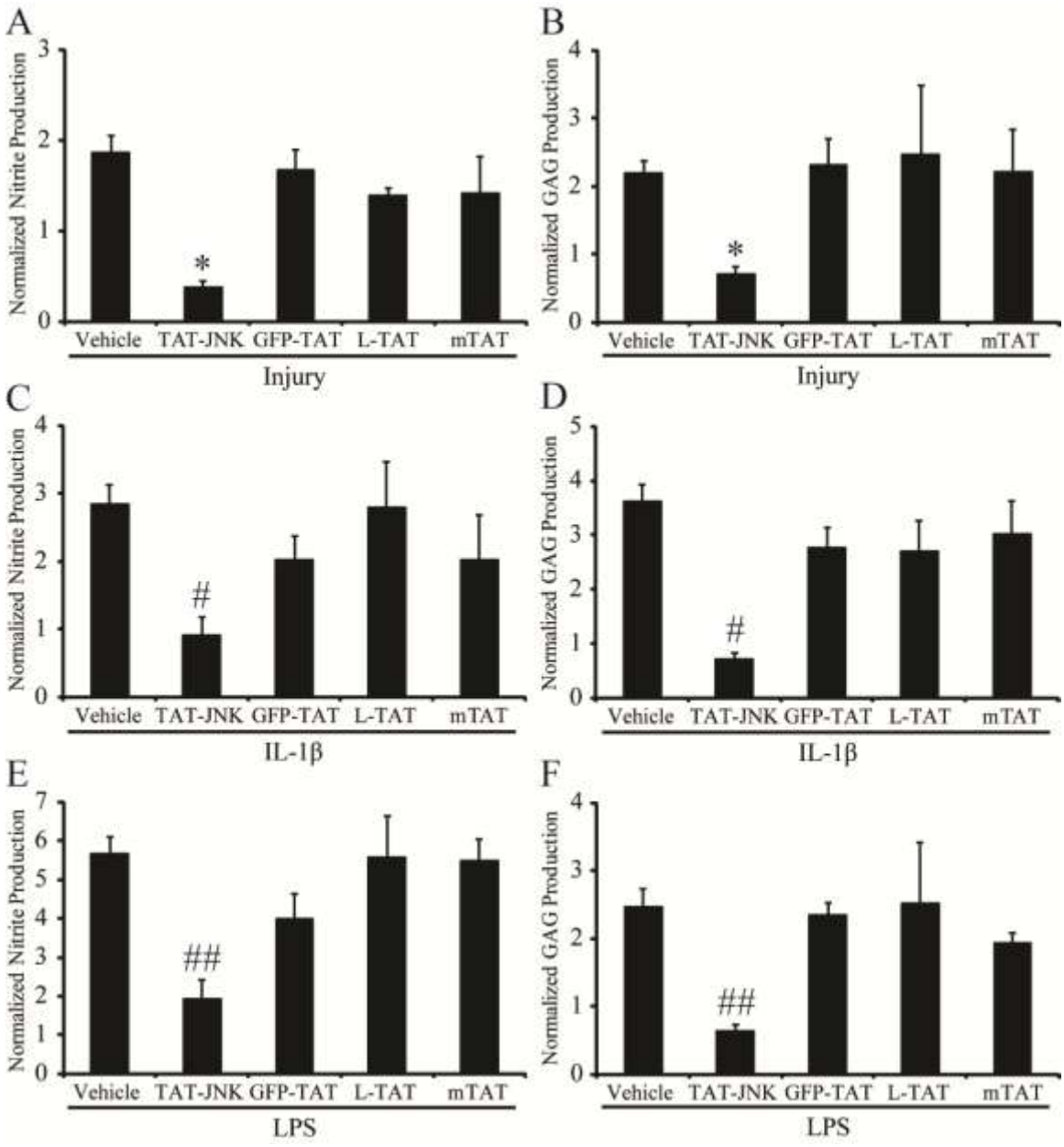

Figure 2.5 Effect of TAT-mediated delivery of a peptide JNK inhibitor on activation (**A**) The injury-induced increase of nitrite content was significantly attenuated by the TAT-JNK inhibitor ($n \geq 3$). (**B**) The injury-induced increase of GAG content was significantly attenuated by the TAT-JNK inhibitor ($n \geq 3$). (**C**) The increase of nitrite content after IL-1β stimulation was significantly attenuated by the TAT-JNK inhibitor ($n \geq 9$). (**D**) The increase of GAG content after IL-1β stimulation was significantly attenuated by the TAT-JNK inhibitor ($n \geq 5$). (**E**) Increases in nitrite production after LPS stimulation

were attenuated by the TAT-JNK inhibitor ($n \geq 6$). (**F**) Increases in GAG production after LPS stimulation were attenuated by the TAT-JNK inhibitor ($n \geq 5$). GFP-TAT, L-TAT control peptide, and mTAT did not significantly affect nitrite or GAG production after mechanical stretch injury, IL-1β, or LPS stimulation (*$p < 0.05$ compared to injured, vehicle-treated cultures; #$p < 0.05$ compared to IL-1β + vehicle; ##$p < 0.05$ compared to LPS + vehicle; mean ± standard error of the mean; IL-1β, interleukin IL-1β; LPS, lipopolysaccharide; GAG, glycosaminoglycans; TAT-JNK, transactivator of transcription-c-Jun N-terminal kinase; GFP-TAT, green fluorescence protein-transactivator of transcription).

2.4 Discussion

Astrocytes have been implicated to have both beneficial and harmful effects in the developing pathobiology after CNS insults (Morganti-Kossmann *et al.*, 2002, Sofroniew, 2005). Much of their negative effects are associated with the process of reactive gliosis or astrocyte activation in which astrocytes increase production of GAG and NO, among other changes in their physiology. In our study, NO and GAG production were chosen as functional measures of astrocyte activation because of their potential to detrimentally affect surrounding cells (Wada *et al.*, 1998b, Silver and Miller, 2004). Although GFAP is often used as a histological marker of activation (Pekny and Nilsson, 2005), whether it plays a functional role in the injury cascade is unclear. However, it is well established that increased expression of iNOS (Lee *et al.*, 1995) and the subsequent over production of NO (Wada *et al.*, 1998a, Wada *et al.*, 1998b) can cause cell death due to subsequent nitrosylation of proteins (Wada *et al.*, 1998b). Furthermore, increased production of extracellular GAG is known to be inhibitory to neurite outgrowth (Smith-Thomas *et al.*, 1994). GAGs form a significant component of the glial scar and cause growth cone collapse, preventing regeneration. Therefore, we chose to focus on these more relevant,

functional measures of activation. In the present study, astrocytes were activated by very different factors including mechanical stimulation with a well-characterized stretch injury model developed previously in our laboratory (Morrison *et al.*, 2003), cytokine treatment (Kim *et al.*, 2006) or LPS (Bhat *et al.*, 1998) to determine if the activation process could be controlled by the intracellular delivery of a peptide TAT-JNK inhibitor.

Utilization of TAT to target activated astrocytes via their increased GAG content could be of significant therapeutic value. Whereas the 86 amino acid, full length HIV-1 TAT has been implicated in neurodegeneration and neuroinflammation (Williams *et al.*, 2009), the CPP TAT is an 11 amino acid peptide which is non-toxic, non-inflammatory, and capable of cellular transduction (Vives *et al.*, 1997). Through TAT-mediated delivery of an appropriate therapeutic cargo, it may be possible to limit GAG production and iNOS activity in activated astrocytes, thereby limiting detrimental effects.

Regulation of the MAPKs p38, ERK and JNK may play a central role in astrocyte activation (Otani *et al.*, 2002, Guan *et al.*, 2006b, Hsiao *et al.*, 2007). These MAPKs are activated by a variety of stimuli, such as mechanical trauma (Mandell *et al.*, 2001), spinal cord injury (Stirling *et al.*, 2008), ischemia and reperfusion (Namura *et al.*, 2001, Guan *et al.*, 2006a) and cytokine (Waetzig *et al.*, 2005, Hsiao *et al.*, 2007) and LPS stimulation (Bhat *et al.*, 1998, Nakajima *et al.*, 2004). Inhibition of MAPK cascades by the small molecule inhibitors of p38 (Piao *et al.*, 2003, Yoo *et al.*, 2008), JNK (Hua *et al.*, 2002, Guan *et al.*, 2006a) and ERK (Mandell *et al.*, 2001) decreased the stimulated upregulation of iNOS *in vitro*. In the present study, small molecule inhibitors of p38 MAPK (SB203580), JNK (SP600125) and ERK (U0126) verified the essential role of the MAPK cascade in each of the different activation paradigms

employed. Taken together, these results suggest that therapeutic modulation of astrocyte activation may be possible via the MAPK pathways.

However, a significant limitation of existing small molecule inhibitors is that they cannot be targeted to a specific cell population, in this case activated astrocytes. In our study we chose to focus on JNK as a possible therapeutic target because, while the roles of p38 and ERK in astrogliosis are still controversial (Cole-Edwards *et al.*, 2006), the role of JNK in neurodegeneration after CNS insults has been well-established (Cole-Edwards *et al.*, 2006, Guan *et al.*, 2006a). Peptide inhibitors for JNK are commercially available (Axxora) and the TAT-JNK inhibitor has been well-characterized (Bonny *et al.*, 2001, Borsello *et al.*, 2003). In contrast, the peptide inhibitor of p38 has only recently been reported in literature (Fu *et al.*, 2008).

An alternative strategy to enhance repair is to target the glial scar directly. Degradation of the glial scar with chondroitinase ABC or attenuating its formation through the use of a GAG synthesis inhibitor have been shown to promote axonal regrowth (Moon *et al.*, 2001, Bradbury *et al.*, 2002, Silver and Miller, 2004). Unfortunately, the use of chondroitinase ABC as a therapeutic is not ideal as cleaving the GAG side chains leaves behind debris that remains inhibitory to neurite outgrowth (Ughrin *et al.*, 2003, Silver and Miller, 2004). Similarly, general inhibition of GAG production may have unwanted side effects as certain GAGs, such as heparan sulphate GAGs, are important in guiding axonal growth, promoting neurite outgrowth and facilitating synapse formation (Properzi *et al.*, 2008).

Successful glial-specific therapies will likely need to strike a fine balance between inhibiting negative consequences of astrocyte activation while maintaining their homeostatic

functions. Inhibiting their supporting function could exacerbate the pathology given their roles in the normal function of the brain. For example, reactive astrocytes were selectively ablated after spinal cord injury in mice expressing a GFAP-herpes simplex virus-thymidine kinase transgene with ganciclovir (Faulkner *et al.*, 2004). In that study, the ablation of all reactive astrocytes after injury resulted in the failure of blood-brain barrier repair, leukocyte infiltration, local tissue disruption, severe demyelination, neuronal and oligodendrocyte death, and pronounced motor deficits. Therefore a more subtle modulation of activation may be required for improved outcome. In our study, we aimed to preserve homeostatic astrocytic processes by down-regulating activated astrocytes rather than eliminating them altogether. This strategy may prove more beneficial for ameliorating the detrimental effects of activated astrocytes by maintaining their presence in the injury site. However further *in vivo* studies are necessary to clarify the relationship between modification of astrocyte activation and wound healing. Astrocytes grown in serum-containing medium have been used as models of reactive gliosis due to their proliferative nature (Audouy *et al.*, 1999). However, *in vitro* studies involving astrocyte cultures lack critical input regarding systemic effects and environmental cues which could potentially impact the results reported here, highlighting the need for additional *in vivo* work.

Reactive astrocytes play a key role in the formation of the glial scar that is inhibitory to axon growth (Wanner *et al.*, 2008) due to injury-induced up-regulation of GAG production (McKeon *et al.*, 1995). We hypothesized that the increase in GAG content of activated astrocytes could be exploited to deliver a therapeutic molecule since intracellular delivery of GFP by TAT was increased after activation induced by different stimulation paradigms (Figure 2.1C, Figure 2.2C). In confirmation of our hypothesis, a TAT-JNK peptide inhibitor significantly prevented the functional consequences of astrocyte activation after stretch-induced

injury, cytokine, or LPS stimulation, as measured by reduced nitrite and GAG production (Figure 2.5). Our study is the first to report direct modulation of astrocyte activation with a peptide JNK inhibitor. By exploiting this characteristic of activated astrocytes, our delivery strategy may be highly specific for activated astrocytes.

Previous studies have attempted to reduce astrogliosis after injury (Yu *et al.*, 1991, 1993, Ghirnikar *et al.*, 1994, Zhu *et al.*, 2007, Spigolon *et al.*, 2010). GFAP synthesis was inhibited in primary astrocytes after scratch injury by antisense RNA (Yu *et al.*, 1991). However, the inhibitory effect lasted only 3-5 days after injury due to the limited stability of the antisense RNA, resulting in only a delay in reactive astrogliosis. Utilization of the CDK inhibitor olomoucine arrested the developmental astrocytic cell cycle and reduced astrocyte activation after hypoxia, scratch-wound, and ischemia (Zhu *et al.*, 2007). Newly proliferating astrocytes have been implicated in the astrogliotic scar (Kernie *et al.*, 2001), however previously existing astrocytes may contribute significantly to the inhibitory effects of the glial scar as well. Systemic injections of kainic acid into the adult rat hippocampus induced marked increases of GFAP (Spigolon *et al.*, 2010). Administration of D-JNKI-1, the protease-resistant all-D-retroinverso form of the peptide inhibitor used in our study, significantly attenuated neuronal cell death and partially prevented increased GFAP expression, although not significantly. Although suggestive, a direct effect of the peptide inhibitor on astrocytes could not be distinguished from an indirect effect on astrocyte activation due to the significantly reduced neuronal death. The results of our study demonstrate that the TAT-JNK peptide inhibitor exerts a direct effect on astrocyte activation in response to multiple stimuli.

IL-1β- and LPS-mediated inflammation and neurotoxicity have been used to model a broad array of neurodegenerative diseases such as bacterial meningitis (Quagliarello *et al.*,

1991), Alzheimer's disease (Lee *et al.*, 2008) and Parkinson's disease (Yang *et al.*, 2008). Utilizing a peptide construct to deliver a JNK inhibitor to a specific population of cells to reduce the effects of IL-1β- and LPS-mediated activation and subsequent neurotoxicity could potentially be a targeted therapeutic for these and other neurodegenerative disorders. The ability to deliver a therapeutic cargo via TAT transduction to a specific cell population could be of practical use considering the wide range of cell types involved in these complex neuropathologies.

3 Functional Tolerance to Mechanical Deformation Developed from Organotypic Hippocampal Slice Cultures[2]

3.1 Introduction

Despite the rising incidence and societal cost of TBI (Finkelstein *et al.*, 2006, Langlois *et al.*, 2006, Faul *et al.*, 2010), treatment options remain limited or ineffective (Exo *et al.*, 2009, Kolias *et al.*, 2013), with drug candidates failing in clinical trials (Narayan *et al.*, 2002, Maas *et al.*, 2008). In light of the struggles to develop effective drug therapeutics for TBI, efforts to prevent TBI remain central to reducing its societal costs. However, developing more effective safety systems requires a fundamental understanding of injury mechanisms to translate the effects of mechanical stimuli to biologically relevant responses.

TBI is the result of brain tissue deformation, with tissue strain and strain rate identified as significant predictors of injury in the brain after TBI (Margulies and Thibault, 1992, Bain and Meaney, 2000, Cater *et al.*, 2006, Kleiven, 2006, Elkin and Morrison, 2007). TBI can alter intracellular signaling cascades (Atkins *et al.*, 2007b, Dash *et al.*, 2011), neurotransmitter receptor subunit expression (Giza *et al.*, 2006, Gibson *et al.*, 2010, Kharlamov *et al.*, 2011), neurotransmitter receptor function (Lea *et al.*, 2002), and neuron morphology (Gao *et al.*, 2011). The cumulative effect of these numerous changes can ultimately affect the electrophysiological activity of neuronal networks within the brain. Electrophysiological activity has been quantified in response to deformation/strain in guinea pig optic nerve (Bain and Meaney, 2000), giant squid axon (Galbraith *et al.*, 1993), and in cultured cortical neurons (Zhang *et al.*, 1996, Goforth *et al.*,

[2] A modified version of this chapter previously appeared in print: Kang, W.H. and Morrison, B. (2014). Functional Tolerance to Mechanical Deformation Developed from Organotypic Hippocampal Slice Cultures. Biomech Model Mechanobiol. Reprinted with permission by Springer.

2004, Kao *et al.*, 2004). Bain and Meaney measured visual evoked potentials after stretching guinea pig optic nerve, but did not investigate the effect of strain rate on electrophysiological activity (Bain and Meaney, 2000). In contrast, Galbraith *et al*. measured electrical response to elongation of giant squid axon at varying strain rates, but only for a few minutes after injury (Galbraith *et al.*, 1993). AMPA, $GABA_A$, and NMDA currents were recorded after stretching cortical neurons on an elastic membrane, but the injury model prevented quantification of Lagrangian strain (Zhang *et al.*, 1996, Goforth *et al.*, 2004, Kao *et al.*, 2004).

In this study, organotypic hippocampal slice cultures were mechanically injured using our well-characterized, *in vitro* model of TBI (Morrison *et al.*, 2003, Cater *et al.*, 2006, Morrison *et al.*, 2006, Elkin and Morrison, 2007) to investigate alterations in electrophysiological function following mechanical injuries at varying tissue strains and strain rates relevant to TBI. Changes in electrophysiological function were correlated to mechanical injury parameters in the form of mathematical equations describing the region-specific changes in electrophysiological function of the hippocampus after precisely controlled mechanical stimuli.

One of the applications of these equations is for interpreting the mechanical outputs of finite element (FE) models of TBI. Currently, FE models are capable of describing the mechanical events that occur during a TBI for the human brain (Kleiven and Hardy, 2002, Takhounts *et al.*, 2003, El Sayed *et al.*, 2008), as well as pig (Coats *et al.*, 2012) and rat brain (Lamy *et al.*, 2013, Mao *et al.*, 2013). However, developing accurate FE models requires a fundamental understanding of biological injury mechanisms to translate the effects of mechanical stimuli to biologically relevant responses. Our functional data can be incorporated into FE models to enhance their biofidelity of accident and collision reconstructions.

Combined with FE simulations of automobiles or safety equipment, FE models of the brain have the potential to significantly reduce the cost of safety systems engineering by optimizing the performance of new designs before expensive prototypes need to be produced (Nirula *et al.*, 2004, Moss *et al.*, 2014).

3.2 Materials and Methods

3.2.1 Organotypic Slice Cultures of the Rat Hippocampus

All animal procedures were reviewed and approved by the Columbia University Institutional Animal Care and Use Committee (IACUC). The brains of post-natal day 8-11 rat pups were aseptically removed and the hippocampus cut into 400 μm thick slices using a McIlwain tissue chopper (Harvard Apparatus, Holliston, MA, USA) according to published methods (Morrison *et al.*, 2006). Hippocampal slices were then transferred onto polydimethylsiloxane (PDMS) membranes (Specialty Manufacturing Inc., Saginaw, MI, USA) pre-coated with 80 μg/mL laminin (Life Technologies, Carlsbad, CA, USA) and 320 μg/mL poly-L-lysine (Sigma-Aldrich, St. Louis, MO, USA) and incubated in a standard cell-culture incubator (37°C, 5% CO_2) with Neurobasal medium (Life Technologies; supplemented with 1 mM Glutamax, 50X B27, 4.5 mg/mL D-glucose, and 10 mM HEPES) for the first 2-3 days. Slice cultures were then fed every 2-3 days with conditioned full-serum medium (Sigma-Aldrich; 50% minimum essential media, 25% Hank's balanced salt solution, 25% heat inactivated horse serum, 1 mM Glutamax, 4.5 mg/mL D-glucose, and 10 mM HEPES) and maintained in a standard cell-culture incubator (37°C, 5% CO_2) for 14-20 days total, including post-injury incubation. The fluorescent dye propidium iodide (Life Technologies) was used prior to injury

to stain for dead or injured cells to verify slice culture health. Unhealthy slice cultures were not included in the study (Effgen *et al.*, 2012).

3.2.2 Controlled Mechanical Deformation of Hippocampal Slice Cultures

The *in vitro* mechanical stretch injury device has been characterized previously in detail (Morrison *et al.*, 2003, Cater *et al.*, 2006, Morrison *et al.*, 2006). Briefly, after 10-14 days *in vitro*, media was removed from the culture well, and the hippocampal slice cultures were mechanically stretched by pulling the PDMS culture substrate over a rigid, tubular indenter under feedback control to precisely control the applied mechanical stimulus. Slice cultures were then returned to the incubator until electrophysiological function was assessed 4-6 days post-injury. The time after injury was selected based on previous studies that demonstrated maximum cell death by 4 days post-injury (Cater *et al.*, 2006, Yu and Morrison, 2010). The purpose of assessing electrophysiological function 4-6 days post-injury was to quantify altered function before neuronal repair and regeneration processes had begun. The induced tissue strain and strain rate were verified with high-speed video analysis of the dynamic stretch event. Lagrangian strain was determined by calculating the deformation gradient tensor by locating fiducial markers on the tissue slice before and at maximal stretch (Morrison *et al.*, 2003).

In total, 135 hippocampal slice cultures from 45 rat pups across 15 different litters were injured at strains (up to 0.44) and strain rates (up to 30 s^{-1}) relevant to TBI, with 12 uninjured slice cultures generated continuously throughout the entire course of experiments as negative controls. Uninjured slice cultures were age-matched to injured slice cultures to account for developmental changes *in vitro*. Uninjured slice cultures underwent identical procedures as injured slice

cultures, including being placed on the mechanical stretch injury device, only without device firing.

3.2.3 Assessment of Electrophysiological Function

Prior to electrophysiological assessment, 60-electrode microelectrode arrays (MEA, Multichannel Systems, Reutlingen, Germany) were made hydrophilic with gas plasma treatment and coated with nitrocellulose (Thermo Fisher Scientific, Waltham, MA, USA) for slice culture adhesion (Egert and Meyer, 2005). At the desired time point after injury, slice cultures were transferred to Biopore CM membranes (BGCM00010, EMD Millipore, Billerica, MA, USA), inverted onto pre-coated MEAs, and perfused with artificial cerebrospinal fluid (Sigma-Aldrich; 125 mM NaCl, 3.5 mM KCl, 26 mM $NaHCO_3$, 1.2 mM KH_2PO_4, 1.3 mM $MgCl_2$, 2.4 mM $CaCl_2$, 10 mM D-glucose, pH = 7.4) at 37°C, and aerated with 95% O_2/5% CO_2, as previously described (Yu and Morrison, 2010).

Spontaneous neural activity was measured by recording unstimulated neural signals continuously for 3 minutes at a sampling rate of 20 kHz. Raw data was low pass filtered with a 6 kHz analog, anti-aliasing filter and then passed through a 60 Hz comb filter using custom MATLAB scripts (version R2012a, MathWorks, Natick, MA, USA). Neural event activity was detected based on the Teager energy operator (Choi *et al.*, 2006). Spontaneous neural event firing rate, neural event duration, and neural event magnitude were calculated for all electrodes for each slice culture.

To evoke neuronal responses, a programmable stimulator (STG2004, Multichannel Systems) generated constant current, biphasic stimuli (a positive phase for 100 μs followed by a

negative phase for 100 μs) at the indicated currents. Neural signals were recorded at a sampling rate of 20 kHz and low pass filtered with a 6 kHz analog, anti-aliasing filter. Before analysis and fitting, raw recording data was filtered through a digital, 8th order Butterworth filter with a low pass frequency of 1000 Hz and a digital, 4th order Butterworth filter with a high pass frequency of 0.2 Hz in MATLAB (MathWorks).

Stimulus-response (S/R) curves were generated for each culture as previously described (Yu and Morrison, 2010). Bipolar, biphasic stimuli of varying magnitudes (0 μA – 200 μA in 10 μA steps) were applied to each slice culture through electrodes in the mossy fiber (MF) or Schaffer collateral (SC) regions of the hippocampal slice. Tissue response was recorded from all other channels simultaneously, and the amplitude of the field potential response was quantified as the peak to peak response. The response at each electrode was plotted versus stimulus current and then fit to a sigmoid function:

$$R(S) = \frac{R_{max}}{1 + e^{m(I_{50} - S)}}$$

Equation 3.1 Stimulus-response (S/R) equation for evoked response electrophysiology.

where R_{max} was the maximum peak to peak response, I_{50} was the current which produced a half-maximal peak to peak response, S was the current of the applied stimulus, and m was proportional to the slope of the linear region of the sigmoid curve. A representative S/R curve is plotted in Figure 3.1, illustrating the S/R parameters.

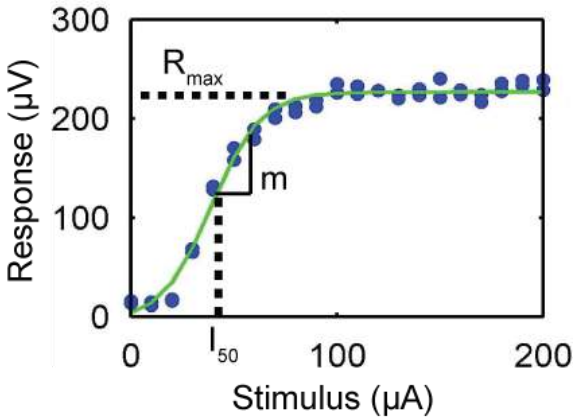

Figure 3.1 Representative stimulus-response (S/R) curve generated from fitting Equation 1 (green line) to raw electrophysiological data (blue). R_{max} was the maximum peak to peak response, I_{50} was the stimulus current which produced a half-maximal peak to peak response, and m was proportional to the slope of the linear portion of the sigmoid curve.

For paired-pulse recordings, paired-pulse responses were generated by delivering two successive stimuli of the same current (100 μA) at interstimulus intervals (ISI) of 40, 60, 80, 100, 140, 180, 220, 260, 300, 400, 500, 1000, 1500, and 2000 ms. The paired-pulse ratio (PPR) of peak to peak amplitudes was defined as the ratio of the amplitude of the second response to the amplitude of the first response. A PPR greater than 1 indicated paired-pulse facilitation, while a PPR less than 1 indicated paired-pulse depression (Fueta *et al.*, 1998). ISIs were assigned to four bins that are biologically relevant to short-term synaptic plasticity: Short Term ISIs (< 50 ms) elicit enhanced paired pulse depression mediated by the neurotransmitter γ-aminobutyric acid (GABA), specifically the $GABA_A$ class of GABA receptors (Stanford *et al.*, 1995, Margineanu and Wulfert, 2000); Early-Mid ISIs (50 – 100 ms) elicit a rebound in excitation thought to be caused by $GABA_A$ mediated disinhibition and activation of *N*-methyl-D-aspartate (NMDA)

receptors (Joy and Albertson, 1993, Stanford *et al.*, 1995); Late-Mid ISIs (140 – 500 ms) elicit late phase paired pulse depression mediated by $GABA_B$ receptors (DiScenna and Teyler, 1994, Stanford *et al.*, 1995); and Long Term ISIs (> 500 ms), where an effect of paired stimulation is not expected (Zucker, 1989, Commins *et al.*, 1998).

Spontaneous network synchronization was quantified for each spontaneous recording using previously published methods based on correlation matrix analysis and surrogate resampling for significance testing (Li *et al.*, 2007a, Li *et al.*, 2010b, Patel *et al.*, 2012). Correlation of neural events were computed to determine an event synchronization measure, called the synchronization index, for each electrode pair (Li *et al.*, 2007a). For two electrodes *x* and *y*, and neural event-timing t_i^x and t_j^y (i = 1, …, m_x; j = 1, …, m_y), the event correlation matrix was calculated by:

$$c^{\tau}(x|y) = \sum_{i=1}^{m_x}\sum_{j=1}^{m_y} J_{ij}^{\tau} \begin{cases} J_{ij}^{\tau} = 1 \; if \; 0 < t_i^x - t_j^y \leq \tau \\ J_{ij}^{\tau} = \frac{1}{2} \; if \; t_i^x = t_j^y \\ J_{ij}^{\tau} = 0 \; otherwise \end{cases}$$

Equation 3.2 Neural event correlation matrix equation for spontaneous electrophysiology.

where τ was the time interval in which two events were considered synchronous (1.5 ms), m_x and m_y were the total number of events to be compared, and J_{ij}^{τ} was a measure of correlation of two particular electrodes.

The event synchronization index for each electrode comparison, ranging in value from 0 (completely uncorrelated) to 1 (perfectly correlated), was calculated by:

$$Q_\tau = \frac{c^\tau(x|y) + c^\tau(y|x)}{\sqrt{m_x m_y}}$$

Equation 3.3 Neural event synchronization index equation for spontaneous electrophysiology.

To identify clusters of synchronized electrodes, first, the participation index (PI) was calculated for each electrode *a* that contributed to a cluster *b*:

$$PI_{ab} = \lambda_b v_{ab}^2$$

Equation 3.4 Participation index equation for spontaneous electrophysiology.

where v_{ab} was the a^{th} element of eigenvector v_b and λ_b was the corresponding eigenvalue. PI_{ab} indicated the contribution of electrode *a* to the synchronized cluster *b*, with v_{ab}^2defined as the weight with which electrode *a* contributed to cluster *b*.

Next, randomized surrogate time-series data without any correlated electrode pairs were generated with an event rate equal to the instantaneous event rate of the experimental recordings, and the eigenvalues of the surrogate correlation matrix were calculated (Li *et al.*, 2010b). The surrogate randomization was repeated 50 times and the mean ($\bar{\lambda}'_k$) and standard deviation (SD_k)

of surrogate eigenvalues were calculated (k = 1, …, M, where M was the number of electrodes). We identified the number of synchronized clusters that were significantly different from the randomized, asynchronous surrogates by:

$$Number\ of\ Clusters = \sum_{k} sgn\left[\lambda_k > \left(\bar{\lambda}'_k + K \times SD_k\right)\right]$$

Equation 3.5 Synchronized cluster equation.

where *sgn* was a sign function, λ_k was the eigenvalue of each electrode of the experimental data, and *K* was a constant (*K* = 3, for 99% confidence level, for a given number of electrodes).

Finally, a global synchronization index (GSI), ranging from 0 (completely random, uncorrelated activity) to 1 (perfectly synchronous, correlated activity), was calculated for the cluster with the highest degree of synchronization:

$$GSI = \begin{cases} \dfrac{\lambda_M - \bar{\lambda}'}{M - \bar{\lambda}'}\ if\ \lambda_M > \bar{\lambda}' \\ 0\ otherwise \end{cases}$$

Equation 3.6 Global synchronization index (GSI) equation.

where $\bar{\lambda}'$ was the mean of the highest eigenvalues calculated across all surrogates, λ_M was the maximal eigenvalue of the correlation matrix from the experimental data, and M was the number of electrodes.

To account for differences in the number of electrodes in each hippocampal region, the percentage of electrodes from each region in the cluster with the highest synchrony was calculated by dividing the number of electrodes in each region in the cluster with the highest synchrony by the total number of electrodes within a region in the entire hippocampal slice. The percentage of electrodes in each region in that cluster was multiplied by the GSI to obtain a normalized GSI for each region.

3.2.4 Statistical Analysis

To capture the dependence of changes in spontaneous (neural event firing rate, neural event duration, neural event magnitude), S/R (R_{max}, I_{50}, and m), and paired-pulse (PPR for Short Term ISIs, Early-Mid ISIs, Late-Mid ISIs, and Long Term ISIs) electrophysiological parameters to injury (strain and strain rate), nonlinear regression was performed and empirical functions were fit for the hippocampus using the MATLAB function *nlinfit.m*, and 95% confidence intervals were computed using the function *nlparci.m* (MathWorks). Data sets were also partitioned and fit separately for each hippocampal region (CA1, CA3, and DG). For S/R and paired-pulse data only, the data sets were further partitioned and fit separately for each stimulation site (MF and SC).

The functional forms of the fit equations were chosen based on the general shape of the data set, its gradients, and degree of non-linearity with respect to the independent variables. To

determine the best fit for each data partition, with an optimal number of terms to preserve parsimony, we performed *k*-fold cross validation, choosing to replicate 10-fold cross validation, 10 times. In *k*-fold cross validation, a data set consisting of *n* samples is randomly split into *k* subsets (or *k* folds), with each subset consisting of approximately *n*/*k* samples. Each of the *k* subsets is used as a test set, with the remaining $k - 1$ folds serving as training sets. The candidate equations are fit to the training set, then applied to the test set and the sum of squared errors (SSE) is calculated (Guo *et al.*, 2008). This procedure is repeated for *k* different test folds and the SSE is averaged over *k*. To account for random resampling variance, *k*-fold cross validation is generally iterated with different random permutations of training and test folds (Ounpraseuth *et al.*, 2012). A widely accepted choice of *k* is 10, and 10 to 30 iterations of 10-fold cross validation have been shown to minimize random resampling variance (Molinaro *et al.*, 2005). For *R* iterations of *k*-fold cross validation for a data set with *n* samples, the mean squared error (MSE) is calculated and the fit equation with the minimum value of MSE is chosen as the best fit equation for each data partition:

$$MSE = \frac{1}{R}\sum_{l=1}^{R}\frac{1}{k}\sum_{j=1}^{k}\sum_{i=1}^{n}\left(e_i - \hat{e}_{ijl}\right)^2$$

Equation 3.7 Equation for *k*-fold cross validation for electrophysiology best fit equations.

where e_i is the actual experimental value of the i^{th} sample and $\hat{e}_{ijl}$ is the predicted value of the i^{th} sample of the j^{th} data fold of the l^{th} iteration.

To test the significance of partitioning the data set according to hippocampal region and/or stimulation site, the F-test was applied, a method used to compare statistical models by testing whether the addition of terms significantly improves the goodness of fit (Allen, 1997, Finan *et al.*, 2012). The results of the F-test are summarized in Table 3.1 and Table 3.2. Finally, to test significance of cross-validated coefficients, a linear hypothesis test was performed for each coefficient in the best fit equations using the MATLAB function *coefTest.m* (MathWorks). Significance was set at $p < 0.05$.

Comparison	Hippocampus vs. Regions	
Parameter	F	*p*
Neural Event Firing Rate	0.020	1
Neural Event Duration	-2.112	1
Neural Event Magnitude	1.017	0.433

Table 3.1 Results from the F-test to compare model parsimony between data partitions for spontaneous electrophysiological parameters.

Comparison	MF+SC vs. MF and SC		MF+SC Hippocampus vs. Regions		MF Hippocampus vs. Regions		SC Hippocampus vs. Regions		MF+SC Hippocampus vs. MF and SC Regions		MF and SC Hippocampus vs. MF and SC Regions		MF+SC Regions vs. MF and SC Regions		MF+SC Regions vs. MF and SC Hippocampus	
Parameter	F	p	F	p	F	p	F	p	F	p	F	p	F	p	F	p
R_{max}	-0.429	1	6.073	*	-2.461	1	6.602	*	0.716	1	1.011	0.437	-1.040	1	-2.544	1
I_{50}	1.168	*	-3.182	1	-9.228	1	-3.000	1	-1.634	1	-1.884	1	-0.889	1	-4.624	1
m	7.726	*	-3.157	1	-1.991	1	-2.097	1	-0.018	1	-1.848	1	1.029	0.343	-44.972	1
Short Term PPR	1.497	*	-0.116	1	-0.561	1	0.282	1	0.082	1	-0.179	1	0.332	1	-0.748	1
Early-Mid PPR	1.143	*	-0.350	1	0.117	1	-0.067	1	0.080	1	0.018	1	0.292	1	-0.646	1
Late-Mid PPR	1.840	*	5.267	*	1.177	*	1.349	*	1.380	*	1.276	*	0.053	1	1.017	0.407
Long Term PPR	3.369	*	4.628	*	4.435	*	3.108	*	3.619	*	3.677	*	2.284	*	6.384	*

Table 3.2 Results from the F-test to compare model parsimony between data partitions for stimulus-response and paired-pulse electrophysiological parameters. *indicates $p < 0.05$; MF, mossy fiber stimulation; SC, Schaffer collateral stimulation.

Parameter	Data Partition	K	R	Constant	Strain	Strain^2	Strain^3	Rate (s)	Rate^2 (s^3)	Rate^3 (s^3)	Strain*Rate (s)	Strain^2*Rate (s)	Strain*Rate^2 (s^2)	Strain^2*Rate^2 (s^2)	Strain^3*Rate (s)	Strain*Rate^3 (s^3)
Neural Event Firing Rate	Hippocampus	3	0.18	0.08 (s^{-1}) ±0.01		0.41 ±0.24				-0.0000041 ±0.0000026						
Neural Event Duration	Hippocampus	5	0.29	5.18 (s) ±0.59				0.42 ±0.23	-0.019 ±0.017			-4.36 ±2.72	0.079 ±0.060			
Neural Event Magnitude	Hippocampus	4	0.27	27 (μV) ±1				-0.73 ±0.62	0.10 ±0.06	-0.0026 ±0.0015						
R_{max}	MF+SC CA1	3	0.17	508 (μV) ±48						-0.017 ±0.015					283 ±198	
	MF+SC CA3	4	0.25	774 (μV) ±88	-532 ±478				-0.64 ±0.34						468 ±225	
	MF+SC DG	5	0.23	601 (μV) ±64				-36 ±24			486 ±449	-2224 ±2110			3132 ±2888	
I_{50}	MF Hippocampus	3	0.30	26 (μA) ±3	74 ±25		-370 ±171									
	SC Hippocampus	5	0.32	29 (μA) ±2		252 ±190	-690 ±475				4.78 ±2.87		-0.17 ±0.11			
m	MF Hippocampus	6	0.33	0.16 (μV/μA) ±0.02	-0.26 ±0.11						-0.05 ±0.03	0.43 ±0.17		-0.027 ±0.009		0.00024 ±0.00008
	SC Hippocampus	4	0.26	0.14 (μV/μA) ±0.02	-0.07 ±0.06			-0.0057 ±0.0029	0.00030 ±0.00012							
Short Term PPR	MF Hippocampus	6	0.29	0.93 ±0.04		5.20 ±3.20	-11.46 ±8.84	0.012 ±0.005				-0.60 ±0.25			1.25 ±0.64	
	SC Hippocampus	6	0.31	0.89 ±0.03			2.54 ±1.91				0.30 ±0.12	-0.81 ±0.37	-0.012 ±0.005	0.031 ±0.015		
Early-Mid PPR	MF Hippocampus	6	0.26	0.95 ±0.03		3.41 ±2.42	-7.31 ±6.67	0.0084 ±0.0034				-0.39 ±0.19			0.81 ±0.48	
	SC Hippocampus	4	0.28	0.92 ±0.03		0.56 ±0.33		0.014 ±0.006	-0.00053 ±0.00025							
Late-Mid PPR	MF Hippocampus	1	0.13	0.95 ±0.01												
	SC Hippocampus	6	0.25	0.94 ±0.02		0.53 ±0.36		0.013 ±0.005		0.000026 ±0.000013	-0.081 ±0.037		0.0035 ±0.0016			
Long Term PPR	MF CA1	1	0.08	0.99 ±0.02												
	MF CA3	1	0.18	1.01 ±0.01												
	MF DG	1	0.10	1.01 ±0.01												
	SC CA1	5	0.28	0.98 ±0.02				0.006 ±0.004		-0.00001200 ±0.00001197	-0.040 ±0.029		0.0018 ±0.0015			
	SC CA3	6	0.35	1.01 ±0.02		0.76 ±0.51			0.0013 ±0.0007	-0.000059 ±0.000035	-0.095 ±0.051		0.0040 ±0.0023			
	SC DG	5	0.29	0.96 ±0.02				0.008 ±0.005		-0.000012 ±0.000011	-0.025 ±0.022			0.0030 ±0.0025		

Table 3.3 Fit equations for each electrophysiological parameter. Coefficient values are presented as ±95% confidence interval.

3.3 Results

For all electrophysiological parameters, at most, six parameters were necessary to optimally fit the raw data (Table 3.3). Changes in spontaneous activity after mechanical injury were best described by fit functions independent of hippocampal region (Figure 3.2). Neural event firing rate (Figure 3.2A) and duration (Figure 3.2B) were influenced by strain and strain rate in a complex fashion, while neural event magnitude (Figure 3.2C) was dependent on strain rate only. Neural event firing rate increased as strain increased and strain rate decreased (Figure 3.2A). Neural event duration peaked at moderate strain severity (approximately 0.2 strain) and high strain rate (30 s^{-1}) and generally increased with increasing strain rate (Figure 3.2B). Neural event magnitude exhibited a biphasic response to injury; magnitude generally increased as strain rate increased until peaking at approximately 20 s^{-1}, before decreasing back to uninjured levels between 20 and 30 s^{-1} (Figure 3.2C).

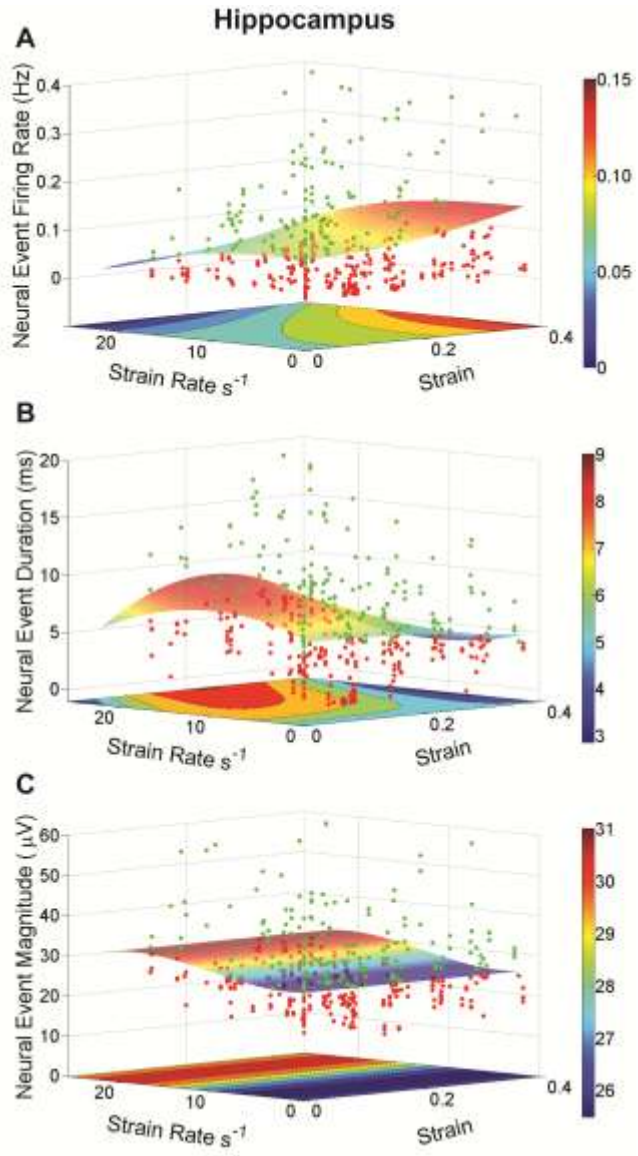

Figure 3.2 Alterations in spontaneous electrical activity of the hippocampus in response to mechanical injury parameters defined as tissue strain and strain rate. Raw data points are plotted above (green) and below (red) the surface representing the best fit equation. A 2D contour plot was included for visualization purposes. (A) Neural event firing rate was dependent on both strain and strain rate and increased as strain increased and strain rate decreased. (B) Neural event duration was dependent on both strain and strain in a complex fashion. Duration peaked at moderate strain severity (approximately 0.2 strain) and high strain rate (30 s^{-1}) and generally increased with increasing strain rate. (C) Neural event

magnitude was independent of strain and exhibited a biphasic response to injury; magnitude generally increased as strain rate increased until a peak value at approximately 20 s^{-1}.

Changes in R_{max} after mechanical injury were best described by separate fit functions for each hippocampal region, independent of stimulation site (Figure 3.3A, B, C). In contrast, changes in I_{50} (Figure 3.3D, E) and m (Figure 3.3F, G) were best described by separate fit functions for each stimulation site, but independent of hippocampal region. R_{max} in all regions peaked as strain rate increased at high strain (Figure 3.3A, B, C), although to varying magnitudes, with CA3 increasing the most in response to high strain and high strain rate injuries (Figure 3.3B). Changes in I_{50} in response to mossy fiber stimulation were independent of strain rate (Figure 3.3D), while I_{50} in response to Schaffer collateral stimulation exhibited minor dependence on strain rate (Figure 3.3E). I_{50} in response to mossy fiber and Schaffer collateral stimulation peaked at strains between 0.2 and 0.3, regardless of strain rate. Changes in m in response to mossy fiber stimulation were dependent on strain and strain rate in a complex fashion, with the greatest dependence on changes in strain and strain rate of any electrophysiological parameter (Figure 3.3F). Between 0.1 and 0.2 strain at high strain rates (>25 s^{-1}), a sharp increase in m was predicted by the fit equation, despite no raw data in that domain. In response to Schaffer collateral stimulation, m increased with increasing strain rate, with minimal effect of strain (Figure 3.3G).

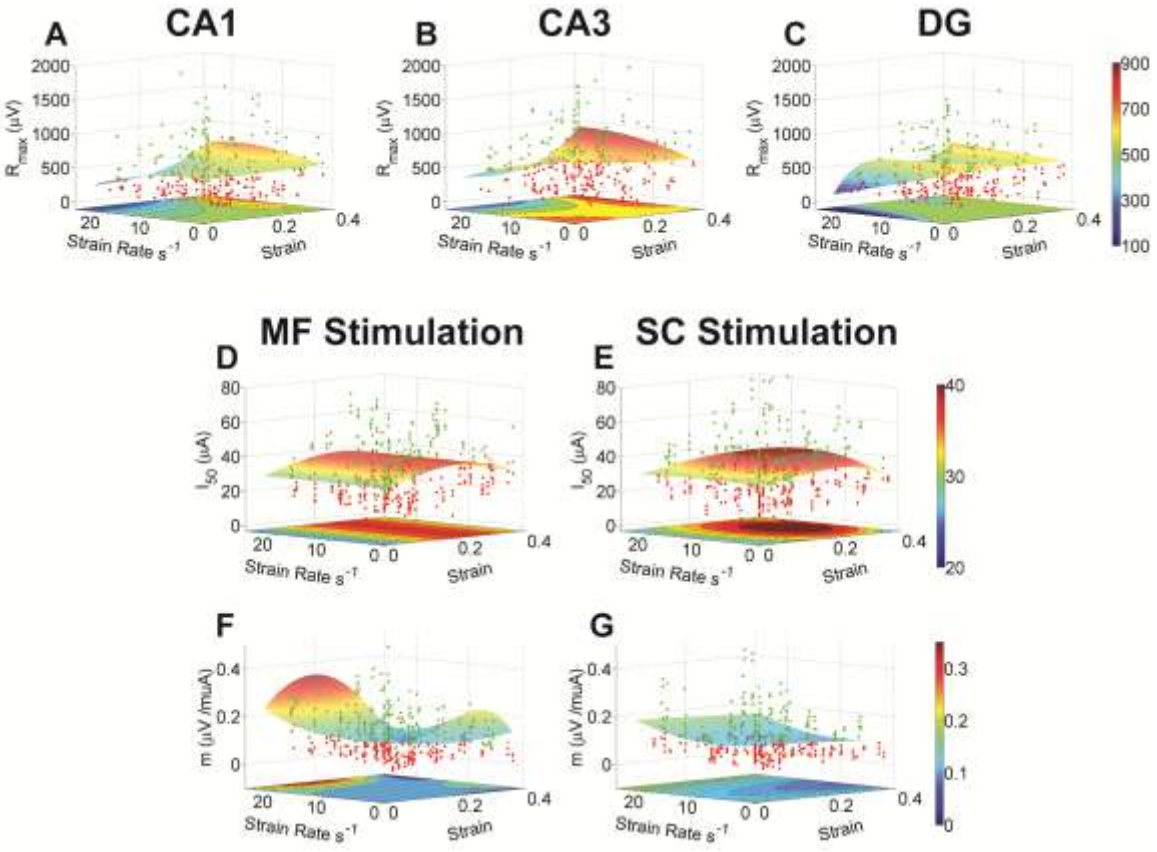

Figure 3.3 Alterations in S/R electrophysiology of the hippocampus in response to mechanical injury parameters defined as tissue strain and strain rate. Raw data points are plotted above (green) and below (red) the surface representing the best fit equation. A 2D contour plot was included for visualization purposes. R_{max} (A – C) was dependent on hippocampal region, but not stimulation site. I_{50} (D, E) and m (F, G) were both only dependent on stimulation site. R_{max} in CA1 (A), CA3 (B), and DG (C) peaked as strain rate increased at high strain, although to varying magnitudes. R_{max} decreased in all regions as strain rate increased at low strain. (D) I_{50} in response to mossy fiber stimulation was dependent only on strain and was independent of strain rate. (E) I_{50} in response to Schaffer collateral stimulation was dependent on strain and strain rate in a complex fashion. (F) m in response to mossy fiber stimulation was dependent on strain and strain rate in a complex fashion, peaking at high strain rate. (G) m in response to Schaffer collateral stimulation was dependent only on strain and was independent of strain rate. m generally increased with increasing strain rate.

Changes in PPR for Short Term ISIs (Figure 4a and 4b), Early-Mid ISIs (Figure 3.4C, D), and Late-Mid ISIs (Figure 3.4E, F) were best described by separate fit functions for each stimulation site, independent of hippocampal region. The only significant changes in PPR for Short Term ISIs and Early-Mid ISIs in response to mossy fiber stimulation occurred as strain rate increased at strains less than 0.1 (Figure 3.4A, C). PPR values approached 1.2, indicating paired-pulse facilitation at these injury values. In contrast, PPR for Short Term ISIs, Early-Mid ISIs, and Late-Mid ISIs in response to Schaffer collateral stimulation decreased as strain rate increased at strains less than 0.1 (Figure 3.4B, D, F), indicating paired-pulse depression. Upon closer inspection, all non-constant term coefficients of the fit functions for mossy fiber stimulation for Late-Mid ISIs did not significantly differ from zero, indicating that the best fit function was a horizontal plane at the value of the constant term coefficient, at approximately 1 (Figure 3.4E). Changes in PPR for Long Term ISIs were best described by separate fit functions for stimulation site and hippocampal region (data not shown). However, similar to mossy fiber stimulation for Late-Mid ISIs (Figure 3.4E), all non-constant term coefficients of the fit functions for mossy fiber stimulation for all hippocampal regions for Long Term ISIs did not significantly differ from zero, indicating that the best fit functions were horizontal planes at the values of the constant term coefficient, again at approximately 1 (data not shown). Best fit functions for changes in PPR for Long Term ISIs for Schaffer collateral stimulation were determined to be complex equations, but were essentially horizontal planes at the values of the constant term coefficient (data not shown).

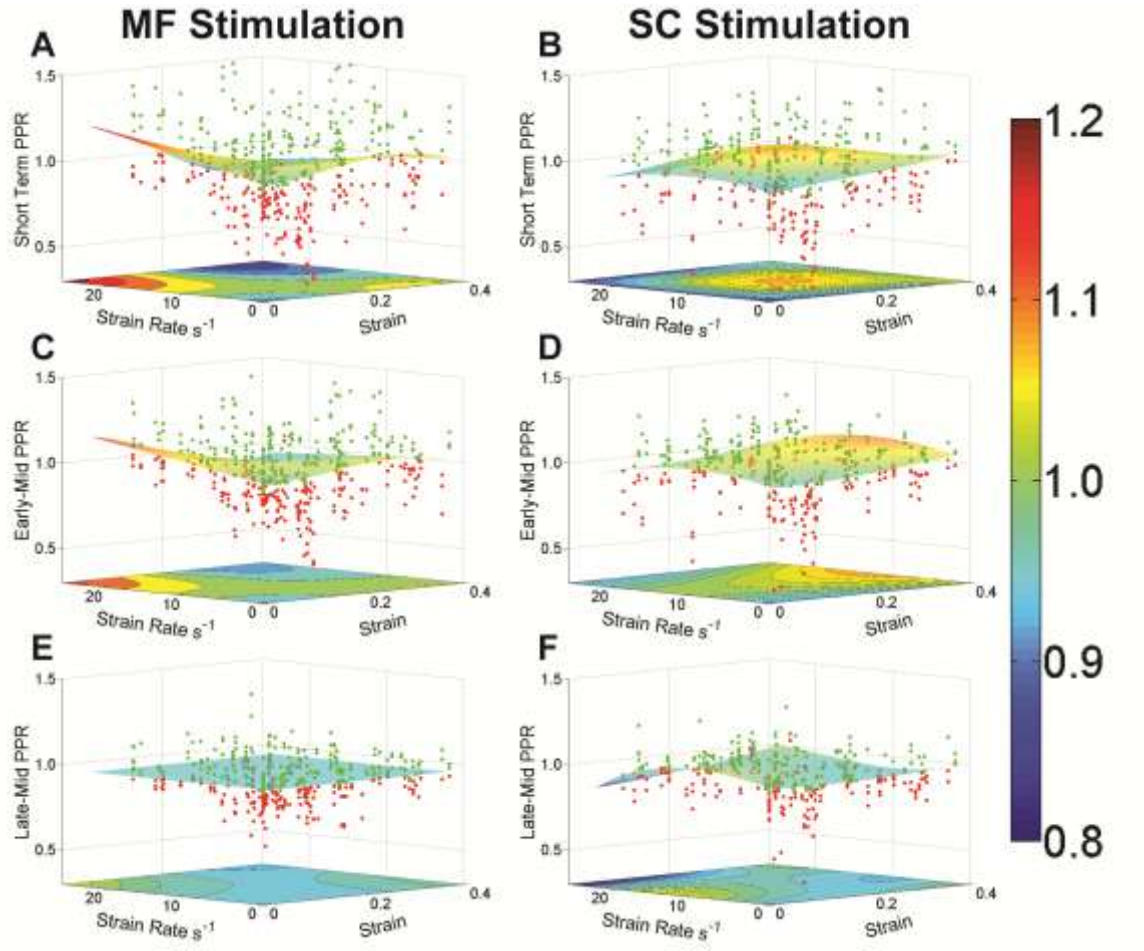

Figure 3.4 Alterations in PPR for the hippocampus in response to mechanical injury parameters defined as tissue strain and strain rate. Raw data points are plotted above (green) and below (red) the surface representing the best fit equation. A 2D contour plot was included for visualization purposes. PPR for Short Term ISIs (A, B), Early-Mid ISIs (C, D), and Late-Mid ISIs (E, F) were dependent on stimulation site, but independent of hippocampal region. PPR for all ISIs were dependent on both strain and strain rate. PPR for Short Term ISIs (A) and Early-Mid ISIs (C) in response to mossy fiber stimulation (left) increased with increasing strain rate at low strain values. In contrast, PPR for Short Term ISIs (B), Early-Mid ISIs (D), and Late-Mid ISIs (F) in response to Schaffer collateral stimulation (right) decreased with increasing strain rate at low strain values. PPR for Late-Mid ISIs (E) in response to mossy fiber stimulation were not significantly different from a horizontal plane at approximately PPR = 1.

In the hippocampus, only two parameters were necessary to optimally fit the raw data in all regions (Table 3.4). The normalized GSI was dependent only on strain rate in a monotonic manner (Figure 3.5). As strain rate increased, the normalized GSI increased. This is in contrast to previous studies of tolerance criteria based on cell death, which determined that cell death was dependent on tissue strain but not strain rate in the hippocampus (Cater *et al.*, 2006).

Region	K	Constant	Rate (s)	Rate^2 (s^2)	Rate^3 (s^3)
Hippocampus DG	2	0.044 ±0.017		0.00010 ±0.00007	
Hippocampus CA3	2	0.041 ±0.018	0.0019 ±0.0016		
Hippocampus CA1	2	0.046 ±0.016			0.0000035 ±0.0000031

Table 3.4 Fit equations for the normalized GSI. Values are prsented as ±95% confidence interval.

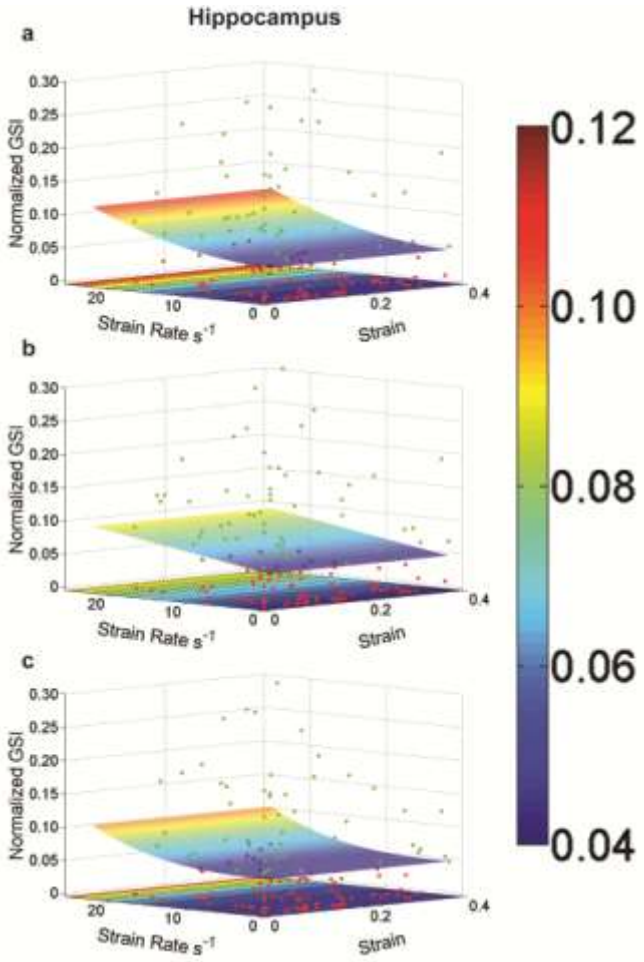

Figure 3.5 Alterations in network synchronization for the hippocampus in response to mechanical injury parameters defined as tissue strain and strain rate. Raw data points are plotted above (green) and below (red) the surface representing the best fit equation. A 2D contour plot was included for visualization purposes. In DG (A), CA3 (B), and CA1 (C), the normalized GSI was dependent only on strain rate and increased as strain rate increased.

Our functional results were compared to previous functional tolerance criteria determined by Bain and Meaney (Bain and Meaney, 2000). Using their best overall threshold for strain of 0.21 and an estimated value for strain rate of 30 s^{-1}, we compared the predicted changes in S/R

and paired-pulse electrophysiological function using the mathematical functions determined in this study (Figure 3.6).

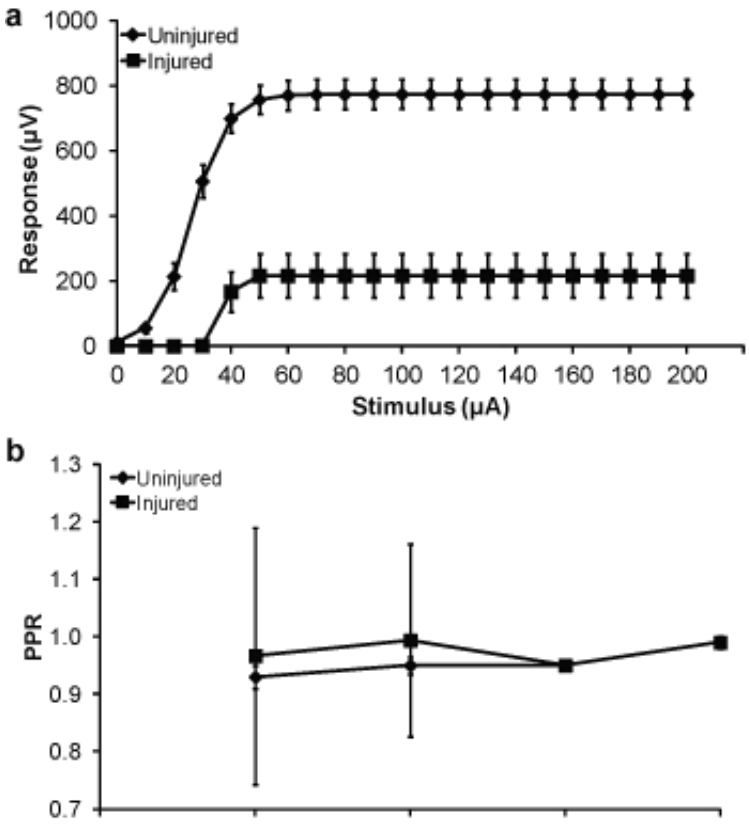

Figure 3.6 Changes in S/R and PPR generated from fit equations due to a particular combination of tissue strain and strain rate from Bain and Meaney. Tissue strain (0.21) and strain rate (30 s^{-1}) from uniaxial stretch of the optic nerve by Bain and Meaney were used as inputs to fit equations for R_{max}, I_{50}, and m to output S/R curves, and PPR for Short Term, Early-Mid, Late-Mid, and Long Term ISIs for paired-pulse data (mean ±SD).

To illustrate the utility of our data set for improving FE models of TBI, an example is given of how the data set can be applied. Data from physical injury reconstructions and FE modeling of a specific helmet-to-helmet collision of professional football players reported a strain of 0.15 and strain rate of 26 s^{-1} in the hippocampal and parahippocampal regions of the struck player (Viano *et al.*, 2005). We predicted the alterations in electrophysiological function of the hippocampus of the struck player by inputting the strain (0.15) and strain rate (26 s^{-1}) into the equations for R_{max}, I_{50}, m, and PPR for Short-Term, Early-Mid, Late-Mid, and Long-Term ISIs. The resulting values for these electrophysiological parameters were then compared with the expected electrophysiological function of the hippocampus of an uninjured player (Figure 3.7).

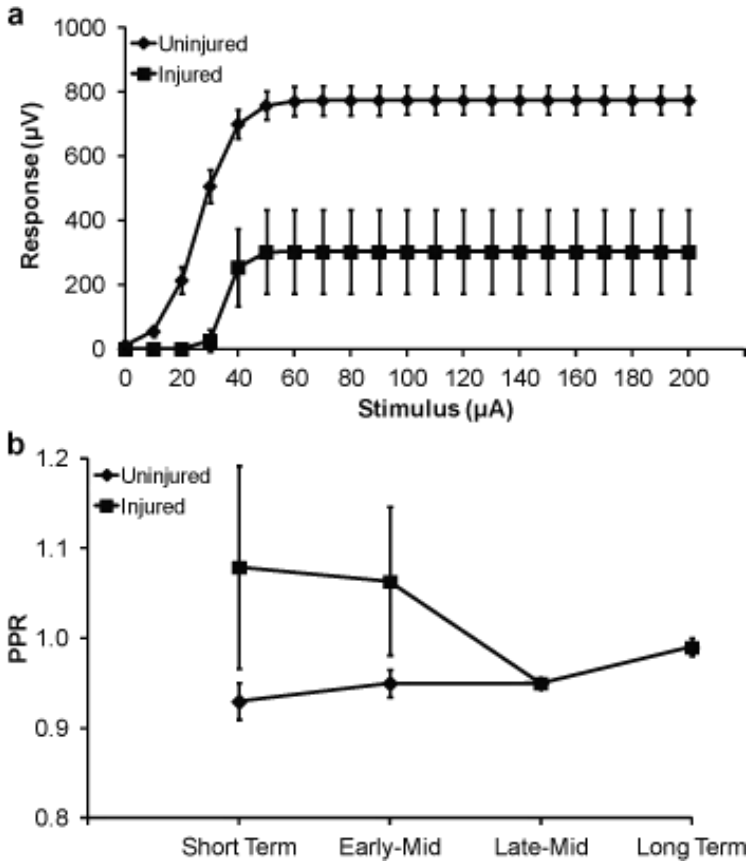

Figure 3.7 Changes in S/R and PPR generated from fit equations due to a particular combination of tissue strain and strain rate from Viano *et al*. Tissue strain (0.15) and strain rate (26 s^{-1}) from a helmet-to-helmet collision determined by Viano *et al*. were used as inputs to fit equations for R_{max}, I_{50}, and m to output S/R curves, and PPR for Short Term, Early-Mid, Late-Mid, and Long Term ISIs for paired-pulse data (mean ±SD).

3.4 Discussion

We have developed functional tolerance criteria for the hippocampus based on irreversible changes in electrophysiological function 4-6 days after precisely controlled mechanical deformation. By irreversible, we mean changes in the sub-acute period after injury before remodeling processes could repair the neuronal network. An optimal set of equations that parsimoniously describes the changes in electrophysiology after mechanical injury was determined by *k*-fold cross validation to account for the tradeoff between model complexity and goodness of fit, thus avoiding overfitting (Cawley and Talbot, 2010). We believe our model strikes a balance between model complexity and prediction accuracy, with all fit equations requiring no more than six terms without sacrificing significant prediction accuracy.

To determine the best fit for each data partition, with an optimal number of terms to preserve parsimony, two model selection methods were considered: penalized criteria, using Akaike's Information Criterion (AIC) (Burnham and Anderson, 2002) with a correction for small sample sizes (AIC_C) (Burnham and Anderson, 2004), and cross validation, using *k*-fold cross validation. The AIC_C provides a relative measure of information lost when a model is used to approximate the unknown, true model of a given data set, and can be used to determine the

tradeoff between the goodness of fit of a model and the model complexity (Akaike, 1973). The strengths of the AIC_C are its ease of calculation and simplicity of interpretation (Glatting *et al.*, 2007). Compared to cross validation methods, penalized criteria methods such as AIC_C can be more accurate for most data frameworks, with significantly less computational cost (Arlot and Celisse, 2010). However, because the value of the AIC_C itself for a given data set has no meaning on its own, only relative comparisons can be determined among candidate models (in this case, candidate fit equations for a given data partition but not for fits between different partitions of data). In addition, penalized criteria methods have been shown to overfit data sets that are not sufficiently homoscedastic (Arlot and Celisse, 2010). For these reasons we chose cross validation, specifically *k*-fold cross validation, to determine the best model among our sets of candidate models.

Previous studies have determined functional tolerances to mechanical injury by measuring changes in electrophysiological activity at specific strains and strain rates (Galbraith *et al.*, 1993, Bain and Meaney, 2000). It is difficult to directly compare our study to that of Galbraith *et al*. because they examined the response of the squid axon immediately after mechanical deformation, not in the subacute period days after injury. However, in general, they found that uniaxial stretch ratios in excess of 1.1 transiently depolarized neurons, which then recovered function within a few minutes and that the degree of depolarization was correlated with stretch magnitude. Bain and Meaney determined conservative, liberal, and best overall thresholds of strain for predicting morphological injury in guinea pig optic nerve. Using the strain (0.21) and strain rate ($30\ s^{-1}$) from Bain and Meaney, our functions predict impairment of neuronal network firing, as seen by the downward and rightward shift of the S/R curve and the increased PPR at Short Term and Early-Mid ISIs (Figure 3.6). Bain and Meaney predicted a

25% probability of morphological and functional injury at the specified strain and strain rate, whereas our functions predicted potentially larger changes in electrophysiological function. The differences in predicted electrophysiological function could be the result of using different species or testing different anatomical structures between the two studies. Bain and Meaney developed their functional tolerances for uniaxial extension of the optic nerve of guinea pigs, a model of pure axons compared to the heterogeneous population of neural cells present in organotypic slice cultures of the hippocampus that we biaxially deformed.

Although our study does not explicitly calculate one threshold in terms of strain and strain rate, we believe our approach to developing predictive equations for changes in electrophysiological function provides the end-user the ability to choose particular strain and strain rate inputs that produce a given change in electrophysiological parameters. In this way, the end-user can define a degree of dysfunction that is acceptable to their particular application. Rather than a single value for an injury tolerance, in this study we developed continuous mathematical functions relating input (strain and strain rate) and output (electrophysiological function). We believe this approach can potentially be more powerful than strict demarcations between safe and unsafe injuries, which may be too simplistic, particularly for complex biological responses such as electrophysiological function.

It is important to determine the functional response to mechanical injury in as many brain regions as possible due to the heterogeneity of TBI-induced functional damage in the brain, especially in the hippocampus (Witgen *et al.*, 2005, Bonislawski *et al.*, 2007). In our study, however, only changes in R_{max} were significantly dependent on hippocampal region, with all other electrophysiological parameters being insensitive to anatomical location. R_{max} is an approximation of the total number of functional synaptic contacts, *i.e.* the number of neurons that

fire in response to a given stimulus (Buchs *et al.*, 1993, Yu and Morrison, 2010). Because the density and distribution of synapses in the hippocampus vary from location to location, even within the same anatomic region, significant differences in the way R_{max} changes after injury between the hippocampal regions are not unexpected. Moderate TBI has been reported to decrease synaptic density in the DG (Gao *et al.*, 2011), consistent with the decrease in R_{max} predicted after moderate strain and strain rate using our predictive functions. The density and distribution of inhibitory and excitatory synapses has been quantified in CA1, with the majority of synaptic connections concentrated on excitatory pyramidal cells (Gao *et al.*, 2011). The higher ratio of excitatory to inhibitory neurons in the CA1 compared to DG could explain the differences in predicted changes in R_{max} between CA1 and DG.

A previous study reported that cell death in the hippocampus after mechanical injury was dependent on only tissue strain, monotonically increasing as strain increased (Cater *et al.*, 2006). In contrast, changes in electrophysiological function did not have a monotonic relationship with either strain or strain rate, changing in a complex manner dependent on both strain and strain rate. The complexity of our data is not surprising considering the nature of electrophysiological function in the hippocampus. For example, each region of the hippocampus consists of different types of neurons, including excitatory neurons, inhibitory interneurons, and even different cell types, such as astrocytes (Pascual *et al.*, 2012, Navarrete *et al.*, 2013) and microglia (Kettenmann *et al.*, 1993, Ji *et al.*, 2013), all of which contribute to the population-level electrophysiological activity of the hippocampus. The balance between excitatory and inhibitory neuronal activity as a result of different ratios of excitatory and inhibitory neurons in each hippocampal region also influences electrophysiological behavior (Gulyas *et al.*, 1999). Even within a specific class of neurons, such as interneurons, multiple cell subtypes exist, each with different firing

characteristics (Klausberger *et al.*, 2003, Hefft and Jonas, 2005). All of these cell types and subtypes may be susceptible to mechanical injury to different degrees, resulting in different network electrophysiological consequences depending on the magnitude of mechanical stimuli. Combined, the diversity of cells contributing to the population-level electrophysiological activity is expected to result in responses that are not monotonic with respect to strain.

To illustrate the utility of our data set in adding biological predictions to FE models of TBI, we compared data from a physical injury reconstruction and FE modeling of a specific helmet-to-helmet collision of professional football players with the expected electrophysiological function of the hippocampus of an uninjured player (Figure 3.7) (Viano *et al.*, 2005). The struck player was reported to have impaired cognition and short term memory, symptoms of disruption in the normal function of the medial temporal lobes, which include the hippocampus and parahippocampal regions (Viskontas *et al.*, 2006). The downward shift of the S/R curve after injury is caused by a decrease in R_{max} (Figure 3.7A). The drastic decrease in R_{max} can be interpreted as a decrease in the number of functional synaptic contacts, that could result in loss of neuronal network connectivity (Scheff and Price, 2006). Brain connectivity has been found to correlate with cognitive ability (Sze *et al.*, 1997). Thus, the decrease in R_{max} in the S/R curve of the injured player may help explain the cognitive impairments that resulted from the specific tissue deformations from the helmet-to-helmet collision.

The predicted changes in PPR following injury result in paired-pulse facilitation in the Short Term ISIs when paired-pulse depression is observed in uninjured hippocampus (Figure 3.7B). In healthy, uninjured hippocampus, paired-pulse depression at Short Term ISIs is mediated by the inhibitory neurotransmitter GABA, specifically through the $GABA_A$ class of receptors found in interneurons (Margineanu and Wulfert, 2000). The feedforward and feedback

regulation of excitability by inhibitory neurotransmission is an essential function of interneurons in the hippocampus (Sloviter, 1991). GABAergic dysfunction in the hippocampus has been implicated as a significant factor in cognitive and memory impairments (Savanthrapadian *et al.*, 2013). The switch from paired-pulse depression to paired-pulse facilitation in the Short Term ISIs could indicate dysfunction in GABAergic inhibition, which could further help explain the cognitive and short term memory impairments of the struck player.

Although correlating *in vitro* electrophysiological changes to behavior in humans remains speculative, changes in electrophysiology predicted by our fit equations could be a starting point in explaining the behavioral consequences of the simulated collision. In this way, our data set could be incorporated into FE models to add a functional component to the predictive capabilities of computational simulations of TBI.

Tissue strain and strain rate are significant predictors of injury in the brain after TBI (Margulies and Thibault, 1992, Bain and Meaney, 2000, Cater *et al.*, 2006, Kleiven, 2006, Elkin and Morrison, 2007). However, very few *in vivo* measurements of tissue strain and strain rate exist due to the difficulty of measuring tissue deformation within the brain during TBI (Bayly *et al.*, 2006, Hardy *et al.*, 2007). Studies involving *in vivo* measurements of tissue strain and strain rate have focused on axonal injury in primarily white matter brain tissue (Bain and Meaney, 2000, Singh *et al.*, 2006) or of non-injurious brain deformations in human volunteers (Sabet *et al.*, 2008, Feng *et al.*, 2010). Injury reconstructions using anthropomorphic test devices have been utilized in simulating the different injury variables in sports collisions (Pellman *et al.*, 2003, Zhang *et al.*, 2004) and traffic accidents (Kleiven, 2007, Post *et al.*, 2012). FE modeling continues to be an important technique for simulating TBI under a wide variety of impact and loading conditions (Takhounts *et al.*, 2008, Patton *et al.*, 2012, Rowson *et al.*, 2012).

Neuroimaging, such as diffusion tensor imaging (DTI) (Colgan *et al.*, 2010, Wright and Ramesh, 2012, Giordano *et al.*, 2014, Giordano and Kleiven, 2014) and magnetic resonance imaging (MRI) (McAllister *et al.*, 2012), can be used in conjunction with FE modeling and injury reconstructions to augment the biofidelity of numerical simulations by incorporation of directional white matter tracts. However, all of these methods suffer from the same limitations in that they must be validated against experimental data sets in animal models or in human cadaver studies, and each method is constructed on a set of underlying assumptions and simplifications to approximate the anatomical and physiological details of the head during TBI. Until it becomes possible to measure directly brain deformation *in vivo* during TBI, *in vitro* models of TBI will continue to be necessary to provide valuable inputs to FE models, accident reconstructions, and other numerical simulations of TBI. Our *in vitro* approach allows for an approximation of the hippocampal response to tissue strain and strain rate due to the biofidelity of the organotypic slice culture model (Noraberg *et al.*, 1999). However, a limitation of our study is whether these results can be applied to human FE models or are specific to the rat. While rat and human brains are very different at the macroscopic level, at the cellular and tissue level, evidence exists that they may be similar (Shreiber *et al.*, 1999). Mechanical properties of brain tissue may not be significantly different between species, particularly for strain-based tissue deformation (Ommaya *et al.*, 1967). Experiments with living cultures of human brain tissue would also directly address this limitation.

A further limitation of our study is that the data domain used to determine the fit equations was restricted to the maximum tissue strains and strain rates achievable using our *in vitro* stretch injury device. In our data sets, a maximum tissue strain of 0.44 and a maximum tissue strain rate of 30 s^{-1} were achieved. Data from physical injury reconstructions and FE

modeling of helmet-to-helmet collisions of professional football players found that a collision with a 50% probability of concussion featured a strain and strain rate of 0.26 and 48.5 s^{-1}, respectively, in gray matter (Kleiven, 2007), with other studies implicating even higher brain strains and strain rates in moderate to severe TBI (Kimpara and Iwamoto, 2012, Post *et al.*, 2012). The strain rate in the reconstructed collision from Kleiven 2007 would surpass the upper bound in our data set, requiring extrapolation outside the loading conditions used to construct our fit equations. Thus, caution should be exercised when attempting to interpret changes in electrophysiological parameters in response to TBI in excess of our maximal experimental values.

4 Predicting Changes in Cortical Electrophysiological Function after In Vitro Traumatic Brain Injury[3]

4.1 Introduction

Traumatic brain injury (TBI) remains a significant health concern in the United States, with annual incidence and estimated societal cost on the rise (Finkelstein *et al.*, 2006, Langlois *et al.*, 2006, Faul *et al.*, 2010). Efforts to prevent TBI by developing more effective safety systems remain central to reducing the societal impact of this growing epidemic (Nirula *et al.*, 2004, Moss *et al.*, 2014), particularly in light of the continuing struggle to develop effective drug therapeutics (Narayan *et al.*, 2002, Maas *et al.*, 2008). Finite element (FE) models of the brain are important tools in the development and testing of safety systems as they can predict the biomechanical outcomes of *in silico* simulations (Aare *et al.*, 2004). However, the predictive capability of FE models is dependent on tolerance criteria capable of describing the anatomical, region-specific response of the brain to quantitative, input injury parameters.

Current FE models have been developed to describe the mechanical events occurring within the brain during a TBI in humans (Kleiven and Hardy, 2002, El Sayed *et al.*, 2008, Takhounts *et al.*, 2008) and animals (Mao *et al.*, 2006, Lamy *et al.*, 2013, Mao *et al.*, 2013). However, a predictive model of the outcome of mechanical injury is incomplete without a fundamental understanding of how mechanical stimuli translate to biologically relevant responses. Electrophysiological activity has been quantified previously in response to deformation in giant squid axon (Galbraith *et al.*, 1993), guinea pig optic nerve (Bain and

[3] A modified version of this chapter has been submitted for publication: Kang, W.H. and Morrison B., 3rd (2014). Predicting Changes in Cortical Electrophysiological Function after In Vitro Traumatic Brain Injury. Biomech Model Mechan.

Meaney, 2000), and in cultured cortical neurons (Zhang *et al.*, 1996, Goforth *et al.*, 2004, Kao *et al.*, 2004). Galbraith *et al*. measured the electrical response to stretch of giant squid axon at various strain rates, but only for a few minutes post-injury (Galbraith *et al.*, 1993). Bain and Meaney measured visual evoked potentials (VEP) of stretched guinea pig optic nerve, but did not investigate the effect of varying strain rate on VEP (Bain and Meaney, 2000). AMPA, $GABA_A$, and NMDA currents were recorded after stretching cortical neurons cultured on an elastic membrane, but the injury model prevented quantification of Lagrangian strain (Zhang *et al.*, 1996, Goforth *et al.*, 2004, Kao *et al.*, 2004).

Anatomical, region-specific tolerance criteria relating mechanical parameters of tissue strain and strain rate to cell death have been developed previously for the hippocampus (Cater *et al.*, 2006) and cortex (Elkin and Morrison, 2007). However, neuronal and glial cell death do not adequately describe the dysfunctional behavior of the brain after TBI and do not always correlate with functional deficits (Lyeth *et al.*, 1990, Santhakumar *et al.*, 2000), necessitating a more complete description of the biological outcomes of the living brain in response to mechanical injury. Therefore, quantifying alterations in network electrophysiological function has the potential to provide unique functional information about the effects of TBI. It is possible that the death of individual brain cells might go unnoticed by the patient in the absence of a change in brain function, *i.e.* behavior, highlighting the importance of tolerance criteria based on changes in neuronal network function in addition to those based on cell death or structural damage.

Previously, we determined functional tolerance criteria relating tissue strain and strain rate to changes in electrophysiological function for the hippocampus (Kang and Morrison, 2014). In the present study, functional tolerance criteria for the cortex were determined. Organotypic cortical slice cultures were subjected to mechanical stretch injury using our well-characterized,

in vitro model of TBI (Morrison *et al.*, 2003, Cater *et al.*, 2006, Morrison *et al.*, 2006, Cater *et al.*, 2007), and changes in electrophysiological function to varying tissue strains and strain rates relevant to TBI were quantified. Electrophysiological parameters associated with unstimulated spontaneous network activity (neural event rate, duration, and magnitude), stimulated evoked responses (R_{max}, I_{50}, and m), and evoked paired-pulse ratios (PPR) at varying interstimulus intervals (ISI) were correlated to mechanical injury parameters by fitting mathematical functions to the raw data. The resulting fit functions could be incorporated into FE models of TBI to improve the predictive capabilities of the consequences of TBI from numerical simulations. The ability to engineer new protective safety systems *in silico* via FE models with accurate biomechanical and functional outputs could significantly reduce the cost of developing protective equipment against TBI.

4.2 Materials and Methods

4.2.1 Organotypic Slice Cultures of the Rat Cortex

Animal procedures were reviewed and approved by the Columbia University Institutional Animal Care and Use Committee (IACUC). The brains of post-natal day 8-11 Sprague-Dawley rat pups were aseptically removed and a strip of cerebral cortex directly above the hippocampus was excised from each cerebral hemisphere and cut into 375 μm thick slices using a McIlwain tissue chopper (Harvard Apparatus, Holliston, MA, USA), according to previously published methods (Elkin and Morrison, 2007). Cortical slices were then transferred to polydimethylsiloxane (PDMS) membranes (Specialty Manufacturing Inc., Saginaw, MI, USA) that were pre-coated with 80 μg/mL laminin (Life Technologies, Carlsbad, CA, USA) and 320

μg/mL poly-L-lysine (Sigma-Aldrich, St. Louis, MO, USA), and incubated at 37°C with Neurobasal medium (Life Technologies; supplemented with 1 mM Glutamax, 50X B27, 4.5 mg/mL D-glucose, and 10 mM HEPES) for the first 2-3 days. Cortical slice cultures were fed every 2-3 days with conditioned full-serum medium (Sigma-Aldrich; 50% minimum essential media, 25% Hank's balanced salt solution, 25% heat inactivated horse serum, 1 mM Glutamax, 4.5 mg/mL D-glucose, and 10 mM HEPES) and maintained in a standard cell-culture incubator (37°C, 5% CO_2) for 11-17 days total, including post-injury incubation.

4.2.2 Controlled Mechanical Deformation of Organotypic Cortical Slice Cultures

Immediately prior to mechanical stretch injury, the fluorescent dye propidium iodide (Life Technologies) was used to stain dead or injured cells. Unhealthy slice cultures were eliminated from the study, according to published methods (Effgen *et al.*, 2012). The *in vitro* mechanical stretch injury device has been previously characterized in detail (Morrison *et al.*, 2003, Cater *et al.*, 2006, Morrison *et al.*, 2006, Cater *et al.*, 2007). Briefly, after 7-12 days *in vitro*, media was removed from the culture well, and the cortical slice cultures were subjected to equibiaxial stretch by pulling the PDMS culture substrate over a rigid, tubular indenter under feedback control to precisely control the applied mechanical stimulus. Cortical slice cultures were then returned to the incubator until 4-6 days post-injury for assessment of electrophysiological function. The time after injury was determined based on previous studies that demonstrated maximum cell death by 4 days post-injury (Elkin and Morrison, 2007, Yu and Morrison, 2010). The purpose of assessing electrophysiological function 4-6 days post-injury was to quantify altered function before neuronal repair and regeneration processes could begin.

The induced tissue strain and strain rate were verified via high-speed video analysis of the dynamic stretch event. Lagrangian strain was determined by calculating the deformation gradient tensor using fiducial markers on the tissue slice image before and at maximal stretch (Morrison *et al.*, 2003).

In total, 119 cortical slice cultures from at least 40 rat pups across a minimum of 13 different litters were injured at strains (up to 0.59) and strain rates (up to 26 s^{-1}) relevant to TBI. Uninjured cortical slice cultures were age-matched to injured slice cultures to account for developmental changes *in vitro*. Uninjured slice cultures underwent identical procedures as injured slice cultures, including being placed on the stretch injury device without device firing.

4.2.3 Assessment of Electrophysiological Function

Immediately prior to electrophysiological measurements, 60-electrode microelectrode arrays (MEA) with electrode diameter of 30 μm and electrode spacing of 200 μm (60MEA200/30iR-Ti-gr, Multichannel Systems, Reutlingen, Germany) were made hydrophilic with gas plasma treatment and coated with nitrocellulose (Thermo Scientific, Waltham, MA, USA) for slice culture adhesion (Egert and Meyer, 2005). At 4-6 days post-injury, cortical slice cultures were transferred to Biopore CM membranes (MGCM00010, EMD Millipore, Billerica, MA, USA), inverted onto pre-coated MEAs, and perfused with artificial cerebrospinal fluid (Sigma-Aldrich; 125 mM NaCl, 3.5 mM KCl, 26 mM $NaHCO_3$, 1.2 mM KH_2PO_4, 1.3 mM $MgCl_2$, 2.4 mM $CaCl_2$, 10 mM D-glucose, pH = 7.4) at 37°C and aerated with 95% O_2/5% CO_2, as previously described (Yu and Morrison, 2010).

Spontaneous neural activity was measured by continuous recording of unstimulated neural signals for 3 minutes at a sampling rate of 20 kHz. Raw data was low pass filtered with a 6 kHz analog, anti-aliasing filter and passed through a 60 Hz comb filter using custom MATLAB scripts (version R2012a, MathWorks, Natick, MA, USA). Neural activity was detected using a custom MATLAB script with an action potential detector based on the Teager energy operator (Choi *et al.*, 2006). Unstimulated neural event rate, duration, and magnitude were calculated for all electrodes for each cortical slice culture.

To evoke responses, a programmable stimulator (STG2004, Multichannel Systems) generated constant current, biphasic stimuli (a positive phase for 100 μs followed by a negative phase for 100 μs) at the indicated current magnitudes. Evoked neural signals were recorded at a sampling rate of 20 kHz and low pass filtered with a 6 kHz analog, anti-aliasing filter. Prior to analysis and fitting, raw recording data was also filtered through a digital, 8^{th} order Butterworth filter with a low pass frequency of 1000 Hz and a digital, 4^{th} order Butterworth filter with a high pass frequency of 0.2 Hz in MATLAB (MathWorks).

Stimulus-response (S/R) curves were generated for each slice culture, as previously described (Yu and Morrison, 2010). Briefly, bipolar, biphasic stimuli of varying magnitudes (0 μA – 200 μA in 10 μA steps) were applied to the slice culture through electrodes in Layer IV of the cortical slice. Layer IV was chosen due to the abundance of granule cell bodies that send projections to supragranular Layers II – III and infragranular Layers V – VI (Alloway *et al.*, 1993). Previous studies have shown that thalamic stimulation induces a strong initial excitation in Layer IV granule cells which then leads to a series of excitations throughout the cortical layers, starting at the supragranular Layers II – III and followed by the infragranular Layers V – VI (Armstrong-James *et al.*, 1992, Staiger *et al.*, 2000). Stimulation in Layer IV resulted in the

most consistent evoked responses throughout the organotypic cortical slice cultures (data not shown). Stimulated responses were recorded from all channels simultaneously, and the amplitude of the evoked field potential response was quantified as the peak to peak response. The peak to peak response at each electrode was plotted versus stimulus current and then fit to a sigmoid function:

$$R(S) = \frac{R_{max}}{1 + e^{m(I_{50} - S)}}$$

Equation 4.1 Stimulus-response (S/R) equation for evoked response electrophysiology.

in which R_{max} was the maximum peak to peak response, I_{50} was the current that produced a half-maximal peak to peak response, S was the current of the applied stimulus, and m was proportional to the slope of the linear region of the sigmoid fit curve.

For paired-pulse recordings, paired-pulse responses were generated by delivering two successive stimuli at I_{50} with ISI of 20, 35, 40, 50, 60, 70, 80, 100, 140, 180, 220, 260, 300, 400, 500, 1000, 1500, and 2000 ms. The PPR was defined as the ratio of the peak to peak amplitude of the second response to the peak to peak amplitude of the first response. PPR greater than 1 indicated paired-pulse facilitation, whereas PPR less than 1 indicated paired-pulse depression (Fueta *et al.*, 1998). ISI were assigned to four bins with distinct biological relevance to short term synaptic plasticity: Short Term ISIs (< 50 ms) elicit paired-pulse depression mediated by the neurotransmitter γ-aminobutyric acid (GABA), specifically the $GABA_A$ class of GABA receptors (Stanford *et al.*, 1995, Margineanu and Wulfert, 2000); Early-Mid ISIs (50 – 100 ms)

elicit a rebound in excitation thought to be caused by $GABA_A$-mediated disinhibition and activation of *N*-methyl-D-aspartate (NMDA) receptors (Joy and Albertson, 1993, Stanford *et al.*, 1995); Late-Mid ISIs (140 – 500 ms) elicit late phase paired-pulse depression mediated by $GABA_B$ receptors (DiScenna and Teyler, 1994, Stanford *et al.*, 1995); and Long Term ISIs (> 500 ms) produce independent responses with a PPR close to 1 (Zucker, 1989, Commins *et al.*, 1998).

Spontaneous network synchronization was quantified for each spontaneous recording using previously published methods based on correlation matrix analysis and surrogate resampling for significance testing (Li *et al.*, 2007a, Li *et al.*, 2010b, Patel *et al.*, 2012). Correlation of neural events were computed to determine an event synchronization measure, called the synchronization index, for each electrode pair (Li *et al.*, 2007a). For two electrodes *x* and *y*, and neural event-timing t_i^x and t_j^y (i = 1, …, m_x; j = 1, …, m_y), the event correlation matrix was calculated by:

$$c^{\tau}(x|y) = \sum_{i=1}^{m_x}\sum_{j=1}^{m_y} J_{ij}^{\tau} \begin{cases} J_{ij}^{\tau} = 1 \; if \; 0 < t_i^x - t_j^y \leq \tau \\ J_{ij}^{\tau} = \frac{1}{2} \; if \; t_i^x = t_j^y \\ J_{ij}^{\tau} = 0 \; otherwise \end{cases}$$

Equation 4.2 Neural event correlation matrix equation for spontaneous electrophysiology.

where τ was the time interval in which two events were considered synchronous (1.5 ms), m_x and m_y were the total number of events to be compared, and J_{ij}^{τ} was a measure of correlation of two particular electrodes.

The event synchronization index for each electrode comparison, ranging in value from 0 (completely uncorrelated) to 1 (perfectly correlated), was calculated by:

$$Q_\tau = \frac{c^\tau(x|y) + c^\tau(y|x)}{\sqrt{m_x m_y}}$$

Equation 4.3 Neural event synchronization index equation for spontaneous electrophysiology.

To identify clusters of synchronized electrodes, first, the participation index (PI) was calculated for each electrode *a* that contributed to a cluster *b*:

$$PI_{ab} = \lambda_b v_{ab}^2$$

Equation 4.4 Participation index equation for spontaneous electrophysiology.

where v_{ab} was the a^{th} element of eigenvector v_b and λ_b was the corresponding eigenvalue. PI_{ab} indicated the contribution of electrode *a* to the synchronized cluster *b*, with v_{ab}^2defined as the weight with which electrode *a* contributed to cluster *b*.

Next, randomized surrogate time-series data without any correlated electrode pairs were generated with an event rate equal to the instantaneous event rate of the experimental recordings, and the eigenvalues of the surrogate correlation matrix were calculated (Li *et al.*, 2010b). The surrogate randomization was repeated 50 times and the mean ($\bar{\lambda}'_k$) and standard deviation (SD_k) of surrogate eigenvalues were calculated (k = 1, …, M, where M was the number of electrodes). We identified the number of synchronized clusters that were significantly different from the randomized, asynchronous surrogates by:

$$Number\ of\ Clusters = \sum_k sgn\left[\lambda_k > \left(\bar{\lambda}'_k + K \times SD_k\right)\right]$$

Equation 4.5 Synchronized cluster equation.

where *sgn* was a sign function, λ_k was the eigenvalue of each electrode of the experimental data, and *K* was a constant (*K* = 3, for 99% confidence level, for a given number of electrodes).

Finally, a global synchronization index (GSI), ranging from 0 (completely random, uncorrelated activity) to 1 (perfectly synchronous, correlated activity), was calculated for the cluster with the highest degree of synchronization:

$$GSI = \begin{cases} \dfrac{\lambda_M - \bar{\lambda}'}{M - \bar{\lambda}'}\ if\ \lambda_M > \bar{\lambda}' \\ 0\ otherwise \end{cases}$$

Equation 4.6 Global synchronization index (GSI) equation.

where $\bar{\lambda}'$ was the mean of the highest eigenvalues calculated across all surrogates, λ_M was the maximal eigenvalue of the correlation matrix from the experimental data, and M was the number of electrodes.

To account for differences in the number of electrodes in each hippocampal region, the percentage of electrodes from each region in the cluster with the highest synchrony was calculated by dividing the number of electrodes in each region in the cluster with the highest synchrony by the total number of electrodes within a region in the entire hippocampal slice. The percentage of electrodes in each region in that cluster was multiplied by the GSI to obtain a normalized GSI for each region.

4.2.4 Statistical Analysis

Nonlinear regression was performed to relate changes in spontaneous (neural event rate, duration, and magnitude), stimulus-response (R_{max}, I_{50}, and m), and paired-pulse (PPR for Short Term ISIs, Early-Mid ISIs, Late-Mid ISIs, and Long Term ISIs) electrophysiological parameters to injury parameters (tissue strain and strain rate). Empirical functions were fit for the cortex using the MATLAB function *nlinfit.m* and 95% confidence intervals were computed using the function *nlparci.m* (MathWorks). All electrophysiological parameters were fit separately.

The functional forms of the candidate fit equations were polynomials in strain and strain rate (including interaction terms) with powers up to 3. This family of polynomials was chosen based on the general shape of the data, its gradients, and degree of non-linearity with respect to

the independent variables of strain and strain rate. To determine the best-fit equation from the family of 8,190 equations for each electrophysiological parameter, with an optimal number of terms to preserve parsimony, *k*-fold cross-validation was performed across all candidate equations, with 10 folds iterated 10 times. In *k*-fold cross-validation, a data set consisting of *n* samples is randomly split into *k* subsets (called folds), with each subset consisting of approximately *n / k* samples. Each of the *k* folds is used as a test fold, with the remaining *k – 1* folds serving as training folds. All candidate equations are fit to the data in the training fold, then applied to the data in the test fold, and the sum of squared errors (SSE) is calculated (Guo *et al.*, 2008). This process is repeated for each of the *k* test folds and the SSE is averaged over *k*. To account for random resampling variance, *k*-fold cross-validation is usually iterated with different random permutations of training and test folds (Ounpraseuth *et al.*, 2012). A common choice of *k* is 10, and 10 to 30 iterations of 10-fold cross-validation have been shown to minimize random resampling variance (Molinaro *et al.*, 2005). For *R* iterations of *k*-fold cross-validation for data with *n* experimental samples, the mean squared error (MSE) is calculated, and the fit equation with the minimum MSE is chosen as the best-fit equation:

$$MSE = \frac{1}{R}\sum_{l=1}^{R}\frac{1}{k}\sum_{j=1}^{k}\sum_{i=1}^{n}\left(e_i - \hat{e}_{ijl}\right)^2$$

Equation 4.7 Equation for k-fold cross validation for electrophysiology best fit equations.

in which e_i was the actual experimental value of the i^{th} sample and $\hat{e}_{ijl}$ was the predicted value of the i^{th} sample of the j^{th} data fold of the l^{th} iteration.

Finally, a linear hypothesis test was performed for each coefficient in the best-fit equation using the MATLAB function *coefTest.m* (MathWorks) to test significance of regressed coefficients ($p < 0.05$).

4.3 Results

For all electrophysiological parameters, at most, five terms were necessary to optimally fit the raw data (Table 4.1).

Parameter	K	Constant	Strain	Strain^2	Strain^3	Rate (s)	Rate^2 (s^2)	Strain* Rate (s)	Strain^2* Rate (s)	Strain^2* Rate^2 (s^2)	Strain^3* Rate (s)
Event Firing Rate	1	0.025 (s^{-1}) ±0.006									
Event Duration	1	9.03 (s) ±1.59									
Event Magnitude	4	29.7 (μV) ±2.7			226.46 ±204.79					0.56 ±0.31	-26.9 ±21.4
Rmax	5	306 (μV) ±126	2295 ±1724	-6170 ±4577					-349 ±281		992 ±660
I50	5	48.44 (μA) ±12.16	308.46 ±180.94	-796.45 ±500.56				-16.02 ±11.39	49.69 ±32.98		
m	4	0.103 (μV/μA) ±0.026	-0.81 ±0.48	3.41 ±2.06	-3.92 ±2.50						
Short Term PPR	2	0.857 ±0.033					0.0003 ±0.0002				
Early-Mid PPR	2	1.046 ±0.042		-0.54 ±0.48							
Late-Mid PPR	2	1.043 ±0.037			-0.98 ±0.95						
Long Term PPR	2	1.077 ±0.028				-0.00364 ±0.00297					

Table 4.1 Fit equations for electrophysiological parameters in the cortex. Values are presented as ±95% confidence interval. K, number of terms.

For changes in spontaneous electrophysiological function, neural event rate (Figure 4.1A) and duration (Figure 4.1B) did not change significantly after mechanical injury, and their fit functions contained only a constant term. Only neural event magnitude was dependent on the independent variables strain and strain rate, with magnitude generally increasing as strain and strain rate increased (Figure 4.1C).

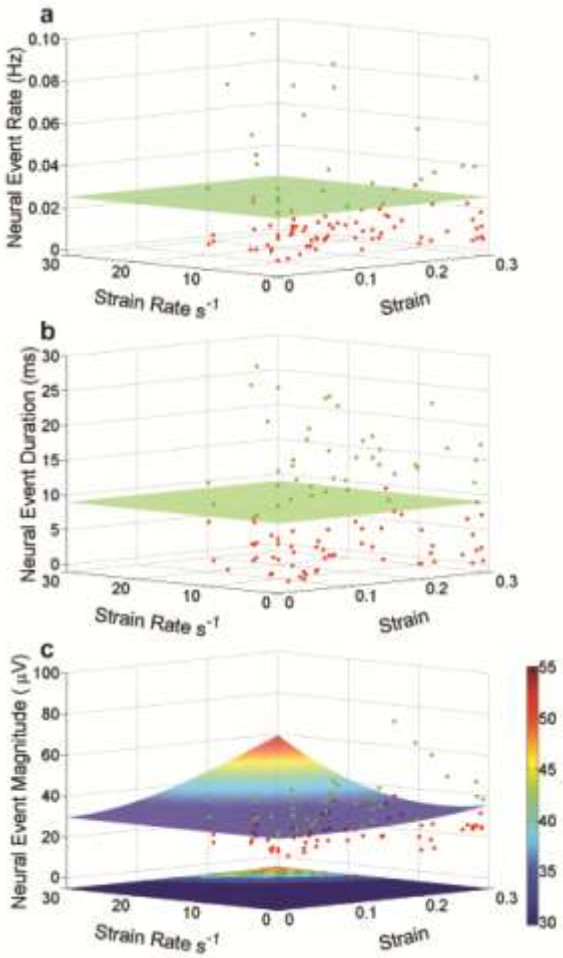

Figure 4.1 Alterations in spontaneous electrophysiology of the cortex in response to mechanical stimuli (tissue strain and strain rate). Raw data points are plotted above (green) and below (red) the surface representing the fit equation. A contour plot is included for visualization purposes. (A) Neural event rate

was independent of both strain and strain rate. (B) Neural event duration was independent of both strain and strain rate. (C) Neural event magnitude was dependent on strain and strain rate in a complex manner and generally increased as strain and strain rate increased.

Changes in R_{max} after mechanical injury were dependent on strain and, minimally, on strain rate (Figure 4.2A). Changes in I_{50} were dependent on both strain and strain rate in a complex manner (Figure 4.2B). Maximum values of I_{50} were predicted at approximately 0.2 strain at very low strain rates ($< 5\ s^{-1}$) while minimum values of I_{50} were predicted at approximately 0.1 strain at high strain rates ($> 25\ s^{-1}$). Changes in m were dependent on strain, but independent of strain rate (Figure 4.2C). As strain increased, m generally decreased or did not change significantly.

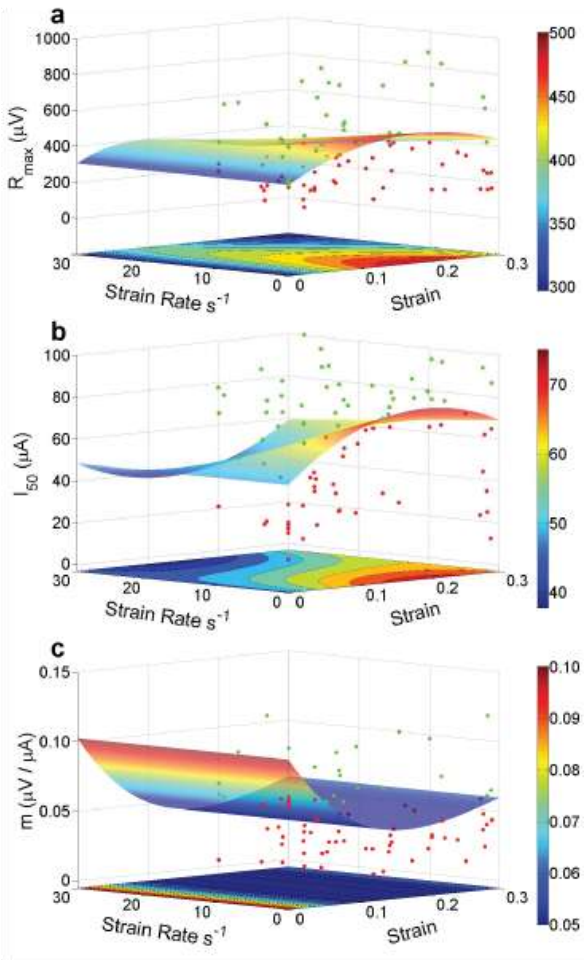

Figure 4.2 Alterations in evoked responses of the cortex as a function of mechanical injury parameters of tissue strain and strain rate. Raw data points are plotted above (green) and below (red) the surface representing the fit equation. A contour plot is included for visualization purposes. (A) R_{max} was dependent on both strain and strain rate in a complex manner. (B) I_{50} was dependent on both strain and strain rate in a complex manner. (C) m was dependent on strain but independent of strain rate.

Changes in PPR in each ISI bin were described optimally with only two terms. Changes in PPR for Short Term (Figure 4.3A) and Long Term (Figure 4.3D) ISIs were dependent only on strain rate, while PPR for Early-Mid (Figure 4.3B) and Late-Mid (Figure 4.3C) ISIs were

dependent only on strain. PPR for Short Term ISIs exhibited the greatest amount of perturbation after mechanical injury, increasing from paired-pulse depression to paired-pulse facilitation as strain rate increased.

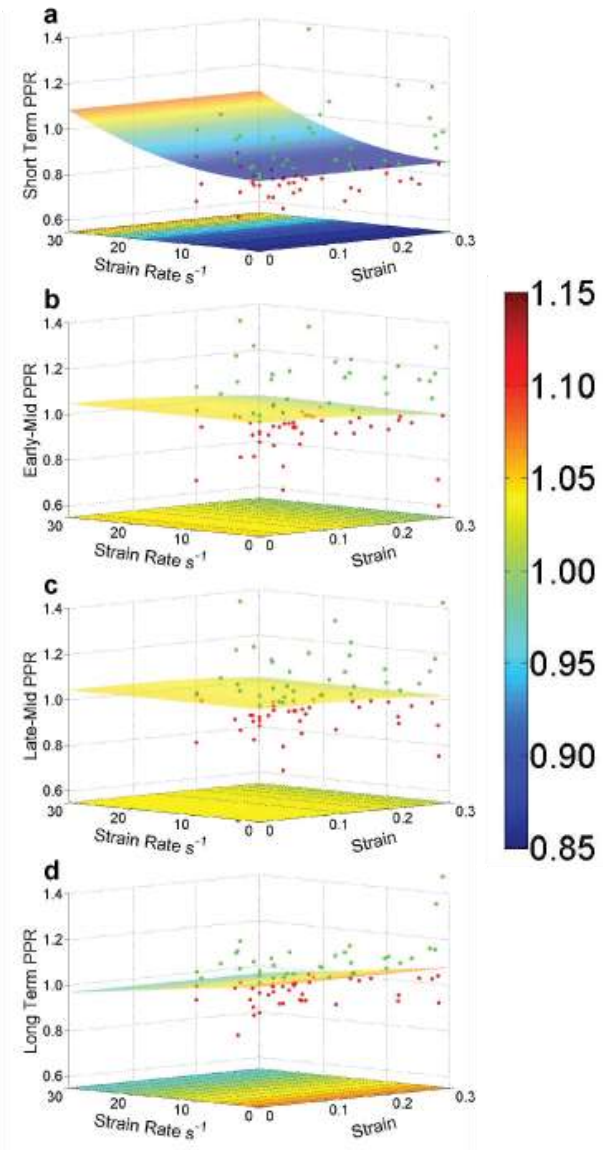

Figure 4.3 Alterations in paired-pulse ratios for the cortex in response to mechanical stimuli (tissue strain and strain rate). Raw data points are plotted above (green) and below (red) the surface representing the fit

equation. A contour plot is included for visualization purposes. (A) PPR for Short Term ISIs was dependent only on strain rate. (B) PPR for Early-Mid ISIs was dependent only on strain. (C) PPR for Late-Mid ISIs was dependent only on strain. **d** PPR for Long Term ISIs was dependent only on strain rate.

In the cortex, three parameters were necessary to optimally fit the raw data (Table 4.2). Similar to the hippocampus, the normalized GSI was also dependent only on strain rate, but in a nonlinear manner (Figure 4.4). The normalized GSI decreased with increasing strain rate up to approximately 10 s^{-1}, but then increased as strain rate increased, peaking at high strain rates (30 s^{-1}).

Region	K	Constant	Rate	$Rate^2$	$Rate^3$
Cortex	3	0.087 ±0.027	-0.0090 ±0.0069	0.00038 ±0.00034	

Table 4.2 Fit equations for the normalized GSI of cortex. Values are presented as ±95% confidence interval. K, number of terms.

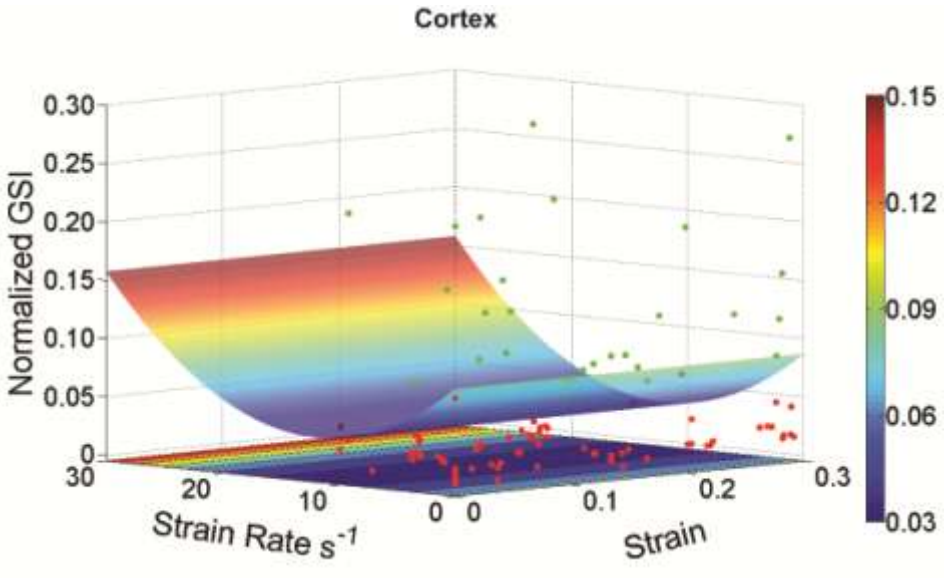

Figure 4.4 Alterations in network synchronization of the cortex in response to mechanical injury parameters defined as tissue strain and strain rate. Raw data points are plotted above (green) and below (red) the surface representing the best fit equation. A 2D contour plot was included for visualization purposes. The normalized GSI was dependent only on strain rate.

4.4 Discussion

We have developed functional tolerance criteria for the cortex based on alterations in electrophysiological function after precisely controlled and verified mechanical deformation. Optimal fit equations were determined from a large pool of candidate equations by ten-fold cross-validation to account for the tradeoff between model (equation) complexity and goodness of fit, thus avoiding overfitting. Our strategy preserved parsimony, with all fit equations requiring no more than 5 terms without sacrificing significant prediction accuracy.

The predicted functional tolerance criteria for the cortex differed substantially when compared to results for hippocampus (Kang and Morrison, 2014). In the hippocampus, even

small changes in strain and strain rate were predicted to elicit large changes in spontaneous activity. In the cortex, in contrast, no change in neural event rate or duration were observed across all combinations of strain and strain rate, with only neural event magnitude exhibiting any dependence on strain and strain rate (Figure 4.1). This difference could be due to the inherent differences between the cortical and hippocampal neuronal networks, both morphologically (Juraska and Fifkova, 1979) and functionally (Dalva and Katz, 1994, Garaschuk *et al.*, 2000). In the hippocampus, spontaneous network oscillations involve a large number of neurons acting together in a frequent, regular pattern (Garaschuk *et al.*, 1998). In contrast, cortical spontaneous oscillatory activity is detected only in individual neurons (Flint *et al.*, 1999) or very small, discrete "neuronal domains" made up of only 2 – 50 neurons (Yuste *et al.*, 1992, Schwartz *et al.*, 1998). In the cortex, significantly fewer neurons function in concert, even in the uninjured state, to initiate detectable spontaneous activity, which could explain the lack of detectable change after injury. There are also fewer neural events to detect in general. Using calcium imaging as a surrogate for neural activity, Garaschuk *et al*. reported calcium transients at very low rates, recurring approximately once every 1 – 12 minutes. In our study, 54% of the cortical slices in our data set had average rates of less than 1 event per minute per electrode. It may be possible that the chosen recording window did not capture irregular and infrequent spontaneous network oscillations.

The cortical neuronal network was also less active, less excitable, and less coordinated than the hippocampal neuronal network, evidenced by the evoked response data (Figure 4.2). R_{max} in the cortex was never greater than 500 μV after any mechanical stimulus, whereas the average, uninjured R_{max} in hippocampus was above 500 μV in all hippocampal regions and increased to values above 1000 μV after severe mechanical stimuli (Kang and Morrison, 2014).

The comparatively lower activity levels in cortex may be a direct result of the lower density of neurons, and more importantly, the lower density of functional synaptic contacts in the various cortical layers (Blue and Parnavelas, 1983b). Because R_{max} is a correlate for the total number of functional synaptic contacts (Buchs *et al.*, 1993), the difference in R_{max} between cortex and hippocampus is most likely due to the difference in the density of functional synaptic contacts in the cortex and hippocampus.

The cortex was also significantly less excitable compared to the hippocampus (Figure 4.2B). In the hippocampus, I_{50} only varied between 20 to 40 μA, whereas in the cortex, I_{50} fluctuated between approximately 40 to 70 μA. In the developing cortex, synaptic contacts are sparsely distributed throughout the cortical layers and synaptic connectivity is weak (Katz and Shatz, 1996), not reaching full maturity until the end of the fourth postnatal week (Blue and Parnavelas, 1983a). At the time of the electrophysiological experiments, the cortical slice cultures had been in culture for 11-17 days and were originally generated from P8-11 rat pups. Assuming they continued to mature in culture at the same rate *in vivo*, they could be considered equivalent to P18-28. Therefore, the cortical network within the cultures may have been slightly immature, requiring stronger stimuli to efficiently propagate excitation to enough neurons to result in a summed field potential. The brain of a rat aged P18-28 is believed to be similar developmentally to the brain of a human between the ages of 2-11 years old based on common developmental milestones in the juvenile brain (Dobbing and Sands, 1979, Tsujimoto, 2008, Semple *et al.*, 2013). Therefore, our model may be especially relevant to juvenile TBI, a leading cause of long-term neurodegenerative deficits in infants and young children (Langlois *et al.*, 2005, Selassie *et al.*, 2008).

The electrophysiological parameter m approximates the complexity of the neuronal population, in that a low value of m (shallow slope of the linear portion of the S/R curve) indicates a diverse pool of neurons with a wide distribution of firing thresholds (Devanne *et al.*, 1997, Pitcher *et al.*, 2003). Conversely, a larger value of m (steeper slope of the S/R curve) may be indicative of the whole population of neurons possessing a similar threshold to fire. In the cortex, m peaks at approximately 0.1 at injuries of low strain (Figure 4.2C). In contrast, m in the hippocampus may reach maximal values greater than 0.3. Due to the variability in firing characteristics of neurons in different layers of the cortex and the local clustering of neurons into "neuronal domains," the excitability of neurons may be more variable with less uniformity than in the hippocampus (Wu *et al.*, 1999, Wu *et al.*, 2001).

PPR at Short Term ISIs was dependent only on strain rate and switched from depression at low strain rates to facilitation at high strain rates (Figure 4.3A). In the visual cortex, frequency-dependent paired-pulse depression observed under normal conditions is believed to be a dynamic gain-control mechanism (Abbott *et al.*, 1997, Galarreta and Hestrin, 1998), and at short ISIs, paired-pulse depression is dominated by GABAergic-mediated inhibition (Jia *et al.*, 2004). As strain rate increases, GABAergic-mediated disinhibition or dysfunction may be occurring, resulting in the observed reversal of depression to facilitation.

Previous studies quantified functional tolerances to mechanical injury by measuring changes in electrophysiological properties at specific strains and strain rates (Bain and Meaney, 2000). Bain and Meaney determined conservative, liberal, and best overall thresholds of Lagrangian strain for the prediction of morphological and functional injury in guinea pig optic nerve (Bain and Meaney, 2000). Their tolerances were developed using a model of pure axons undergoing uniaxial stretch as opposed to the heterogeneous population of neural cells present in

organotypic slice cultures that were biaxially deformed in the present study. Bain and Meaney determined distinct thresholds of injury using logistic regression, in contrast to the complex predictions determined in the present study. The complexity of our data is not surprising considering the tissue architecture of the cortex and its effects on electrophysiological function. Neurons in different layers of the cortex exhibit layer-specific firing characteristics (Sun and Dan, 2009), and neurons in each cortical layer can form their own "small-world networks" with sparse long-range connections in between layers (Douglas *et al.*, 1995, Watts and Strogatz, 1998). Combined with more complex mechanical stimulation (biaxial vs. uniaxial deformation), the electrophysiological response to injury may not be expected to demonstrate a linear, monotonic relationship with injury severity.

Our data set could be incorporated into current FE models of TBI, adding functional outcomes to the mechanical outputs that simulate the events in the brain during and after injury. An example is provided to illustrate the utility of this approach. Viano *et al*. studied the influence of brain tissue deformation (strain and strain rate) on ensuing concussion symptoms by reconstructing specific helmet-to-helmet collisions in the National Football League (NFL) via high-speed video analysis and dummy simulations (Viano *et al.*, 2005). The physical injury reconstruction data was then used as inputs to an FE model of the brain to predict the strain and strain rate experienced by various regions of the brain during and after the collision (Zhang *et al.*, 2001b). One particular collision was found to induce strain of 0.12 at a strain rate of 28 s^{-1} in the orbitofrontal cortex region of the struck player. The struck player was reported to suffer from headaches and dizziness, as well as impaired cognition and short term memory. Within their patient cohort, Viano *et al*. discovered a correlation between strain in the orbitofrontal cortex and dizziness. The fit equations presented herein can predict the injury-induced changes in the

stimulus-response and paired-pulse function within the cortex of the struck player for comparison to the expected electrophysiological function of an uninjured player (Figure 4.5).

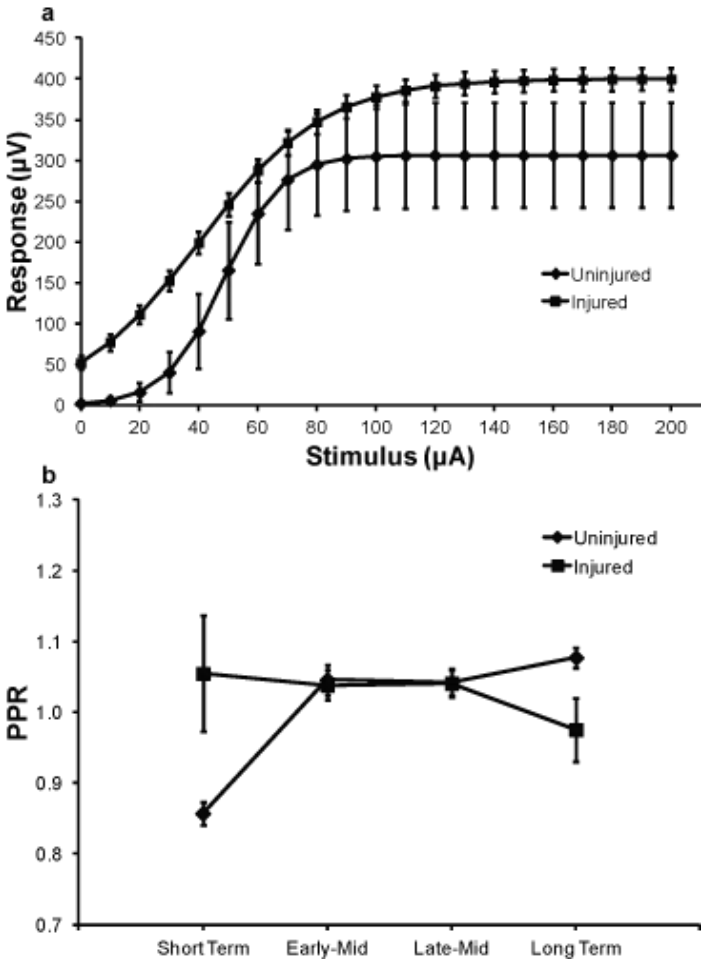

Figure 4.5 Changes in stimulus-response activity and paired-pulse ratios generated from fit equations in response to a particular impact. Tissue strain (0.12) and strain rate (28 s^{-1}) from a helmet-to-helmet collision as determined by Viano *et al*. were used as inputs to the fit equations developed herein. (A) S/R curves were generated using the equations for R_{max}, I_{50}, and m. (B) Paired-pulse data was plotted for PPR for Short Term, Early-Mid, Late-Mid, and Long Term ISIs (mean±SD).

The upward and leftward shift of the S/R curve due to injury is caused primarily by an increase in R_{max} and a decrease in I_{50} (Figure 4.5A). R_{max} is a correlate for the total number of functional synaptic contacts and therefore a measure of neuronal network connectivity (Buchs *et al.*, 1993). I_{50} was defined as the stimulus current necessary to evoke a half-maximal response, reflecting the synaptic excitability of the neural circuitry (Yu and Morrison, 2010). In the case of the injured player, the cortical network is predicted to become hyperexcitable after the collision, with more neurons firing in a coordinated manner (R_{max} increase) with a lower firing threshold (I_{50} decrease). Cortical hyperexcitability has been implicated in the symptoms related to migraine, including headache and dizziness (Welch *et al.*, 1990, Haigh *et al.*, 2012). Thus, the changes in the S/R curve of the struck player that are indicative of hyperexcitability may help explain the migraine-like symptoms that resulted from the specific tissue deformations from the helmet-to-helmet collision.

At tissue strain of 0.12 and strain rate of 28 s^{-1}, our fit equations predict facilitation in PPR for Short Term ISIs rather than paired-pulse depression that is expected in the uninjured case (Figure 4.5B). In healthy, uninjured cortex, paired-pulse depression at Short Term ISIs is mediated by $GABA_A$ receptors (Jia *et al.*, 2004). Cortical GABAergic interneurons regulate excitability through feedforward and feedback inhibition (Lee *et al.*, 2010), and GABAergic dysfunction in the cortex has been implicated as a significant factor in cognitive and memory impairments (Lewis, 2000). The reversal of paired-pulse depression to paired-pulse facilitation in the Short Term ISIs could be indicative of GABAergic dysfunction, which could help explain the cognitive and short term memory impairments experienced by the struck player.

A direct correlation between *in vitro* electrophysiology in animal models to behavioral changes in humans has not been previously validated, so the preceding discussion is somewhat

speculative. However, TBI is known to cause alterations in intracellular signaling cascades (Atkins *et al.*, 2007b, Ning *et al.*, 2013), neurotransmitter receptor subunit expression (Giza *et al.*, 2006, Lee *et al.*, 2011), neurotransmitter receptor function (Tavalin *et al.*, 1997, Lea *et al.*, 2002), and neuron morphology (Gao and Chen, 2011). The summation of all of these microscopic changes after TBI may manifest as changes in electrophysiological function, which represent their cumulative effects on the neuronal network. Findings from electrophysiology studies in rodent tissue are often translated to understanding electrophysiology in human neural tissue (Cohen *et al.*, 2007, Reeves and Colley, 2012). In addition, the cellular- and tissue-level changes after TBI in rat and human brains may be similar despite the macroscopic differences in structure (Shreiber *et al.*, 1999). Therefore, since changes in electrophysiological function are the cumulative effect of cellular and molecular perturbations, it may be possible to justify a comparison between the mechanotransduction of tissue strain and strain rate into changes in electrophysiological function in our animal study and the human condition. Electrophysiological experiments involving cultured human brain tissue could more directly address this limitation.

Another limitation is the range of tissue strains and strain rates achieved with our *in vitro* model of TBI in the current study. While it has been reported that the injury device is capable of producing strains up to 1.00 and strain rates up to 150 s^{-1} (Morrison *et al.*, 2003, Elkin and Morrison, 2007), we were able to achieve a maximum tissue strain of 0.59 and a maximum strain rate of 26 s^{-1}. This experimental range was due to imperfect adhesion of the slice culture to the PDMS substrates, which decreased the percentage of the applied substrate strain experienced by the slice culture. This limitation is common to all injury models based on deformation of the culture substrate. One of the strengths of our *in vitro* injury model is the use of high-speed video to validate the applied tissue strain to correlate outcome to the actual tissue biomechanics.

A combination of physical injury reconstruction and FE modeling of helmet-to-helmet collisions of NFL players reported that a collision with a 50% probability of concussion featured gray matter strain and strain rate of 0.26 and 48.5 s^{-1}, respectively (Kleiven, 2007). Other numerical studies have implicated even higher brain strains and strain rates in moderate to severe TBI, although they have not been validated for predicting tissue strain or strain rate (Kimpara and Iwamoto, 2012, Post *et al.*, 2012). The strain rate in the reconstructed collision by Kleiven would surpass the upper bound in our data set, with extrapolated predictions from our fit equations potentially becoming less accurate. Therefore, caution should be exercised when attempting to interpret changes in electrophysiological function in response to tissue deformations in excess of the maximal values in our data set. Our data set may be most appropriate for simulations of mild to moderate TBI, which produces strains and strain rates within the domain and range of our injury parameter data.

5 Stretchable Neural Interfaces[4]

5.1 Introduction

Neural engineering holds great promise for improving the lives of millions of people who have lost the ability to interact with the world due to disease, injury, or congenital defects. Neural engineering requires an interface with the nervous system to record neural electrical activity and enable bi-directional communication through stimulation of neural tissue. Neural prostheses directly interface with neurons and potentially could overcome cognitive, behavioral, and motor deficits caused by peripheral nerve injury, amputation, spinal cord injury, degenerative motor neuron disease, and many other neurodegenerative conditions. The interface between living neural tissue and the man-made, engineered system is the microelectrode array (MEA), which critically determines the functionality, utility, and stability of the benefit gained from the neural prosthesis. In fact, the quality of the interface between neurons and the device may dictate the overall functional quality of the entire system. If the interface is non-stationary over time, with decreasing signal to noise ratio (SNR) or loss of individual neurons (information), the robustness of the system as a whole will deteriorate.

The interface between the circuitry and the neural tissue or cells is most often achieved through a matrix or array of electrodes. By recording from many electrodes, the information content of the signal is greatly increased over that of single electrodes (Mehring *et al.*, 2003, Cohen and Nicolelis, 2004, Carmena *et al.*, 2005). Given the distributed processing and storage of information in the brain, recording from an extended network of interacting neurons may be

[4] A modified version of this chapter previously appeared in print: Kang, W.H., Cao, W., Wagner, S. and Morrison, B. (2012). Stretchable Neural Interfaces. In: Stretchable Electronics. Wiley-VCH Verlag GmbH & Co. KGaA, pps. 379-399.

more effective than single electrode interfaces (Engel *et al.*, 2001, Harris *et al.*, 2003). Increased information content is critical for accurate decoding of the neural signal and the resultant prediction of the intended output. For example, in a brain-computer interface, single neuron activity may be correlated with motion parameters, but ensemble recordings produced more precise movements and enable better reproducibility (Cohen and Nicolelis, 2004, Carmena *et al.*, 2005).

Contemporary MEAs allow for simultaneous recording from up to 256 discrete locations with recording bandwidths of up to 30 kHz (Charvet *et al.*, 2010). The long-range connectivity of neural networks can be studied with these arrays, providing additional insight into neuronal information processing and function over single electrode recordings (Kralik *et al.*, 2001, Diogo *et al.*, 2003). Higher order behaviors are likely to depend on this type of ensemble network behavior rather than the activity of individual neurons (Doetsch, 2000).

To facilitate coupling of MEAs to neural tissue and the study of neuronal networks within tissue, a multitude of MEA concepts and designs has been demonstrated for application to in vivo neural tissue, in vitro cell culture, and brain slice electrophysiology. Electrodes have been fabricated from many materials including gold, platinum, iridium, titanium nitride, silicon, carbon, and conductive polymers. Electrode arrays are typically configured as either planar, cuff, penetrating, or regenerating electrodes (Lacour *et al.*, 2010). Planar electrodes patterned on flat, most often rigid substrates are designed for extracellular stimulation and recording in vitro of various types of tissues or cells (Yu and Morrison, 2010). Cuff electrodes are coiled arrays wrapped around nerves with interior electrode contacts (Donaldson *et al.*, 2008). Penetrating electrodes are implantable arrays that typically feature long, needle-like structures pushed into the brain or nerve in vivo (Cheung, 2007, Kim *et al.*, 2009). Regenerating electrodes feature a

sieve of surface electrodes implanted between severed ends of a peripheral nerve to facilitate the regrowth of nerve fibers (Edell, 1986).

Most MEA systems are practically rigid in comparison to soft neural tissues (Table 5.1).

Material	Young's Modulus
Brain	3 kPa (Elkin et al., 2011a, Elkin et al., 2011b)
Peripheral Nerve	575 kPa (Borschel et al., 2003)
Spinal Cord	650 kPa (Bilston and Thibault, 1996)
Polydimethylsiloxane (PDMS)	1 MPa (Walker et al., 2004)
Polyimide	2.8 GPa (McClain et al., 2011)
Parylene C	4.8 GPa (Shih et al., 2004)
Bone	16 GPa (Rho et al., 1993)
Thin Film Gold	55 GPa (Espinosa and Prorok, 2003)
Glass	76 GPa (Chen et al., 1995)
Platinum	165 GPa (Merker et al., 2001)
Silicon	170 GPa (Hopcroft et al., 2010)

Table 5.1 Typical Young's Modulus (E) for SMEA materials and neural tissues.

In vivo penetrating MEAs consist of needle-like electrodes made from silicon or metal wires which have Young's moduli (E) on the order of tens to hundreds of GPa (McClain *et al.*, 2011). Less rigid arrays for *in vivo* implantation that integrate stiff components on flexible polymer substrates such as polyimide have been developed but with E of approximately 3 GPa

(Cheung *et al.*, 2007). Small flexion of these flexible MEAs can be achieved without altering their functionality (Suo *et al.*, 1999). However, even these flexible MEAs are much stiffer than neural tissues and cannot withstand mechanical strains in excess of 1-2% (Lacour *et al.*, 2010). Flexible MEAs are not compliant enough to tolerate large mechanical deformations that occur physiologically for neural tissue. With each beat of the heart or due to movement of the head, the brain, for example, experiences up to 5% bulk strain (Bayly *et al.*, 2005, Sabet *et al.*, 2008), and peripheral nerves may experience up to 15% strain (Topp and Boyd, 2006). Contemporary *in vitro* planar MEAs are formed on glass substrates, and are therefore rigid and incompatible with deformation (Egert *et al.*, 1998, van Bergen *et al.*, 2003). These structures fracture under small tensile strain, typically no more than 1% (Spaepen, 2000).

The modulus mismatch between rigid MEAs (E of tens to hundreds of GPa), flexible MEAs (E on the order of GPa) (McClain *et al.*, 2011) and brain tissue (E of approximately 3 kPa) (Elkin *et al.*, 2011a, Elkin *et al.*, 2011b) or peripheral nerves (E of approximately 600 kPa) (Borschel *et al.*, 2003) poses many acute and chronic problems, stemming from implantation trauma, interfacial strains and micro-motion damage (Polikov *et al.*, 2005, Subbaroyan *et al.*, 2005, Cheung, 2007). With the inclusion of a rigid electrode, tissue stress and strain become concentrated very locally around the electrode, leading to repetitive mechanical stimulation and injury. Over time, these contribute to inflammation at the implantation site (Cheung *et al.*, 2007), encapsulation of the electrode (Cheung, 2007), neuronal death in the surrounding brain tissue (Biran *et al.*, 2005), and loss of SNR (Polikov *et al.*, 2005). Additionally, MEA systems that require tethering to the skull or another external anchor exacerbate the inflammation and neuronal cell loss around the electrodes (Kim *et al.*, 2004, Biran *et al.*, 2007).

To avoid the deleterious effects caused by this mechanical mismatch between man-made MEA systems and biological tissues and cells, softer, more compliant electrodes are necessary to improve the tissue-electrode interface. In a theoretical modeling study, significant tissue strains were generated at the interface with stiff electrodes with material properties representative of silicon or polyimide (Subbaroyan *et al.*, 2005). Most interestingly, in simulations of a hypothetical electrode made of a soft material with E = 6 MPa (similar to silicone), interfacial strains were reduced by two orders of magnitude. Softer, more compliant, and stretchable MEAs are capable of moving and deforming with the tissue, thereby reducing this repetitive micro-motion damage and improving the longevity of the interface.

Stretchable MEAs (SMEAs) also have utility for *in vitro* studies to understand mechano-transduction, the cellular pathways by which mechanical stimuli are transduced into intracellular signaling cascades. Many of these *in vitro* systems apply mechanical stimulation by deformation (stretch) of an elastic substrate on which the cells or tissue grow. Such systems have found utility in the study of traumatic brain injury (Morrison III *et al.*, 1998, Morrison III *et al.*, 2011), which is caused by rapid deformation of the brain, including stretch, compression, and shear strain (Cater *et al.*, 2006, Elkin and Morrison, 2007). As described above, most contemporary MEAs are rigid and therefore not compatible with these injury models, making it difficult to study the effects of mechanical injury on electrophysiological function of the neuronal network. While it is possible to injure neural tissue after removing it from an MEA, recording from the same locations after injury is very difficult. An SMEA embedded in the elastic substrate lifts these limitations because the tissue remains adhered to the SMEA before, during, and after stretch injury (Yu *et al.*, 2009b). Examples of this *in vitro* application for SMEAs, developed by us, and examples of *in vivo* applications, developed by others, are described below.

5.2 Classes of SMEAs

Contemporary SMEAs fall into one of two categories: planar or cuff SMEAs. Many MEAs have been described in the literature as being flexible and capable of functioning while being rolled or bent. Induced bending strains range up to a few percent (Lacour *et al.*, 2010). In an arbitrary definition that takes practical needs into account, we consider a stretchable MEA to be defined as one which can withstand at least 20% uniaxial or at least 5% biaxial strain without losing electrical continuity.

5.2.1 Planar SMEAs

Planar SMEAs provide spatial and temporal information about neuronal networks and have the additional advantage of being capable of monitoring neural electrophysiological activity from tissues or cells subjected to mechanical deformation and injury (Yu *et al.*, 2009a). For planar SMEAs, elastically stretchable electrodes are patterned on a substrate of elastomeric silicone, typically biomedical grade polydimethylsiloxane (PDMS). They have been designed for extracellular stimulation and recording from neural tissues and cells *in vitro,* such as acute and organotypic hippocampal brain slices or primary dissociated neuron cultures (Graudejus *et al.*, 2009). They also have the potential for long-term *in vivo* implantation (Henle *et al.*, 2011). The current planar SMEA strategies feature three primary designs, each with key differentiating qualities. The first was fabricated on a PDMS substrate with a second layer of photopatternable silicone to serve as an encapsulant (Graudejus *et al.*, 2009); the second used wire bonding for connections and PDMS as an encapsulant (Kitzmiller *et al.*, 2006); the third used laser

micromachining to structure conducting platinum foil as well as insulating layers of PDMS (Henle *et al.*, 2011). Each is described below in the order that they were reported in the literature.

The first design featured a silicone (PDMS, Sylgard 184, Dow Corning) substrate, on which gold thin-film conductors (3 nm chromium, followed by 75 nm gold, finished with 3 nm chromium) were deposited by electron beam evaporation (Figure 5.1) (Graudejus *et al.*, 2009).

6

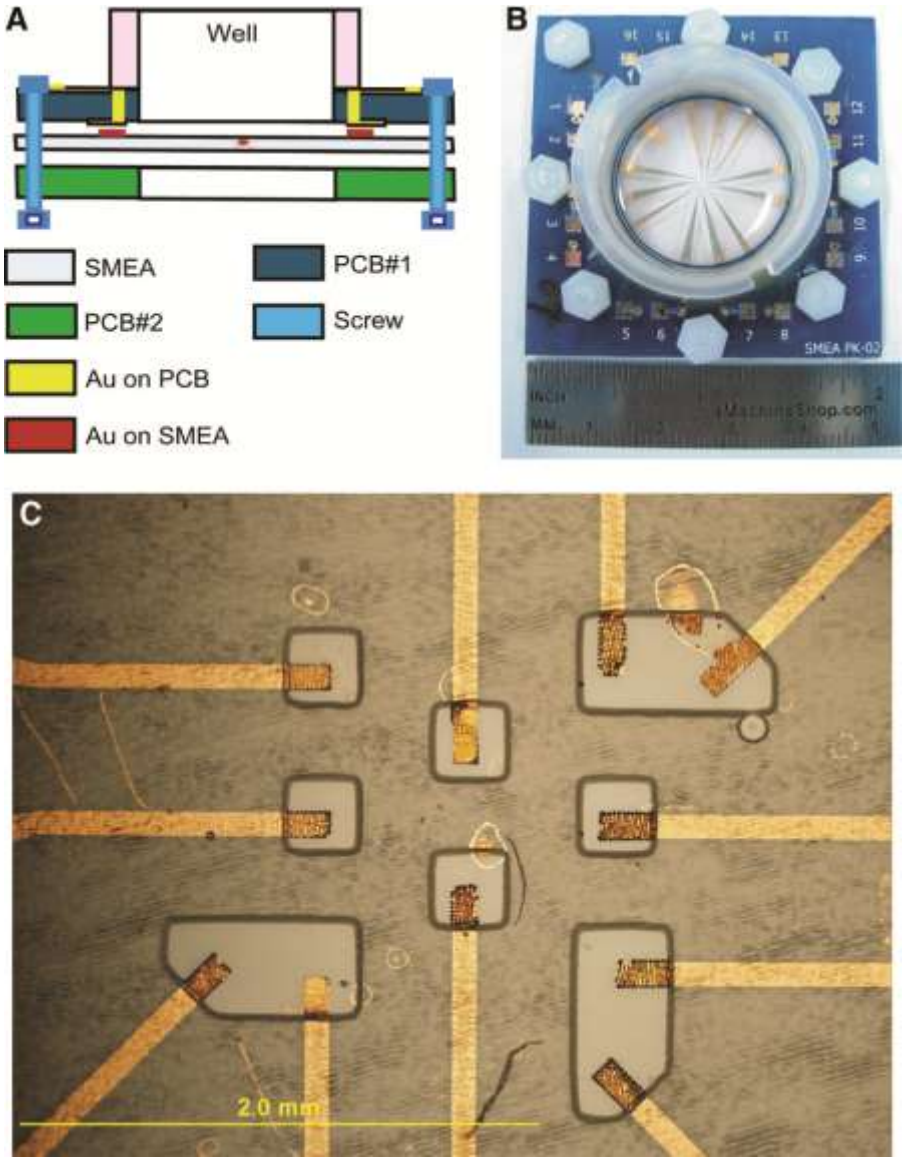

Figure 5.1 Schematic and image of the SMEA and electrode contacts from (Yu, Z., et al. 2009a). (**A**) After fabrication, the SMEA was clamped between two printed circuit boards (PCBs). The metal pads on the PCB were electrically connected with contact pads on the SMEA using silver paste. A plastic cylinder was cemented on the top PCB to form a tissue culture chamber. (**B**) Top-view image of the SMEA package. (**C**) Image of the SMEA electrode array. 11 recording electrodes (100 μm x 200 μm) and 1 reference electrode (not shown) were exposed by photopatterned vias and were coated by platinum black to reduce electrode impedance. Figure reprinted with permission from (Yu *et al.*, 2009a).

The PDMS substrate was not pre-stretched, and the resulting thin-film was not buckled (Lacour *et al.*, 2006). Instead, deposition was controlled to make the thin film adopt a microcracked morphology that was critical to its ability to stretch, as described below (Graudejus *et al.*, 2010). The gold film was patterned into electrodes by photolithography and etching. The patterned electrodes were encapsulated with an approximately 15 μm thick layer of photopatternable silicone (PPS, WL5150, Dow Corning). By photolithography, vias were opened in the PPS to the recording electrodes and peripheral contacts. An early version of the SMEA had 11 recording electrodes (100 μm x 200 μm), 1 reference electrode, and 12 peripheral contacts. To interface the peripheral contacts with a commercial amplifier, the SMEA was sandwiched between two printed circuit boards (PCBs) with circular openings in their centers to form a tissue culture well. The SMEA and PCBs were bolted together; metal pads on the PCB were electrically connected with the pads on the SMEA using silver paste. A plastic cylinder was attached with epoxy to the center of the upper PCB, to form a well. To reduce the impedance between the recording electrodes and the tissue culture, platinum black was electroplated on the surfaces of the recording electrodes in the center of the culture well. In the present design, SMEAs with 28 electrodes were fabricated with feature sizes < 100 μm (Graudejus *et al.*, 2012). A major challenge of microfabrication on PDMS is that many conventional process steps cannot be transferred directly to it, and require significant efforts for their adaptation (Graudejus *et al.*, 2009, Minev and Lacour, 2010).

The morphology of the thin-film gold conductor was critical for maintaining electrical continuity during and after the SMEA was stretched (Li *et al.*, 2004, Lacour *et al.*, 2005, Lacour *et al.*, 2006). The stretchable gold films formed a continuous network that was defined by

disconnected cracks on the micrometer scale (Lacour *et al.*, 2003, Gorrn *et al.*, 2011). As the PDMS substrate strain was increased, the microcracks widened and lengthened reversibly. During uniaxial strain, cracks continued to open in the stretch direction, but cracks actually closed in the perpendicular direction due to Poisson compression (Cao *et al.*, 2011). Conduction was maintained by percolation through a network of conducting ligaments. At very large strain, the microcracks coalesced locally producing a crack that runs across the electrode and breaks conduction (Li *et al.*, 2004, Lacour *et al.*, 2005, Cao *et al.*, 2011). Bare thin-film conductors have withstood uniaxial strains in excess of 60% for 1000s of cycles (Lacour *et al.*, 2005).

Under the much harsher condition of biaxial deformation, Poisson compression cannot occur in the plane of the thin-film. Instead, to accommodate the substrate strain, the metal film twisted and deflected out of plane (Lacour *et al.*, 2006). The substrate between the metal ligaments stretched while the strain in the film remained below its failure limit. The result was that the relatively rigid and fragile metal thin-film was capable of undergoing large biaxial strains; completed SMEAs withstand up to 12% biaxial strain while maintaining conduction (Lacour *et al.*, 2006, Lacour and Adrega, 2010).

These SMEAs have been utilized in neurotrauma studies, in which organotypic hippocampal brain slice cultures from P8-P11 Sprague-Dawley rats were mechanically injured to simulate traumatic brain injury *in vitro*. Brain slice cultures were mechanically stimulated by stretching the SMEA over a hollow cylinder, thereby inducing an equi-biaxial strain in the SMEA culture substrate and the attached tissue (Yu *et al.*, 2009a). Tissue and SMEA deformation was verified by image analysis. Both spontaneous and evoked electrophysiological signals were recorded with a sampling rate of 20 kHz. Evoked activity was induced by constant current stimulation with a biphasic, bipolar, constant current, rectangular pulse (positive phase

for 100 μs followed by negative phase for 100 μs, in 10 μA increments from 0 μA to 150 μA) applied through two of the SMEA electrodes. Field potentials from the neuronal network were recorded while the SMEA was stretched and relaxed. Cultures were maintained and recorded from for up to 19 days with no adverse, cytotoxic reactions to the PDMS or gold electrodes (Yu *et al.*, 2009a).

The SMEA was evaluated for functionality before, during, and after mechanical stretch (Figure 5.2A, B). The impedance at 1 kHz of individual recording electrodes in conductive medium (i.e. tissue culture medium or a physiological salt solution) was 50-150 kΩ before stretch, increased to approximately 2750 kΩ during 11% biaxial stretch, and recovered during relaxation to baseline levels when completely relaxed. The SMEA was able to record extracellular activity at biaxial strains below 8% (Yu *et al.*, 2009a). Recent improvements in encapsulation and fabrication strategies have resulted in an SMEA with smaller feature size and an increased number of electrodes, as well as increased fabrication yield and reproducibility (Graudejus *et al.*, 2012). The improved SMEA was able to record spontaneous and evoked field potentials at biaxial strains of up to 10% (Figure 5.2C, F). However, low signal-to-noise ratio (SNR) at higher strains remains a challenge. In additional tests, the mechanical robustness of the SMEA was assessed by repeated cycles of stretching to different strain levels (ten times to 10% biaxial strain, ten times to 20% biaxial strain, and 10 times to 30% biaxial strain). After cyclic stretching, the SMEA remained functional in its relaxed state with very low electrical noise of 1.86 μV root mean square noise (Yu *et al.*, 2009a).

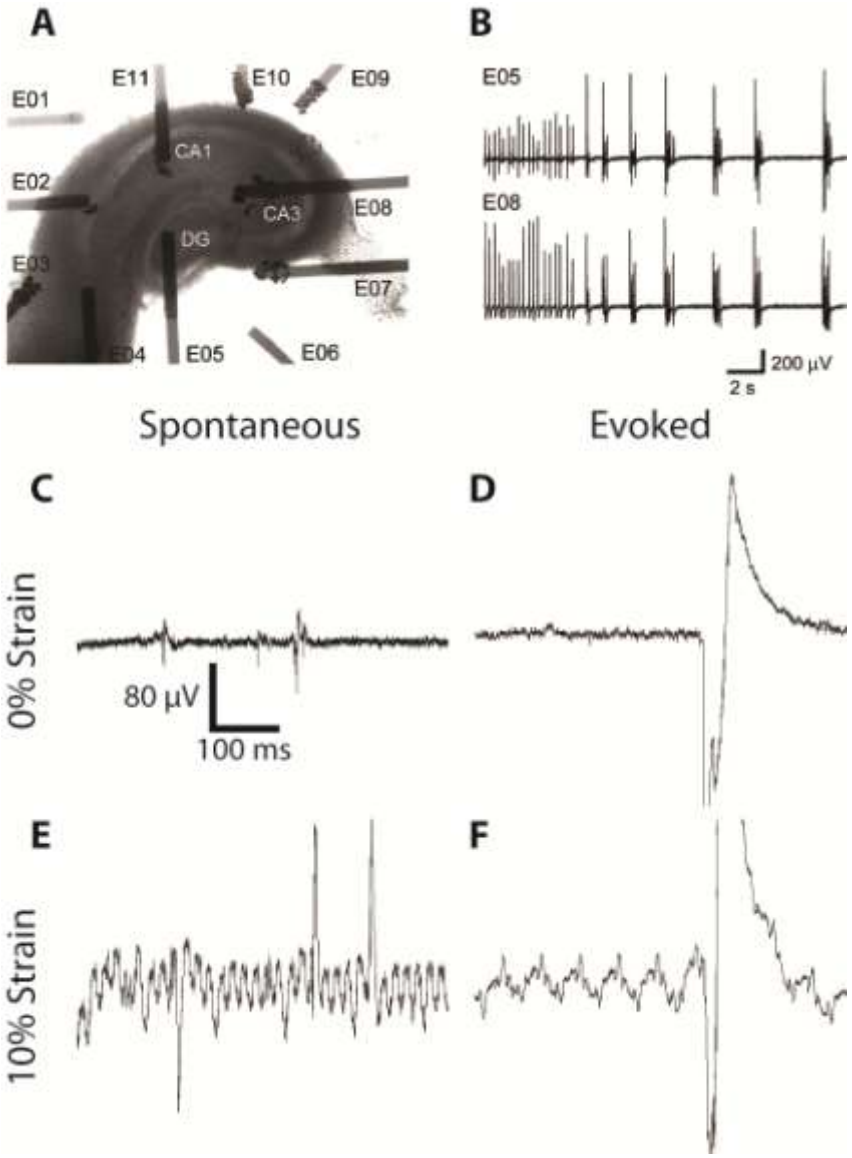

Figure 5.2 Spontaneous activity and evoked field potentials of an injured hippocampal slice culture using the SMEA from (Yu, Z., et al. 2009a) and (Graudejus, O., et al. 2012). (**A**) An optical micrograph of a hippocampal slice cultured on an SMEA. At 5 days *in vitro* (DIV), the tissue and SMEA were biaxially stretched to 8% strain, and spontaneous activity and evoked field potentials were recorded with the SMEA for an additional 9 days post-injury. (**B**) Immediately post-injury, spontaneous and continuous bursting was observed simultaneously on multiple electrodes. (**C**) Spontaneous activity of a healthy slice before mechanical stimulation. (**D**) Evoked field potentials from the same slice in response to a stimulus of 40 µA. (**E**) Spontaneous activity of the same slice during 10% biaxial strain applied to the SMEA and

adhered tissue. (**F**) Evoked field potentials of the same slice during 10% biaxial strain applied to the SMEA and adhered tissue (stimulus parameters as in D). Note the increased electrical noise (~60 μV) of the recordings during biaxial strain due to increased electrode resistance. A and B reprinted with permission from (Yu *et al.*, 2009a).

There were some limitations associated with this SMEA. The electrical interface between the flexible PDMS and the rigid PCB, which acted as a carrier and provided contact pads for the amplifier, required a conducting silver paste for good electrical contact. The number of contacts that fit along the edge of the PCB was limited so that silver paste did not short adjacent contacts. To achieve low-noise recordings, the exposed electrodes were coated with platinum black. Over time, the platinum black coat was thinned out and the SNR decreased, requiring occasional replatinization for optimal performance. These SMEAs were not compatible with conventional steam autoclaving, which damaged the conductors due to the mismatch in thermal expansion between the PDMS and the gold. Treatment with hydrogen peroxide as a cleaning agent has proven to be sufficient for sterilizing SMEAs unable to withstand conventional steam autoclaving.

A second planar SMEA utilized wire bonding to interface platinum electrodes with data acquisition hardware (Figure 5.3A) (Kitzmiller *et al.*, 2006). Its fabrication process began by spin coating photoresist on to a silicon wafer, which was then patterned. Electron beam evaporation was used to deposit a platinum film on the surface of the photoresist and exposed silicon. Stripping the photoresist layer left behind an array of platinum electrode contacts (200 μm square) on the silicon substrate. Aluminum wires, 30 μm in diameter, were ultrasonically bonded to the platinum contacts and the entire interface was encapsulated in flexible,

biomedical-grade PDMS (MDX4-4210, Dow Corning). The encapsulated array was then peeled from the rigid silicon backing to produce a free-standing array of electrodes. Electrical integrity testing measured an average resistance of 0.574 Ω across each electrode and interfacing wire indicating that the wire-bonding and liftoff processes were successful.

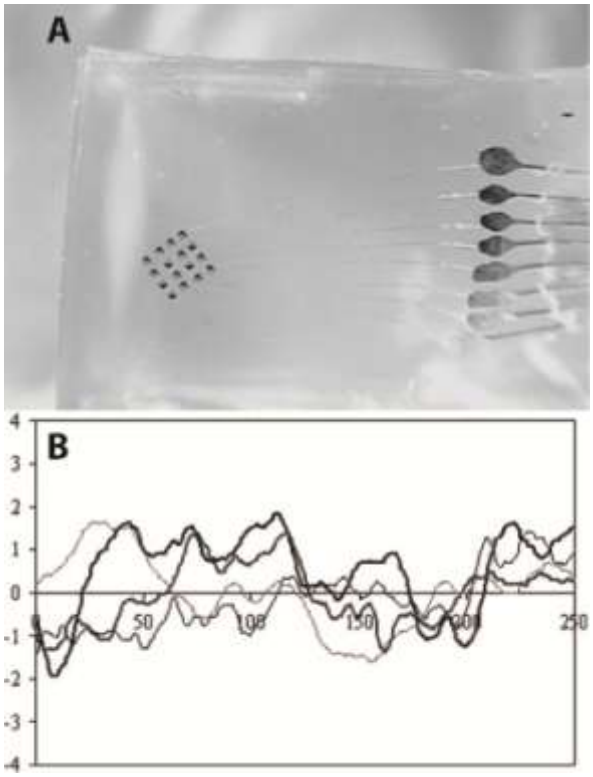

Figure 5.3 Optical micrograph of wire-bonded SMEA from (Kitzmiller *et al.*, 2006). (**A**)Wire bonds were permanently bonded to platinum electrode contacts (200-μm square) (*left*) and held in place within a PDMS layer. The wire-bonded SMEA may not be able to stretch and function at strains high enough for relevant physiological applications. (**B**) Visual evoked potentials (VEP) from the subdural occipital cortex of a domestic pig. Four potentials were recorded from the left eye during stimulation. Voltage (mV) is plotted against time (ms), with visual simulation occurring at time = 0. Reprinted with permission from (Kitzmiller *et al.*, 2006). Copyright 2006, Springer.

Primary cortical cells from rat pups and a cortical human cell line (HCN-1A) were cultured on the surface of the wire-bonded MEA and assayed for cell death to investigate the cytotoxicity of the electrode surface. No significant cytotoxicity was observed, indicating acceptable biocompatibility of the planar SMEA. Visual evoked potentials (VEPs) were collected from porcine subdural occipital cortex to verify electrical functionality in an acute *in vivo* preparation (Figure 5.3B).

The wire-bonded MEA may not be able to stretch and deform to strains high enough for physiologic applications (Bayly *et al.*, 2005, Sabet *et al.*, 2008). Extensive mechanical testing remains to be performed to quantify the mechanical tolerance of the array. The wire bonds also introduced challenges in efficient fabrication as each electrode contact required a separate wire bond to interface with data acquisition hardware. Because the electrode-wire constructs must remain physically separated or risk creating a short circuit, fabricating more than a handful of electrode-wire links may prove difficult and time-consuming. In these experiments, only 8 of the 16 electrodes were wirebonded because of this issue. Printed electronic circuitry may allow a higher number of electrodes for more functional arrays.

The final planar SMEA considered used the same silicone as the first SMEA (Sylgard 184) but patterned the PDMS insulator and platinum conductors by laser micromachining (Figure 5.4A) (Henle *et al.*, 2011). These arrays have been used for electrocorticography, and have been called electrocorticography-microelectrodes (Micro-ECoG) (Henle *et al.*, 2011). A Q-switched 1064 nm Nd:YAG marking laser (DPLGenesisMarker by cab, Karlsruhe, Germany) was used to pattern a base layer of PDMS, which was adhered to a glass slide. A 12.5 μm thick,

platinum foil was laminated onto the PDMS surface and patterned with the same laser. A second PDMS layer (25 μm thick) was spun on and laser-patterned to open up the 8 electrode contact sites (diameter 320 μm). A unique property of the Micro-ECoG was the incorporation of the Microflex interconnection to interface the silicone rubber/platinum foil electrode arrays to thick film ceramic substrates, which provide the bonding interface for a transcutaneous connector (Henle *et al.*, 2011). A 10 mm long stainless steel bar was also mounted on the ceramic substrate to improve mechanical fixation to the skull.

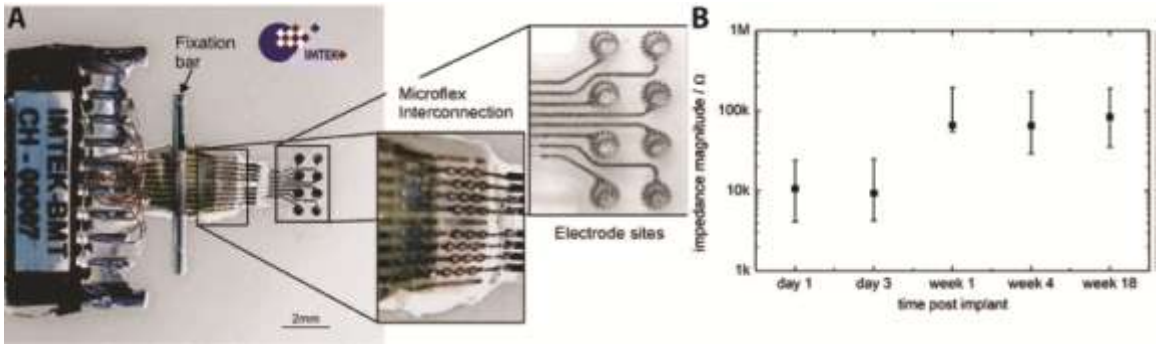

Figure 5.4 Fully assembled Micro-ECoG array from (Henle *et al.*, 2011). (**A**) A platinum foil was patterned by laser micromachining to produce the electrode pattern. Microflex connections were used to interface the PDMS/platinum foil to thick film ceramic substrates, which provided the bonding interface for a transcutaneous connector. A stainless steel fixation bar was used to improve mechanical fixation to the skull. (**B**) Impedance spectra of *in vivo* rat cortex measured by Micro-ECoG from (Henle *et al.*, 2011). The minima and maxima of impedance magnitude measurements at 1 kHz are shown over 18 weeks of implantation. Reprinted with permission from (Henle *et al.*, 2011). Copyright 2011, Springer.

The Micro-ECoG was implanted subdurally in young adult Wistar rats such that the 8-channel SMEA covered the right parietal cortex and parts of the visual cortex. Electrical impedance spectroscopy was conducted over an 18 week period, with access/tissue impedances increasing from 6 kΩ at 40 kHz on day one to 250 kΩ at 100 kHz 18 weeks after implantation (Figure 5.4B). This increase in access resistance was typical for chronically implanted microelectrodes (Williams *et al.*, 1999). Histological assessments performed 25 weeks after implantation showed minor pathological changes predominantly in the leptomeninges. Mild lymphoplasmacytic, but not granulating, inflammation was found in some cases, but most tissue damage was hypothesized to be caused by explantation and removal of the Micro-ECoG array. Neighboring brain tissue displayed subtle changes in reactive astrocytes and a few hypoxically-damaged neurons. However, most other neurons in the cortex were well preserved with little to no significant pathological changes, indicating that the Micro-ECoG could be successfully utilized in long-term, subdural cortical implantation studies.

One of the limitations of this study was that electrophysiological activity was not recorded over the 25 week implantation. Although electrical impedance spectroscopy was performed to determine the functional state of individual electrodes, whether they were actually capable of recording neuronal activity was not demonstrated. A second limitation was that the SMEA was not used to stimulate neural activity, leaving open the question whether it could actually perform its intended function.

5.2.2 Cuff SMEAs

Cuff SMEAs are coiled silicone arrays for bending and wrapping around peripheral or central nerves. The electrode contacts are on the interior of the cuff, and the mechanical design helps to ensure good contact with the nerve in the mechanically active environment of most nerves. Cuff electrodes may avoid some complications associated with penetrating MEAs, such as shear-induced inflammation caused by micromotion of the rigid penetrating electrodes embedded within the soft nerve (Cheung *et al.*, 2007). This repetitive micro-motion can lead to formation of an encapsulation layer around the electrodes that reduces SNR. Additionally, the foreign body and inflammatory responses induce neurotoxicity leading to a loss of neurons (Biran *et al.*, 2007). Similar to the planar SMEAs, cuff SMEAs were fabricated on PDMS substrates. Therefore, these devices had a low E of approximately 1 MPa (McClain *et al.*, 2011).

The first cuff SMEA was microfabricated using a novel reactive ion etch (RIE) process in an effort to better preserve the underlying gold that comprised the conductors (Meacham *et al.*, 2008). A 0.5 μm thick layer of gold was deposited by electron beam evaporation onto a glass slide backing to create a non-stick layer, before a 70 μm thick layer of PDMS (Sylgard 184) was spun on top of the gold layer. Electrodes were photolithographically patterned using standard positive-resist techniques before a 9.5 μm thick encapsulating layer of PDMS was applied. Vias were opened with a patterned aluminum film mask with a customized reactive ion etch (RIE). Significant effort was devoted to optimizing the custom RIE so as to maintain selectivity to cleanly etch the PDMS without damaging the underlying gold or appreciably etching the aluminum mask. The aluminum mask was then stripped and the complete SMEA was removed from the glass carrier.

Two configurations of the RIE SMEAs were evaluated for electrical and mechanical integrity under conditions pertinent to experimental electrophysiological recordings. One

configuration contained straight conductors while the other contained serpentine conductors (Figure 5.5). The impedance of the RIE SMEA electrodes in conducting medium was approximately 100 kΩ at 0.1 kHz and 3 kΩ at 100 kHz, which were comparable to those of rigid MEAs (Heuschkel *et al.*, 2002). The RIE SMEA with serpentine conductors was able to withstand uniaxial strains of up to 8% while continuing to conduct at impedances similar to rigid MEA electrodes. In contrast, the configuration with straight conductors lost conduction at 3% uniaxial strain.

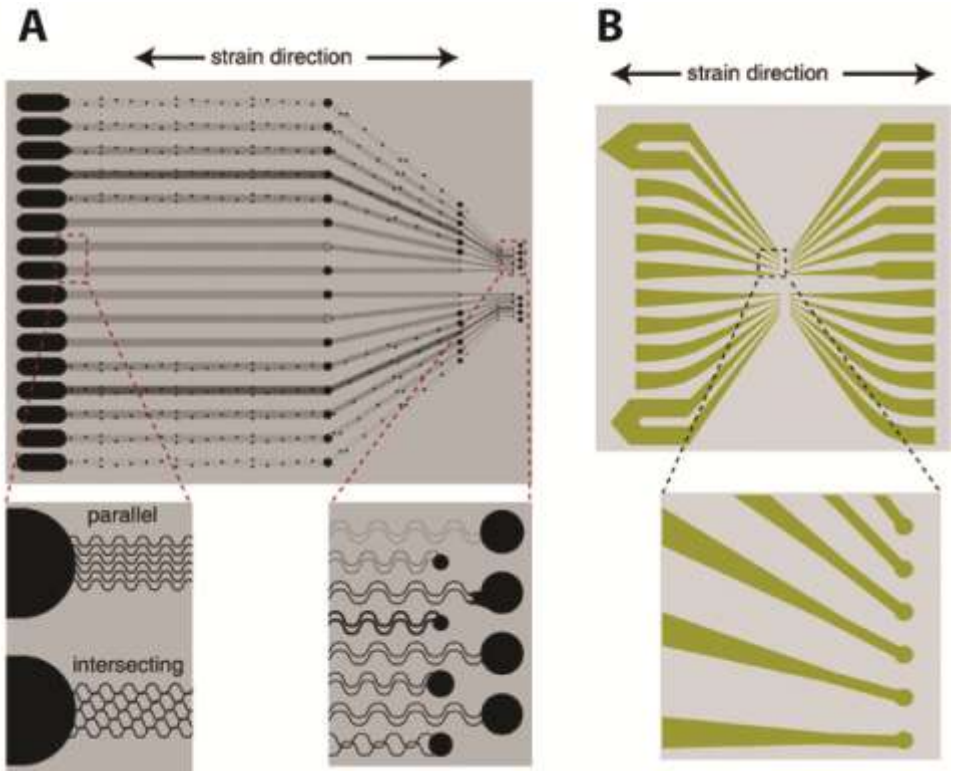

Figure 5.5 Serpentine and straight conductor patterns in the RIE cuff SMEA from (Meacham *et al.*, 2008). (**A**) The intersecting, serpentine electrode trace pattern was able to withstand uniaxial strains of up to 8% while continuing to function as an electrical conductor. (**B**) The straight electrode trace pattern lost

electrical conductivity at only 3% uniaxial strain. Reprinted with permission from (Meacham *et al.*, 2008). Copyright 2008, Springer.

The mechanism by which serpentine conductors withstand stretch has been examined in detail and is fundamentally different than the mechanism for cracked, metal films (Chen *et al.*, 2004, Sheiko *et al.*, 2007, Sun and Wang, 2007). The key design goal was to identify a path shape for the conductor that avoids strain concentrations above the failure limit of the conducting material. Optimization studies have identified a horseshoe shaped path comprised of multiple small conductors which was capable of uniaxial strains of 50-100% (Sheiko *et al.*, 2007, Sun and Wang, 2007). This serpentine pathway strategy worked with both thin-film and relatively thick (4 μm) metal layers (Sheiko *et al.*, 2007, Sun and Wang, 2007).

Using this cuff SMEA, electrophysiological viability was demonstrated in an *in vitro*, isolated spinal cord preparation from juvenile Sprague-Dawley rats (Meacham *et al.*, 2008). Bipolar, charge-balanced, constant current stimuli were applied to the spinal cord surface through two RIE SMEA electrodes, and evoked compound action potentials were recorded with a glass suction-electrode placed 11.5 mm distal. Thresholds to evoke responses were 700 μA applied for 500 μs, which compared favorably to the threshold for a penetrating tungsten electrode at 300 μA applied for 100 μs. One of the major limitations of this study was that neural activity was not recorded. Because the gold electrodes were not coated with platinum black, the charge transfer resistance between the gold and the electrolyte solution and tissue may have been excessive. High electrode impedance would result in substantial noise that could easily obscure neuronal activity, preventing successful recordings.

One challenge of working with PDMS is the opening of vias to expose electrode recording sites without damaging the underlying conductor. A second cuff SMEA employed an alternative to the customized RIE process or PPS described above. In this design, a liftoff resist was used to prevent coverage at the electrode locations by the subsequently applied encapsulation layer of PDMS. Removal of the resist resulted in well-formed circular vias with diameters of 120 μm (Figure 5.6). Fabrication of these cuff SMEAs was accomplished by first spin-coating PDMS (Sylgard 184) on a glass slide and then using a positive photoresist to define conducting traces. A metal stack of 30 nm titanium and 0.5 μm gold was deposited by electron beam evaporation, and the metal pattern developed. A negative photoresist was used as the liftoff resist layer that defined the vias for the electrode contacts before a second layer of PDMS (~10 μm) was applied. After removal of the sacrificial posts to open electrode contacts, the SMEA was removed from the rigid backing.

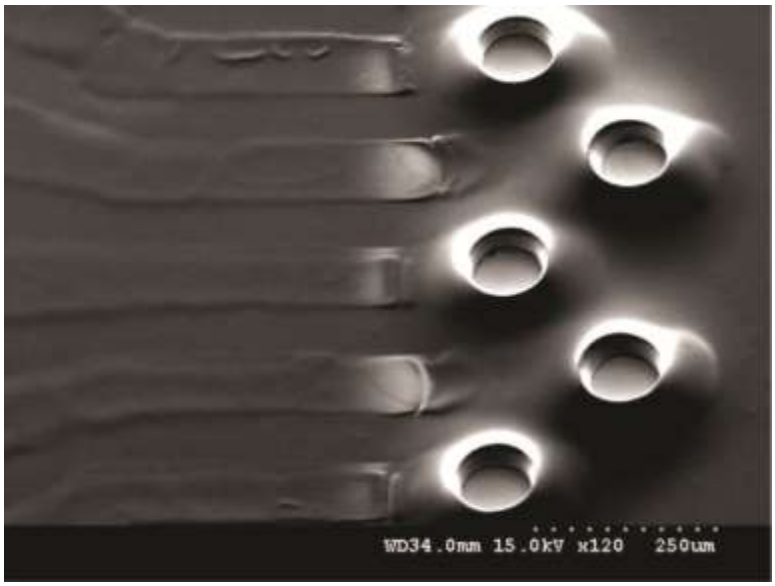

Figure 5.6 SEM image of the conical-well microelectrodes from (Guo *et al.*, 2010). Removal of the sacrificial posts exposed the underlying electrode contacts with a conical shape with top and bottom diameters of ~120 and ~100 μm, respectively. Reprinted with permission from (Guo *et al.*, 2010). Copyright 2010, IEEE.

The impedance of the resulting cuff SMEA electrodes was dependent on the spin speed at which the liftoff resist was applied. Slow spin speeds led to a thicker resist layer, more tapered liftoff posts, smaller electrode openings, and deeper electrode wells, all of which contributed to higher impedances. Impedances measured at 1 kHz ranged from 100kΩ at 400 rpm to 60kΩ at 1000rpm, which were comparable to other *in vitro* and *in vivo* MEAs. The ability to use this cuff SMEA as a neural interface was demonstrated in an *in vitro* spinal cord preparation (Guo *et al.*, 2010, Meacham *et al.*, 2011). The SMEA was wrapped around the excised spinal cord, and evoked responses were elicited by bipolar, monophasic, constant current stimuli (500 μA for 50 μs) (Guo *et al.*, 2010). In a follow-up study to further characterize the SMEA's ability to evoke responses, the threshold to evoke a response was similar to that for tungsten electrodes (153 μA versus 47 μA), using bipolar, biphasic, constant current pulses (Figure 5.7) (Meacham *et al.*, 2011). The ability to stimulate specific populations of neurons was also similar to that of tungsten electrodes. In both studies, neural activity was not recorded with the SMEA; instead, evoked responses were recorded with standard metal electrodes.

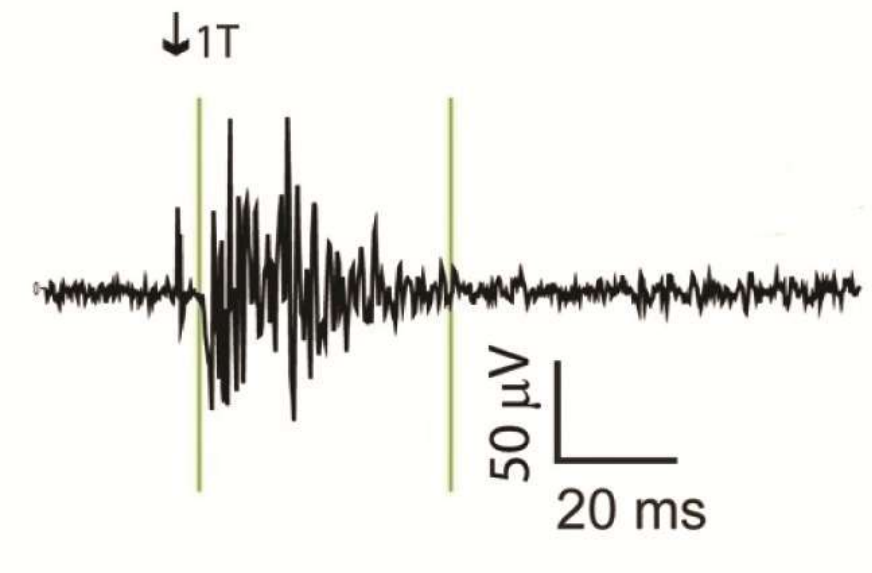

Figure 5.7 Recording of a compound action potential (CAP) in an *in vitro* spinal cord preparation evoked by an SMEA from (Meacham *et al.*, 2011). Arrow indicates the stimulus artifact, and the vertical lines surrounding the response indicate the onset and offset of the evoked CAP. This cuff SMEA utilized the sacrificial post scheme of exposing electrode recording sites without damaging the conducting layer. Reprinted with permission from (Meacham *et al.*, 2011). Copyright 2011, Meacham, Guo, DeWeerth and Hochman.

The final cuff SMEA considered here was comprised of a combination of PDMS and thin-film gold (30 nm), which was designed to wrap around small features (diameter ~ 1 mm) (Figure 5.8) (McClain *et al.*, 2011). PDMS was micro-molded in an SU-8 photoresist master mold followed by thermal evaporation of the metal conductors to form electrode contacts on long flexible PDMS cables. The SU-8 mold was patterned by standard photolithography on a silicon wafer and was filled by spin casting a mixture of Sylgard 184 and Sylgard 186. The authors found that the mixture improved the mechanical durability of the array without negatively affecting its ability to spin-cast. Using a shadow mask of brass foil, metal films, 5 nm chromium

followed by 30 nm gold, were thermally evaporated to form conducting traces on the PDMS cables. The metal traces were insulated with a second layer of PDMS with openings for the electrode contacts being formed by liftoff of a sacrificial photoresist. The elliptical electrodes measured 100 μm x 50 μm.

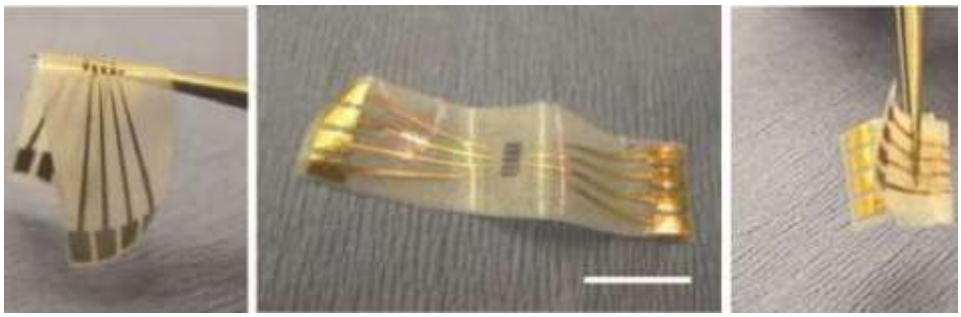

Figure 5.8 The PDMS-thin film gold cuff SMEA is shown in several different conformations from (McClain *et al.*, 2011). The cuff SMEA was designed to wrap around small features (diameter ~ 1 mm) and maintained conduction during uniaxial deformations of up to 7% and 9% strain. Scale bar: 1 cm. Reprinted with permission from (McClain *et al.*, 2011). Copyright 2011, Springer.

Mechanical testing of the microcable SMEA was performed at two strain ranges to determine the E of the composite gold on PDMS structures, which were 1.81 MPa at 10% strain and 1.62 MPa at 40% strain. Electromechanical response to strain was investigated by determining the strain-resistance profile after multiple cycles of 200% uniaxial strain. After five cycles of strain, electrical conductance was lost at 7% and 9% strain. As the number of cycles was increased to 1,000 or 5,000, baseline resistance increased in the unstrained configuration while the range of strain over which the cables were conductive decreased.

To test electrical function in an acute in vivo environment, the microcable SMEA was threaded around the sciatic nerve of an adult rat. Compound action potentials were evoked by stimulation through stainless steel electrodes and recorded with the SMEA (Figure 5.9). The shape of the recorded compound action potential was similar to that recorded with rigid metal electrodes verifying the feasibility of this design. Advantages of this array include its relatively low stiffness (approximately 1MPa) which was similar to peripheral nerves (approximately 600 kPa). The authors also calculated the theoretical bending stiffness of the SMEA and determined that it was an order of magnitude less than that of polyimide electrodes. The closer modulus match between peripheral nerve and this SMEA could reduce scarring and encapsulation during long-term implantation. One limitation of this study was that because common metal electrodes were used to stimulate the nerve only, it was unclear whether this design could deliver sufficient current to evoke neural responses.

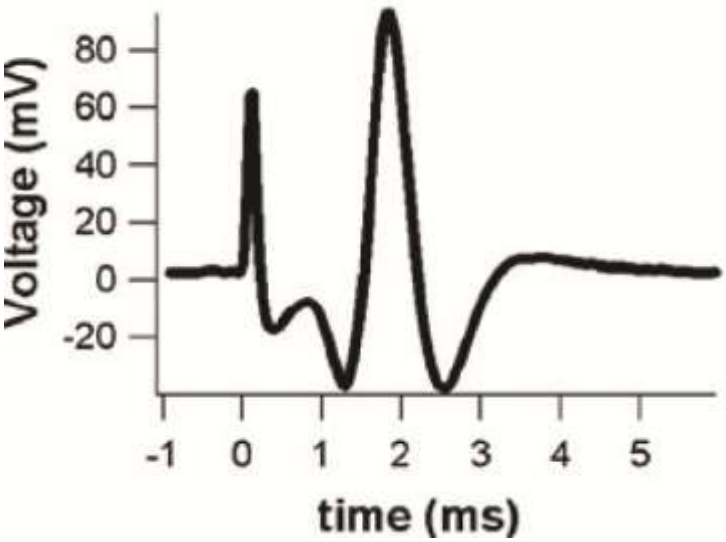

Figure 5.9 Compound action potentials were evoked by stimulation through stainless steel electrodes and recorded between a pair of SMEA microcables spaced 1 cm apart from (McClain *et al.*, 2011). The cuff SMEA was curled around the sciatic nerve to form a good contact. Reprinted with permission from (McClain *et al.*, 2011). Copyright 2011, Springer.

5.3 Common Limitations for All SMEAs

The technology of stretchable neural interfaces and stretchable electronics on which it builds is developing rapidly but is still in its early days. Contemporary SMEAs have some limitations in common. Feature sizes remain relatively large, generally between 50-100 μm, compared to rigid MEAs with feature sizes down to 10 μm. Consequently feature density is also relatively low, which becomes a major issue for routing conductors from the array of electrodes to external contacts. Most SMEAs are hybrid devices with electrodes on elastomeric substrates which conduct the biosignals to traditional rigid circuitry for amplification. The transition from the elastomeric substrates to rigid circuitry is a major design challenge, especially to produce a solution that is scalable. Guo and DeWeerth have developed a promising new process which can transition high-density conductors from PDMS to rigid substrates (DeWeerth and Guo, 2010). Their strategy offers advantages of both photolithographic control and multilayer fabrication, two features which will be necessary to accommodate dense electrode arrays and eventually embedded electronics (DeWeerth and Guo, 2010).

The ability of SMEAs to stretch can be a double-edged sword in some cases. Although the SMEA will deform with the neural tissue, its low modulus may complicate its attachment to mechanically active structures such as peripheral nerves. A secure but gentle attachment will be

necessary to prevent bulk migration of the SMEA while at the same time preventing stress and strain concentration in the nerve and the SMEA itself. The low modulus of SMEAs will make implantation into neural tissues difficult. This could be a major limitation for applications in the brain given the size of the organ and the internal location of certain target structures. All of the SMEA to date have been passive structures without any embedded electronics. SNR could potentially be improved by positioning head-stage amplifiers within the SMEA, close to the point of electrode contact. However, this would require future developments to produce active devices capable of withstanding the same stretch as the passive conductors. Active electronics for telemetry could also address the limitation that current SMEA designs require percutaneous connections, which provide a pathway for opportunistic infections.

5.4 Future Directions in Stretchable Neural Interfaces

Stretchable neural interfaces are evolving rapidly in parallel with innovations in microfabrication, micropatterning, and electronic circuitry. Successful long-term implantation *in vivo* is the next step in developing fully integrated neural interfaces. The challenges of long-term implantation are immense. SMEAs must be fully implantable and isolated from the outside environment to avoid infection. A high degree of biocompatibility is necessary to prevent inflammation and rejection of the neural interface. Kim *et al.* have developed a conformable electrode array fabricated on a dissolvable substrate of silk fibroin that is bioresorbable (Kim *et al.*, 2010). Bioresorbable MEA systems could potentially address the issue of long-term biocompatibility and enable long-term, real-time monitoring of electrophysiological activity while reducing the associated complications of a foreign-body response. Moving forward, fully

implantable neural interfaces must also address the challenge of wireless power transfer into the device and data transfer out of the device. A device capable of stimulation will further increase power demands. Fully implantable, wireless interfaces have been demonstrated with rigid arrays (Kim *et al.*, 2009).

The operational envelope of strains over which SMEAs function with good SNR is still limited to approximately 10% biaxial strain, but recent developments may help improve this performance. For example, Sekitani *et al.* have fabricated organic electronics capable of being bent with a radius of 100 μm, whereas previous circuits were limited to bending radii of several millimeters (Sekitani *et al.*, 2010). Graz *et al.* have manufactured stretchable thin-film transistors and interconnects on a PDMS substrate that is capable of sustaining applied strains of up to 13% while still maintaining electrical conductivity (Lacour *et al.*, 2011).These more mechanically robust, active components could be incorporated to boost the SNR of SMEAs. Rosset *et al.* have used metal ion bombardment of PDMS membranes to develop highly stretchable electrodes, with electrical conduction reported at uniaxial strains of up to 175% (Rosset *et al.*, 2009). It remains to be tested whether they will perform with similar mechanical robustness during biaxial deformation, but the promise of maintaining electrical conductivity at very high strains is evident.

Given the novelty of both the materials and fabrication steps, the yield of fully functional devices tends to be low. This low yield is further compounded by fabrication requiring custom and hands-on processing which poses an impediment to production scale-up. As a result, the cost per functional SMEA can be extremely high. Robinson *et al*. have reported reliable printing of soluble silver cluster ink onto PDMS substrates, with reversible deformation of tens of percent strain (Robinson *et al.*, 2011). Ahn *et al.* and Sekitani *et al.* have also reported successful

utilization of inkjet technology in manufacturing electrical circuitry (Sekitani *et al.*, 2008, Ahn *et al.*, 2009). Translating these fabrication techniques to stretchable neural interfaces could minimize the labor intensive microfabrication process, potentially increasing the yield of neural interfaces and decreasing their costs significantly.

5.5 Conclusion

SMEAs are an emerging technology which holds promise for both *in vivo* and *in vitro* applications. *In vivo*, they may increase the longevity and quality of neural interfaces for prostheses, thereby enhancing their overall functionality. *In vitro*, SMEAs open up new fields to study neural mechano-transduction and traumatic injuries of the nervous system. Interfacing the SMEA with traditional circuitry remains a considerable challenge, as does shrinking feature size. However, as the area of stretchable electronics matures, these challenges will be overcome as SMEAs become more sophisticated and offer greater functionality within the array.

6 Alterations in Hippocampal Network Activity after *In Vitro* Traumatic Brain Injury[5]

6.1 Introduction

Traumatic brain injury (TBI) continues to be a leading cause of death and disability (Hyder *et al.*, 2007, Gean and Fischbein, 2010), affecting nearly 10 million people annually worldwide and an estimated 1.7 million people annually in the United States (Faul *et al.*, 2010). The devastating behavioral and functional consequences of TBI include cognitive impairment (Kinnunen *et al.*, 2011), memory loss or impairment (Christidi *et al.*, 2011), loss or decreased consciousness (Ommaya and Gennarelli, 1974), motor deficits (Fujimoto *et al.*, 2004), coma (Margulies and Thibault, 1989), seizure and epilepsy (Asikainen *et al.*, 1999), and death (Sosin *et al.*, 1995).

Disruption of persistent working memory is a prominent cognitive deficit experienced by individuals with TBI (Hoskison *et al.*, 2009). In adults, the neural correlate for working memory and information storage may be recurrent network activity (Wang, 2001), which is also involved in neuronal network maturation in the developing brain (Buzsaki, 1989). In many cases, working memory deficits arise in the absence of cell death or overt structural damage to brain tissue especially in cases of mild or moderate TBI (McAllister *et al.*, 1999, Levin *et al.*, 2002, Kobori and Dash, 2006, Yu and Morrison, 2010).

[5] A modified version of this chapter previously appeared in print: Kang, W.H., Cao, W., Graudejus, O., Patel, T.P., Wagner, S., Meaney, D.F. and Morrison, B. 3rd (2014). Alterations in Hippocampal Network Activity after In Vitro Traumatic Brain Injury. J Neurotrauma. Reprinted with permission by Mary Ann Liebert, Inc.

TBI is caused by deformation of brain tissue, with tissue strain and strain rate identified as significant predictors of injury (Viano *et al.*, 2005, Cater *et al.*, 2006, Elkin and Morrison, 2007, Kleiven, 2007). However, very few studies have characterized *in vivo* tissue strain and strain rate during TBI due to the challenges of directly measuring tissue deformation *in vivo* (Bayly *et al.*, 2005, Bayly *et al.*, 2006, Hardy *et al.*, 2007). An *in vitro* approach to these mechanistic studies allows for precise control of the mechanical stimulus and the extracellular environment to examine the response of the brain parenchyma in the absence of systemic influences, while recapitulating much of the *in vivo* pathology (Morrison *et al.*, 1998, Hyder *et al.*, 2007).

One way to record *in vitro* neural activity is through the use of microelectrode arrays (MEAs) (Beggs and Plenz, 2004, Arnold *et al.*, 2005, Yu and Morrison, 2010). Compared to single electrode electrophysiological recordings, MEAs enable the investigation of higher order behaviors of neuronal networks comprised of up to many thousands of neurons, due to the ability to record simultaneously from multiple sites (Doetsch, 2000, Kralik *et al.*, 2001). One limitation of available MEAs is their rigid nature, which prevents direct testing of hypotheses relating changes in electrophysiological function to mechanisms of mechanotransduction. Previously, we demonstrated the ability to monitor electrophysiological function in hippocampal slice cultures after mechanical stretch injury using an earlier generation of SMEAs (stretchable microelectrode arrays) (Yu *et al.*, 2009a). In the present study, we leveraged the advantages of the latest generation of SMEA, with more recording electrodes and smaller feature-size, to test our hypothesis that long-lasting, hippocampal network synchronization is disrupted by TBI.

Recurrent network activity or synchronization is regulated by the inhibitory neurotransmitter γ-aminobutyric acid (GABA) (Matsuyama *et al.*, 2008). Disinhibition, caused

by disruptions in GABAergic signaling, may be a leading cause of pathologically persistent activity (Sloviter, 1994). Acutely, the $GABA_A$ antagonist bicuculline is used to induce epileptiform bursting activity in brain slice cultures by blocking GABAergic inhibition (De Curtis *et al.*, 1994) and to induce long-lasting, recurrent synchronous bursting, hours and days after washout (Arnold *et al.*, 2005, Li *et al.*, 2007b). By utilizing the unique capabilities of the SMEA to combine long-term electrophysiological recording with mechanical stimulation, we investigated the effect of mild to moderate mechanical stretch injury on bicuculline-induced, long-lasting network synchronization.

Our SMEA system has the potential to engender novel experimental strategies to investigate the mechanisms of mechanotransduction underlying the functional consequences of TBI. Compared to more labor intensive *in vivo* approaches, the ability to test TBI hypotheses within a single organotypic slice culture over extended durations could increase the speed of drug discovery through high-content screening (Sundstrom *et al.*, 2005).

6.2 Materials and Methods

6.2.1 Stretchable Microelectrode Arrays

Design, fabrication, and packaging of SMEAs have been described previously in detail (Lacour *et al.*, 2003, Tsay *et al.*, 2005, Graudejus *et al.*, 2012). Briefly, thin-film conductors (3 nm chromium, followed by 75 nm gold, finished with 3 nm chromium) were sequentially deposited on a 280 μm thick layer of polydimethylsiloxane (PDMS, Sylgard 184, Dow Corning, Midland, MI, USA) by electron beam evaporation (Graudejus *et al.*, 2009). The gold thin-film was patterned into recording electrodes and encapsulated with a 15 μm thick layer of either

PDMS or photo-patternable silicone (PPS, WL5150, Dow Corning). Vias were opened in the encapsulation layer to expose the recording electrodes and peripheral contacts. Platinum black was electroplated on the surfaces of the recording electrodes. The SMEA was sandwiched between two printed circuit boards with circular openings for the culture well and to allow incorporation into our *in vitro* TBI model (Morrison *et al.*, 2006). The SMEA featured 28 recording electrodes (feature size < 100 μm), 2 reference electrodes, and 30 peripheral contacts (Figure 6.1) (Graudejus *et al.*, 2012).

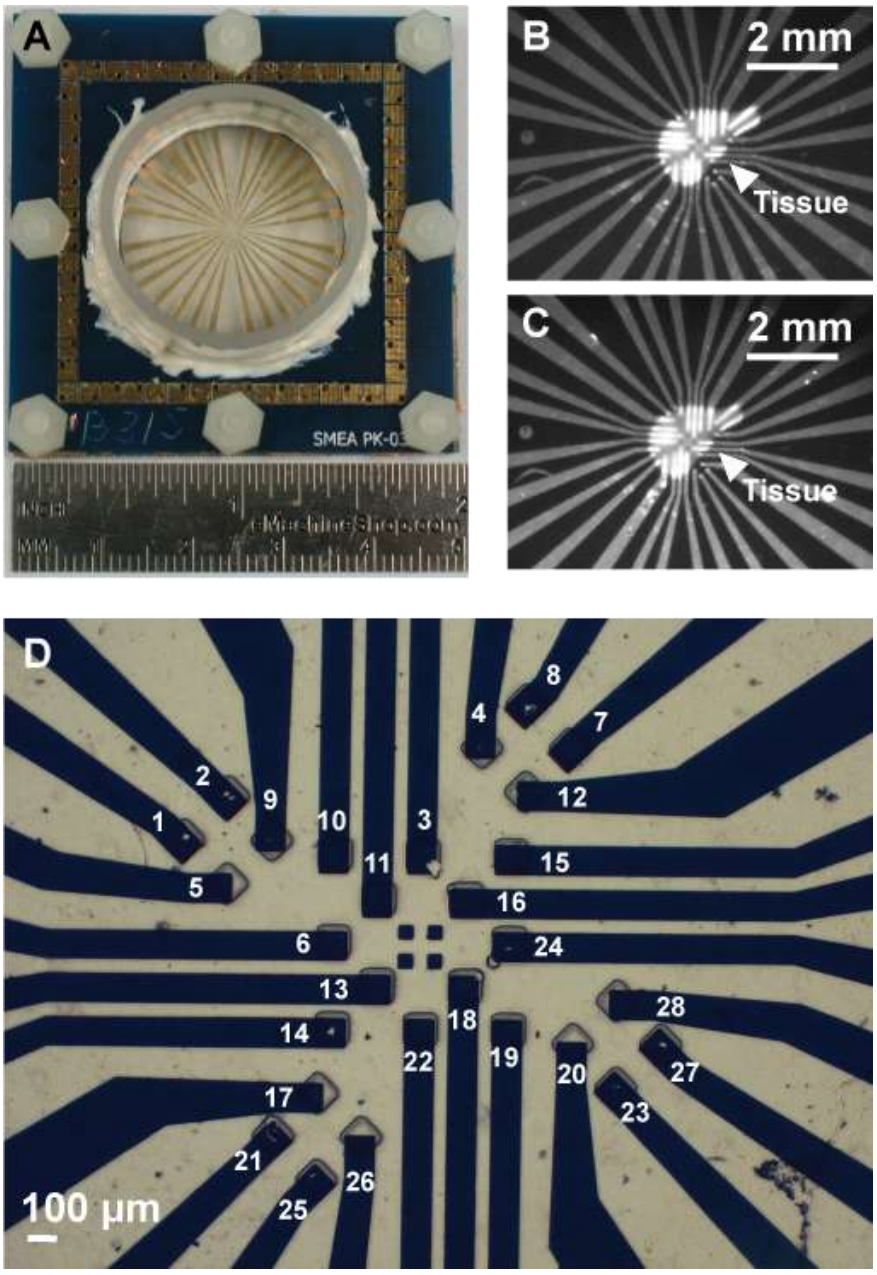

Figure 6.1 Images of an SMEA. (A) The SMEA featured 28 electrodes and 2 reference electrodes in a 49 mm x 49 mm package. (B) Image of a hippocampal slice culture on an SMEA before stretch injury. (C) Image of a hippocampal slice culture on an SMEA after stretch injury of approximately 0.2 strain and 2 s^{-1} strain rate. (D) Image of the 28-electrode array in the center of the SMEA. The tips of the patterned conductors were exposed through 100 µm x 100 µm vias photopatterned in the encapsulation layer. The

four small squares in the center are registration marks for aligning photolithographic masks. Individual electrode ID assignments are indicated in white.

6.2.2 Organotypic Slice Cultures of the Rat Hippocampus

All animal procedures were approved by the Columbia University Institutional Animal Care and Use Committee (IACUC). Prior to plating organotypic hippocampal slice cultures, SMEAs were made hydrophilic with air gas plasma treatment (Harrick PDC-32G, Harrick Scientific, Pleasantville, NY, USA) for 90 s (Egert and Meyer, 2005). SMEAs were pre-coated overnight with 80 μg/mL laminin (Life Technologies, Carlsbad, CA, USA) and 320 μg/mL poly-L-lysine (Sigma-Aldrich, St. Louis, MO, USA), and then incubated overnight with Neurobasal medium (Life Technologies; supplemented with 1 mM Glutamax, 50X B27, 4.5 mg/mL D-glucose, and 10 mM HEPES) in a standard cell-culture incubator (37°C, 5% CO_2). The brains of post-natal day 8-11 Sprague-Dawley rat pups were aseptically removed, and the hippocampus cut into 375 μm thick slices using a McIlwain tissue chopper (Harvard Apparatus, Holliston, MA, USA) according to published methods (Morrison *et al.*, 2006). Hippocampal slice cultures were then plated onto pre-coated SMEAs and fed every 2-3 days with conditioned full-serum medium (Sigma-Aldrich; 50% minimum essential media, 25% Hank's balanced salt solution, 25% heat inactivated horse serum, 1 mM Glutamax, 4.5 mg/mL D-glucose, and 10 mM HEPES) for 8-18 days total. To verify slice culture health prior to injury, the fluorescent dye propidium iodide (Life Technologies) was used to stain for dead or injured cells. Unhealthy slice cultures were not included in the study, according to published methods (Effgen *et al.*, 2012).

6.2.3 Mechanical Stretch Injury of Hippocampal Slice Cultures

The *in vitro* model of mechanical stretch injury has been characterized previously in detail (Morrison *et al.*, 2003, Morrison *et al.*, 2006). Briefly, after 8-18 days *in vitro*, media was removed from the SMEA well, and the hippocampal slice cultures were mechanically stretched by pulling the SMEA over a rigid, tubular indenter. Slice culture electrophysiological function was then assessed as described below. The induced tissue strain and strain rate were verified with high-speed video analysis of the dynamic stretch injury event. Lagrangian strain was determined by calculating the deformation gradient tensor by locating fiducial markers on the tissue slice image before and at maximal stretch (Morrison *et al.*, 2003).

6.2.4 Assessment of Electrophysiological Function

At the indicated time point after stretch injury and while still adhered to the SMEA, slice cultures were perfused with artificial cerebrospinal fluid (aCSF, Sigma-Aldrich; 125 mM NaCl, 3.5 mM KCl, 26 mM $NaHCO_3$, 1.2 mM KH_2PO_4, 1.3 mM $MgCl_2$, 2.4 mM $CaCl_2$, 10 mM D-glucose, pH = 7.4) at 37°C and aerated with 95% O_2/5% CO_2, as previously described (Yu and Morrison, 2010). For experiments involving GABA inhibition, slice cultures were perfused for a minimum of 3 minutes with bicuculline methiodide 50 μM (Sigma-Aldrich) in aCSF before recording electrical activity, within one hour post-injury. Bicuculline was then washed from the slice cultures for at least 20 minutes before returning them to the incubator for follow-up recordings at the indicated time points.

Spontaneous neural activity was measured by recording continuously for 3 minutes at a sampling rate of 20 kHz from all electrodes within the hippocampus prior to injury and at the

indicated time point. Raw data was low pass filtered with a 6 kHz analog, anti-aliasing filter and passed through a 60 Hz comb filter using a custom MATLAB script (version R2012a, MathWorks, Natick, MA, USA). Consistent with other MEA studies with acute slices, the electrodes of the SMEAs recorded the local field potentials produced by populations of neuronal cell bodies, dendrites, and axons within the local vicinity of individual electrodes (Novak and Wheeler, 1988). Neural event activity was detected based on the multiresolution Teager energy operator (m-TEO), which identifies epochs of data that contain high energy in specific frequency bands that are indicative of the feature being detected (Choi *et al.*, 2006). In this case, the feature was the local field potential of neuronal ensembles recorded by the planar electrodes of the SMEA. The m-TEO was calculated for k = (600, 900, 1200), and neural events were identified as the onset of those epochs with an m-TEO greater than 0.5 root-mean-square-error above the baseline m-TEO and with a raw signal greater than 1.5 root-mean-square-error above the baseline of the raw signal (Pimashkin *et al.*, 2011).

Using the results from the previous analysis above, which identified the onset time of each neural event on each electrode, the degree of correlation for event trains across electrode pairs was investigated. Spontaneous network synchronization was quantified using previously published methods based on correlation matrix analysis and surrogate resampling for significance testing (Li *et al.*, 2007a, Li *et al.*, 2010b, Patel *et al.*, 2012). Correlation of neural events was computed to determine an event synchronization measure, the synchronization index, for each electrode pair (Li *et al.*, 2007a). Correlated neural events across electrodes were defined as detected neural events that occurred within 1.5 ms of each other (Pimashkin *et al.*, 2011). For two electrodes *x* and *y*, and neural event-timing t_i^x and t_j^y (i = 1, …, m_x; j = 1, …, m_y), the event correlation matrix was calculated by:

$$c^{\tau}(x|y) = \sum_{i=1}^{m_x} \sum_{j=1}^{m_y} J_{ij}^{\tau} \begin{cases} J_{ij}^{\tau} = 1 \; if \; 0 < t_i^x - t_j^y \leq \tau \\ J_{ij}^{\tau} = \frac{1}{2} \; if \; t_i^x = t_j^y \\ J_{ij}^{\tau} = 0 \; otherwise \end{cases}$$

Equation 6.1 Neural event correlation matrix equation for spontaneous electrophysiology.

where τ was the time interval in which two events were considered synchronous (1.5 ms), mx and my were the total number of events to be compared, and J_{ij}^{τ} was a measure of correlation of two particular electrodes.

The event synchronization index for each electrode comparison, ranging in value from 0 (completely uncorrelated) to 1 (perfectly correlated), was calculated by:

$$Q_{\tau} = \frac{c^{\tau}(x|y) + c^{\tau}(y|x)}{\sqrt{m_x m_y}}$$

Equation 6.2 Neural event synchronization index equation for spontaneous electrophysiology.

To identify clusters of synchronized electrodes, first, the participation index (PI) was calculated for each electrode *a* that contributed to a cluster *b*:

$$PI_{ab} = \lambda_b v_{ab}^2$$

Equation 6.3 Participation index equation for spontaneous electrophysiology.

where v_{ab} was the a^{th} element of eigenvector v_b and λ_b was the corresponding eigenvalue of the event correlation matrix [$c^{\tau}(x|y)$]. PI_{ab} indicated the contribution of electrode *a* to the synchronized cluster *b*, with v_{ab}^2 defined as the weight with which electrode *a* contributed to cluster *b*. Clusters were defined as groups of electrodes with statistically similar patterns of activity, defined by PI ≥ 0.01 (Li *et al.*, 2010b).

Next, randomized surrogate time-series data without correlated electrode pairs were mathematically generated with an event rate equal to the instantaneous event rate of the experimental recordings by generating an inhomogeneous Poisson-distributed, 'event train.' These uncorrelated, synthetic 'event trains' were analyzed identically to the experimental data to produce a correlation matrix, eigenvalues, eigenvectors, and PI to bootstrap hypothesis testing of the experimental data (Li *et al.*, 2010b). Essentially, the uncorrelated Poisson-distributed 'event trains' served as the null hypothesis against which to test experimental data. The surrogate randomization was repeated 50 times, and the mean ($\bar{\lambda}'_k$) and standard deviation (SD_k) of surrogate eigenvalues were calculated (k = 1, …, M, where M was the number of electrodes). We identified the number of synchronized clusters that were significantly different from the randomized, asynchronous surrogates by:

$$Number\ of\ Clusters = \sum_k sgn\left[\lambda_k > \left(\bar{\lambda}'_k + K \times SD_k\right)\right]$$

Equation 6.4 Synchronized cluster equation.

where *sgn* was a sign function, λ_k was the eigenvalue of each electrode of the experimental data, and *K* was a constant (*K* = 3, for 99% confidence level, was used for this study). The detection of synchronized clusters represented the presence of neuronal assemblies functioning in an organized network. It is believed that neuron assemblies play a critical role in higher-order hippocampal function including spatial navigation and memory processes (Bahner *et al.*, 2011), which may be disrupted after TBI and axonal injury (Sharp *et al.*, 2014).

The degree of synchronization can be quantified and compared across slice cultures by calculating the global synchronization index (GSI), ranging from 0 (completely random, uncorrelated activity) to 1 (perfectly synchronous, correlated activity), for the cluster with the highest degree of synchronization within each slice culture:

$$GSI = \begin{cases} \dfrac{\lambda_M - \bar{\lambda}'}{M - \bar{\lambda}'} \; if \; \lambda_M > \bar{\lambda}' \\ 0 \; otherwise \end{cases}$$

Equation 6.5 Global synchronization index (GSI) equation.

where $\bar{\lambda}'$ was the mean of the highest eigenvalues calculated across all surrogates, λ_M was the maximal eigenvalue of the correlation matrix from the experimental data, and *M* was the number of electrodes. Lower synchronization (i.e. lower GSI) has been associated with dysfunctional or damaged neural networks (Tsirka *et al.*, 2011). Lastly, the GSI was apportioned to each region

(DG, CA3, CA1) based on the fraction of regional electrodes participating in the cluster to obtain a normalized GSI for each region.

6.2.5 Statistical Analysis

To account for variability in the density and excitability of neuronal populations at each electrode, spontaneous activity data was normalized to pre-injury levels for neural event rate on an electrode-by-electrode basis. Spontaneous activity and network synchronization data were analyzed by ANOVA, followed by Bonferroni *post hoc* tests with statistical significance set as $p < 0.05$.

6.3 Results

6.3.1 Mechanical Injury Alone Did Not Alter Spontaneous Network Activity

For all injured slice cultures, the average Lagrangian strain was 0.22 ± 0.02 and the average strain rate was 2.37 ± 0.39 s^{-1} (n = 12 slice cultures, mean ± SD), which constituted a mild to moderate injury as previously reported (Cater *et al.*, 2006, Elkin and Morrison, 2007, Yu and Morrison, 2010). Cell death was consistent with previously reported cell death in hippocampal slice cultures caused by mild to moderate injury (Cater *et al.*, 2006). Immediately post-injury and 24 hours after injury, no significant change in the normalized GSI was observed in any region (Figure 6.2A). In addition, no significant alterations in the normalized spontaneous event rate were observed in any region either acutely or 24 hours after injury (Figure 6.2B).

These results are consistent with the mild to moderate severity of the injury and the recording time point (Yu *et al.*, 2009a, Yu and Morrison, 2010).

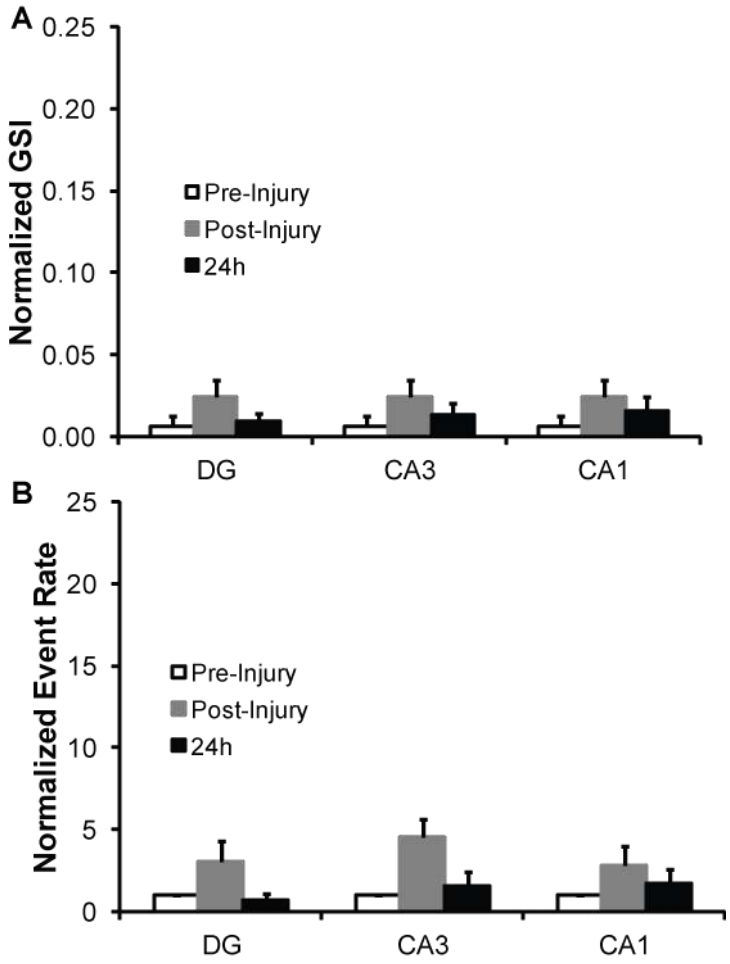

Figure 6.2 Neither network synchronization of spontaneous activity nor the normalized spontaneous event rate was significantly affected by injury. (A) Network synchronization, as measured by the normalized global synchronization index (GSI), was not significantly affected by injury either acutely or 24 hours after injury in DG, CA3, or CA1. (B) The normalized spontaneous event rate was not significantly altered by injury in DG, CA3, or CA1, either acutely after injury or 24 hours after injury. All data was normalized to pre-injury, pre-treatment levels (mean ± SEM).

6.3.2 Mechanical Injury Disrupted Bicuculline-induced, Long-lasting Network Synchronization

In both uninjured and injured slice cultures, bicuculline induced highly synchronized, correlated neural activity (Figure 6.3A, B).

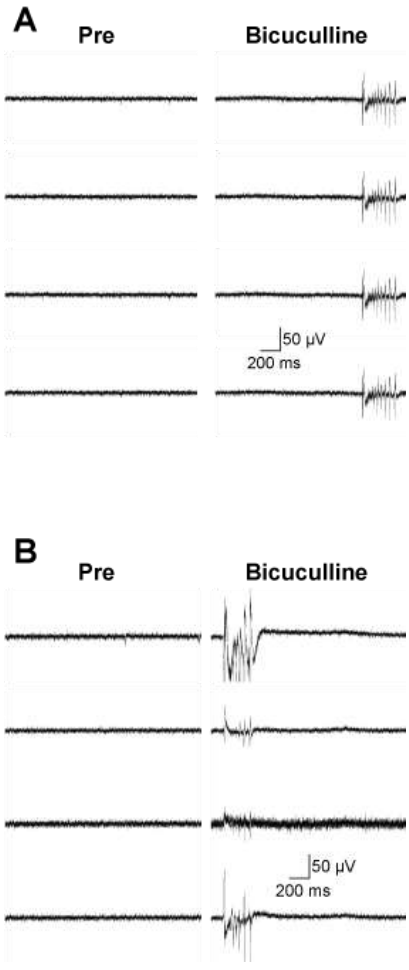

Figure 6.3 Representative traces of temporally aligned raw electrophysiology data from 4 electrodes in CA1 before bicuculline treatment and during bicuculline treatment from uninjured (A) and injured (B) slice cultures.

Prior to injury or bicuculline treatment, the hippocampal network was not synchronized as denoted by low (blue) correlation coefficients (Figure 6.4A, D). During bicuculline treatment, network synchronization increased in both uninjured and injured slice cultures (Figure 6.4B, E). 24 hours after bicuculline treatment, the hippocampal network remained highly synchronized in uninjured slice cultures (Figure 6.4C), whereas in injured cultures synchrony was significantly decreased (Figure 6.4F).

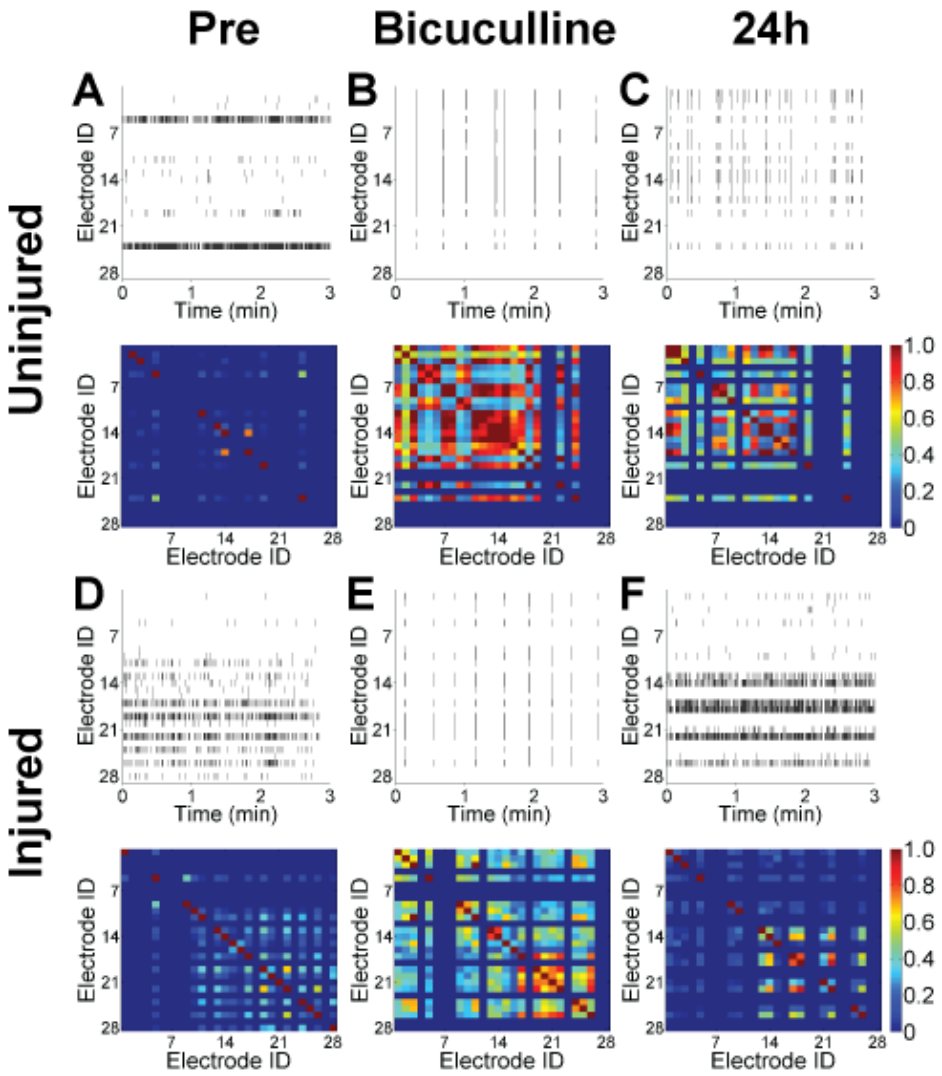

Figure 6.4 Changes in bicuculline-induced, long-lasting network synchronization of spontaneous activity in uninjured and injured slice cultures. Representative raster plots of spontaneous activity and heat maps of pair-wise synchronization $c^{\tau}(x|y)$ for every electrode pair are shown for uninjured and injured slice cultures at the indicated time points: before injury (or sham exposure) and before bicuculline treatment (A, D), during bicuculline treatment (B, E), and 24 hours after bicuculline treatment (C, F). Each line in the raster plots represent a distinct, identified neural event. Heat maps of pair-wise synchronization depict the event synchronization index for each electrode pair, ranging in value from 0 (completely uncorrelated, blue) to 1 (perfectly correlated, red).

Before injury or bicuculline treatment, the normalized GSI was very low in all regions of both uninjured and injured slice cultures (Figure 6.5, normalized GSI < 0.01). During bicuculline treatment, the normalized GSI significantly increased in all regions in both uninjured and injured cultures. 24 hours after bicuculline treatment, the normalized GSI was significantly higher in uninjured cultures compared to pre-bicuculline levels and compared to injured cultures. In contrast, in all regions of injured cultures, the normalized GSI was significantly decreased compared to during bicuculline treatment.

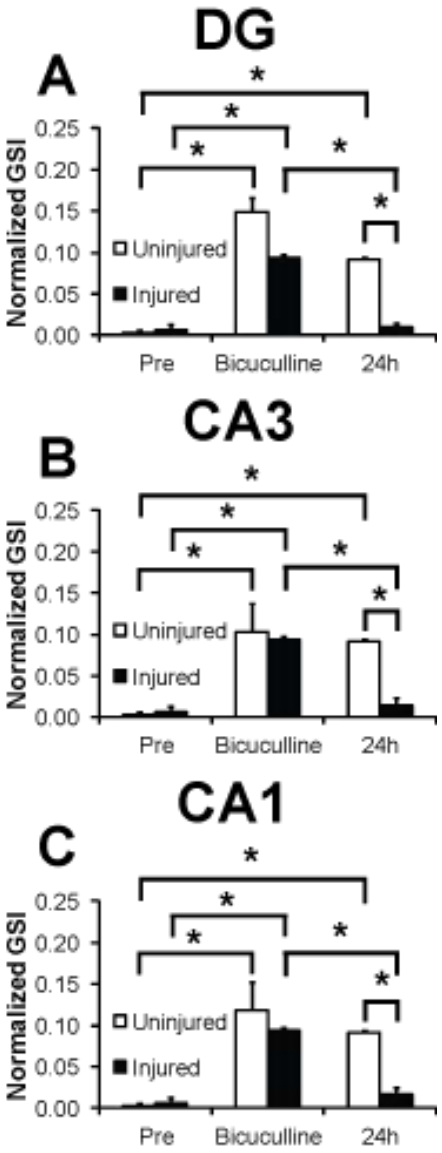

Figure 6.5 Changes in bicuculline-induced, long-lasting network synchronization of spontaneous activity in uninjured and injured slice cultures, quantified by the normalized GSI. Before injury (or sham exposure) and bicuculline treatment, network activity was not synchronized in any region (DG, CA3, or CA1), with the normalized GSI below 0.01 (A, B, C). Acutely during bicuculline exposure, the normalized GSI increased significantly in all hippocampal regions in both uninjured and injured slice cultures, compared to their respective baseline recordings, indicating significantly higher network synchronization. 24 hours after bicuculline exposure, the normalized GSI remained significantly higher in all hippocampal regions in uninjured slice cultures compared to pre-treatment baseline levels. In all

regions of injured slice cultures, the normalized GSI was significantly diminished 24 hours after bicuculline exposure when compared to the normalized GSI during bicuculline treatment, and when compared to uninjured slice cultures 24 hours after bicuculline treatment. Data is presented as mean ± SEM.

6.3.3 Mechanical Injury Increased the Rate of Bicuculline-induced Spontaneous Activity

In all regions of uninjured slice cultures, no significant alteration in the normalized spontaneous event rate was observed 24 hours after bicuculline exposure (Figure 6.6A, B, C). However, 24 hours after bicuculline exposure of injured slice cultures, the normalized spontaneous event rate was significantly increased in the DG and CA1 compared to pre-injury, pre-treatment levels, as well as when compared to uninjured cultures at the same time point (Figure 6.6A, C). No significant changes were observed in CA3 (Figure 6.6B). These results suggest that mild to moderate injury affected the ability of the surviving neuronal network to synchronize activity and not simply the ability of neurons to generate activity.

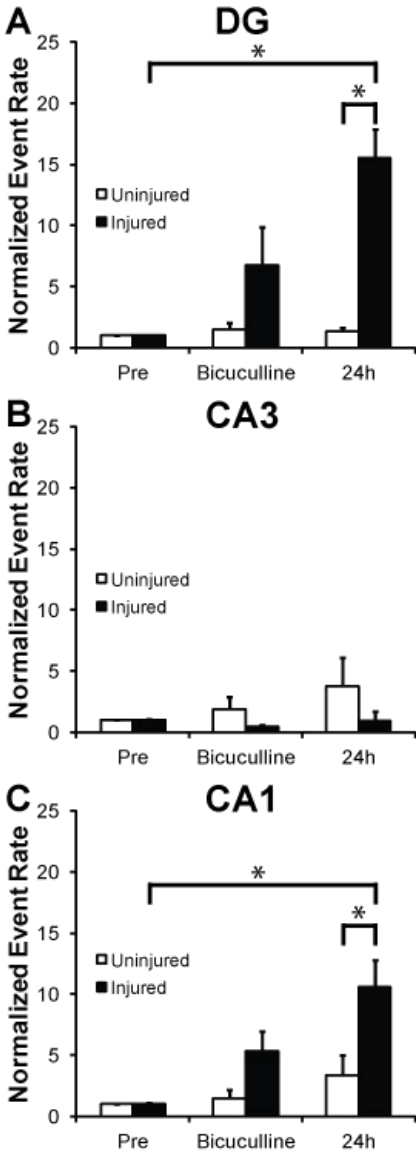

Figure 6.6 The normalized spontaneous event rate before and after bicuculline treatment in uninjured and injured slice cultures. 24 hours after bicuculline exposure, the normalized spontaneous event rate was significantly increased in injured DG (A) and CA1 (C) compared to pre-treatment, pre-injury baseline levels and compared to uninjured DG and CA1 at the same time point. No significant changes in the normalized spontaneous event rate were observed in CA3 (B). All data was normalized to pre-injury, pre-treatment levels (mean ± SEM).

6.3.4 Effects of Bicuculline Re-exposure Differed by Hippocampal Region

24 hours after the initial bicuculline treatment, injured slice cultures were exposed to bicuculline a second time to probe for potential mechanisms of the disruption in bicuculline-induced, long-lasting network synchronization. Re-exposure to bicuculline significantly increased the normalized GSI in all hippocampal regions compared to pre-injury, pre-treatment baseline levels and compared to 24 hours after the initial post-injury bicuculline exposure (Figure 6.7A). In contrast, the effect of re-exposure to bicuculline on event rate was region-dependent, significantly decreasing spontaneous activity in the DG but significantly increasing it in CA3 and CA1 (Figure 6.7B).

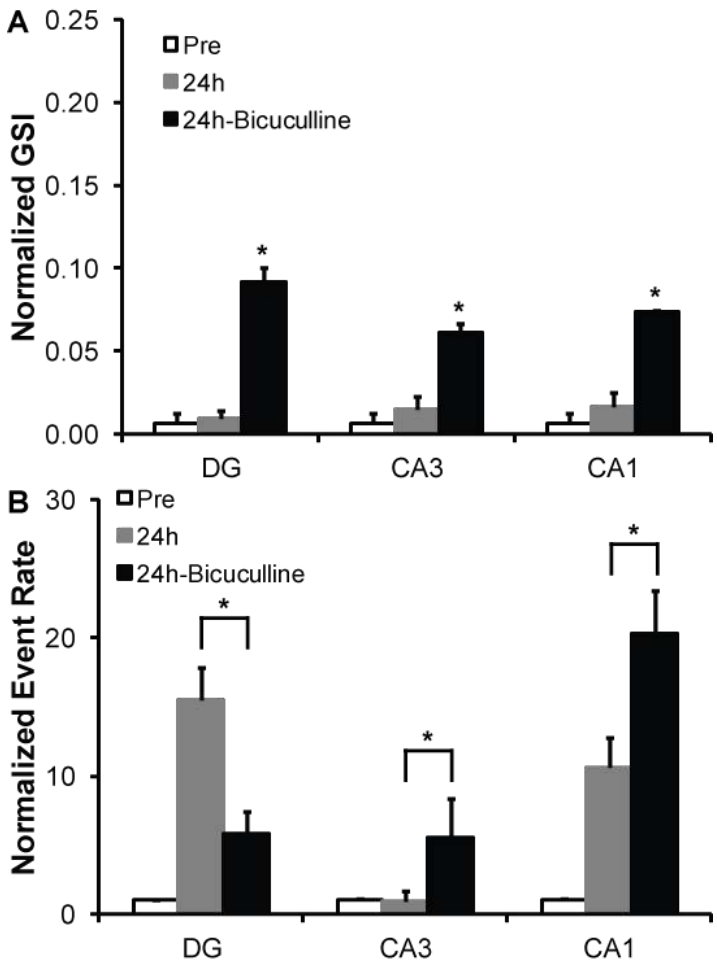

Figure 6.7 Changes in network synchronization of spontaneous activity and the normalized spontaneous event rate in injured slice cultures. (A) A second exposure to bicuculline 24 hours after the initial bicuculline exposure significantly increased the normalized GSI compared to pre-injury, pre-treatment baseline levels and compared to 24 hours after injury and the initial bicuculline exposure in DG, CA3, and CA1. The normalized GSI was not significantly different between hippocampal regions after the second bicuculline exposure. (B) A second exposure to bicuculline 24 hours after the initial bicuculline exposure produced different effects on the normalized spontaneous event rate depending on hippocampal region. Compared to 24h, re-exposure to bicuculline significantly decreased the normalized spontaneous event rate in DG, while significantly increasing the normalized spontaneous event rate in CA3 and CA1. All data was normalized to pre-injury, pre-treatment levels (mean ± SEM).

6.4 Discussion

In the present study, bicuculline exposure almost immediately transformed the network activity of both uninjured and injured hippocampal slice cultures from random, asynchronous activity to highly synchronized, correlated neural activity (Figure 6.3). In uninjured cultures, this coordinated activity persisted for at least 24 hours after the removal of bicuculline (Figure 6.4). In contrast, this long-lasting network synchronization was not evident in cultures that were mechanically injured (Figure 6.5A, B, C), despite increased network synchronization during bicuculline exposure and despite increased asynchronous activity 24h after bicuculline exposure (Figure 6.6A, B, C).

The injury severity for this study was chosen to be characteristic of mild to moderate TBI, which causes neuronal network dysfunction without appreciable cell death (Yu and Morrison, 2010). We observed that mechanical injury disrupted bicuculline-induced, long-lasting network synchronization, but did not abolish neuronal network activity (Figure 6.4, Figure 6.5, Figure 6.6). In fact, the normalized spontaneous event rate was higher in the DG and CA1 24 hours after injury (Figure 6.6A, C). Despite the hippocampal neuronal network being even more active after injury, it was unable to maintain synchronized, correlated activity, a deficit that could explain learning and memory impairments after TBI because the neural process underlying information storage in working memory is persistent neural activity (Wang, 2001). During memory encoding and recognition, optimally functional neuronal networks are highly organized and exhibit synchronization between interconnected neuronal regions (Stam *et al.*, 2007). Brain dysfunction after injury, such as mild TBI (Tsirka *et al.*, 2011), or as a result of

neurological disorders, such as Alzheimer's disease (Stam *et al.*, 2009), alters the functional structure of neuronal networks, transforming synchronized networks into less ordered and more random networks. In patients tested within days of suffering a mild TBI, global synchronization and network organization of rhythmic brain activity hypothesized to underlie episodic memory, was reduced, as measured by electroencephalography (EEG) recordings (Tsirka *et al.*, 2011). These patients also exhibited reduced performance in visual recognition tasks that were dependent on short-term episodic memory. It is an interesting observation that, in the current study, stretch disrupted the development of long-lasting network synchronization *in vitro,* as well (Tsirka *et al.*, 2011).

Exposing injured slice cultures to a second bicuculline challenge 24 hours after the initial exposure resulted in region-dependent changes in the normalized event rate (Figure 6.7). We speculate that the underlying mechanism behind this region-dependent observation may involve the interplay between the K-Cl co-transporter (KCC2) and the Na-K-2Cl co-transporter (NKCC1) in regulating the concentration of intracellular chloride. KCC2 has been implicated to play a key role in the impairment of GABAergic inhibition after mechanical injury (Bonislawski *et al.*, 2007). Bonislawski *et al*. observed significantly reduced KCC2 expression after TBI and a concomitant depolarized shift of the normally hyperpolarizing $GABA_A$ reversal potential in DG, but not CA1. Additionally, in a separate study, significant enhancement of spontaneous circuit activity in cultured hippocampal neurons was observed after pharmacological inhibition of KCC2 (Wang and Xu, 2006). With the depolarizing shift in the $GABA_A$ reversal potential due to post-injury alterations in KCC2 expression, GABA neurotransmission may become depolarizing/excitatory rather than hyperpolarizing/inhibitory, thereby increasing spontaneous activity after injury. In this case, inhibition of GABA by bicuculline would then be hypothesized

to decrease spontaneous activity, which may help explain our observations in the DG after injury (Figure 6.7). In general, however, chloride gradients shift by changing the expression of NKCC1 and KCC2 in the 2nd week of development in rodents (Leinekugel *et al.*, 1999). The hippocampal slice cultures used in our experiments were generated from P8-11 rat pups and were further cultured for an additional 18 days. Future experiments will be necessary to directly test whether changes in expression or activity of KCC2 and NKCC1 are responsible for these post-traumatic changes in network function. Quantifying the changes in NKCC1 and KCC2 protein expression before and after injury may uncover region-dependent roles of the chloride transporters within the hippocampus.

Significant progress has been made in improving the fabrication process of the SMEA and reducing the size of the recording contacts from 300 μm x 300 μm to 100 μm x 100 μm, nearly 90% smaller compared to earlier generations (Graudejus *et al.*, 2012). The reduced feature size has allowed for an increase in the number of recording electrodes from 11 to 28 (12 to 30 electrodes total, including reference electrodes) over the same surface area. However, a continuing limitation of the SMEA is the relatively large feature size of the recording electrodes compared to individual neurons. Commercially available rigid MEAs feature electrodes as small as 8 μm in diameter (256MEA30/8iR-ITO, Multichannel Systems). Currently, multiple neurons and neuronal ensembles may contribute to the summed signal measured from a single electrode. Smaller electrodes could potentially allow for stimulation and recording of individual neurons, increasing the spatial resolution of SMEA-based studies. Although the fabrication process remains difficult and expensive, efforts are underway to improve it and reduce overall manufacturing costs. In addition, *in vitro* slice cultures do not precisely recapitulate important factors of the *in vivo* extracellular environment, such as oxygenation and interplay with systemic

blood supply (Hyder *et al.*, 2007). Components of these systemic factors can be added to an *in vitro* slice culture model, but would require further characterization in order to limit any confounding effects.

7 Summary

7.1 Activated Astrocytes as a Therapeutic Target for TBI

Astrocytes become activated after CNS injury, undergoing a phenotypic change called reactive astrogliosis. One of the hallmarks of astrocyte activation is the increased production of extracellular GAG, which can act to inhibit neuronal regeneration and remyelination in the injured area (Zhang *et al.*, 2006, Properzi *et al.*, 2008, Wanner *et al.*, 2008). In Chapter 2, we took advantage of the relationship between increased GAG content and TAT transduction to deliver a therapeutic cargo to activated astrocytes to attenuate the negative consequences of the activation process.

Primary astrocyte cultures were mechanically stretched using a well-characterized *in vitro* model of TBI (Morrison *et al.*, 2003, Morrison *et al.*, 2006). The resulting overproduction of GAG and nitrite, a measurable oxidation product of NO, were quantified and compared to chemical stimulation known to induce astrocyte activation to verify that mechanical injury could induce astrocyte activation. Mechanical injury, the cytokine IL-1β (Kim *et al.*, 2006), and the *E.coli*-derived bacterial endotoxin LPS (Bhat *et al.*, 1998) all increased production of GAG and nitrite, with corresponding increases in GFP-TAT transduction.

The MAPK signaling pathways have been implicated in reactive astrogliosis and the subsequent cascade of detrimental effects associated with astrocyte activation (Otani *et al.*, 2002, Falsig *et al.*, 2004, Hsiao *et al.*, 2007). To verify the involvement of the MAPK signaling pathways in mechanical activation of astrocytes, we used small molecule inhibitors for p38, JNK, and ERK and reported significant inhibition of GAG, nitrite, and GFP-TAT transduction. A TAT-JNK inhibitor fusion protein was utilized after mechanical activation to specifically

target the JNK pathway, resulting in significant attenuation of activation, as measured by reduced GAG and nitrite levels.

The correlation between increased GAG levels and increased TAT transduction was utilized to specifically target only activated astrocytes after mechanical injury. To our knowledge, our study was the first to report significant attenuation of astrocyte activation through a JNK inhibitor fused to TAT after mechanical stretch injury. Our results suggest a potentially new, targeted therapeutic strategy utilizing TAT as a specific delivery vehicle to activated astrocytes.

Only recently have astrocytes emerged as playing essential roles in synaptic function, by releasing glutamate and other gliotransmitters (Panatier *et al.*, 2006, Henneberger *et al.*, 2010). Astrocytes activated by photostimulation were shown to control excitatory and inhibitory drive in the primary visual cortex (Perea *et al.*, 2014). However, very few studies exist that investigate changes in electrophysiological function after modulation of astrocyte activation. No studies exist in the literature correlating astrocyte activation to electrophysiological function specifically after TBI. This is a critical gap in TBI knowledge that could be addressed in future studies, as discussed below.

7.2 Functional Tolerance Criteria of the Hippocampus and Cortex to Mechanical Deformation

TBI can disrupt normal brain function, resulting in behavioral and functional consequences such as cognitive impairment (Arciniegas *et al.*, 2002, Skandsen *et al.*, 2010),

memory loss or impairment (Christodoulou *et al.*, 2001, Rodriguez Merzagora *et al.*, 2014), loss or decreased levels of consciousness (Godbolt *et al.*, 2013, Sorg *et al.*, 2014), motor deficits (Adelson *et al.*, 1997, Walker and Pickett, 2007), and seizure and epilepsy (Annegers *et al.*, 1998, Vespa *et al.*, 1999). These macroscopic changes in normal behavior and function are the result of cellular and molecular alterations that can be captured at the neuronal network level via electrophysiology (Ding *et al.*, 2011).

In Chapters 3 and 4, we quantified changes in electrophysiological function in response to precisely controlled mechanical stretch injuries in the hippocampus and cortex, respectively. Significant differences in electrophysiological function were observed between the two brain regions, consistent with previous work reporting differences in the cell death response to mechanical injury between the hippocampus and cortex (Cater *et al.*, 2006, Elkin and Morrison, 2007). However, a major difference between the mechanical injury-induced changes in cell death and electrophysiological function was how the outcome measures responded to similar combinations of tissue strain and strain rate. In the hippocampus, development of cell death was solely dependent on tissue strain but not strain rate, whereas in the cortex, both injury parameters significantly affected the development of cell death. Cell death also increased monotonically with increasing injury severity. In contrast, electrophysiological function in both regions generally depended on strain and strain rate in a complex, nonlinear manner. Our results highlight the importance of taking into account neuronal network function when investigating the biological consequences of TBI, possibly a more sensitive measure of injury than cell death.

Evidence suggests that the hippocampus may be more vulnerable to mechanical injury compared to the cortex (Elkin and Morrison, 2007), for various reasons such as differences in mechanical properties (Elkin *et al.*, 2010, Elkin *et al.*, 2011a, Elkin *et al.*, 2011b, Finan *et al.*,

2012), tissue architecture (LaPlaca *et al.*, 2005) and calcium channel density (Geddes *et al.*, 2003). In general, electrophysiological function in the hippocampus changed more drastically than electrophysiological function in the cortex in response to similar magnitudes of injury. For example, changes in strain and strain rate induced large changes in spontaneous event rate and duration in the hippocampus. In contrast, spontaneous event rate and duration did not change in response to tissue strain and strain rate in the cortex, staying constant regardless of the injury severity. Additionally, R_{max} fluctuated between 100 and 900 μV in the hippocampus, while R_{max} was restricted between 300 and 500 μV in the cortex. These results suggest that neurons in the hippocampus surviving stretch injury may be more susceptible to aberrant function than cortical neurons.

In Chapters 3 and 4, we quantified changes in electrophysiological function in response to mechanical stretch injury in the hippocampus and cortex using 60-channel MEAs. Data was recorded from each of the 60 channels simultaneously, essentially performing 60 discrete experiments at once. However, in Chapter 6, we were able to quantify the degree of synchronicity of the hippocampal neuronal network in hippocampal slices cultures on SMEAs. Utilizing the same analytical method from Chapter 6, we quantified network synchronization in the hippocampus after precisely controlled mechanical stretch injury.

The predicted values for the normalized GSI can be compared to the actual values of the normalized GSI quantified in Chapter 6 (Table 7.1). The predicted values for both pre-injury and injury (at 0.22 strain and 2.37 s^{-1} strain rate) are much higher than the actual values of the normalized GSI quantified in Chapter 6. One reason for the discrepancy in injured slice cultures is the difference in day post-injury between the two studies. In Chapter 3, spontaneous electrophysiological function was assessed four days post-injury, whereas in Chapter 6,

electrophysiological function was assessed acutely after injury and 24 hours post-injury. Cell death in the hippocampus progresses over time, with more cell death in all hippocampal regions four days after injury compared to one day after injury (Cater *et al.*, 2006). Although cell death and electrophysiological function are not always correlated, cell death can cause functional deficits, and it is likely that network synchronization may also change over time post-injury as a result. Differences in time post-injury significantly altered evoked field potentials in hippocampal slice cultures (Yu and Morrison, 2010), suggesting that the ability of the hippocampal neuronal network to function normally is disrupted in different ways depending on time post-injury. In a similar manner, network synchronization may also be disrupted differently, depending on time post-injury.

Region	Predicted Pre-Injury	Actual Pre-Injury	Predicted Injury	Actual Injury (Acute)	Actual Injury (24h)
Hippocampus DG	0.044 ±0.009	0.006 ±0.006	0.045 ±0.009	0.025 ±0.010	0.009 ±0.004
Hippocampus CA3	0.041 ±0.009	0.006 ±0.006	0.046 ±0.009	0.025 ±0.010	0.013 ±0.019
Hippocampus CA1	0.046 ±0.008	0.006 ±0.006	0.046 ±0.008	0.025 ±0.010	0.015 ±0.008

Table 7.1 Predicted and experimental values for the normalized GSI. Values are presented as mean ± SEM.

The normalized GSI was higher in uninjured cortex (0.87) compared to uninjured hippocampus (0.044 for DG, 0.041 for CA3, 0.046 for CA1), suggesting that the cortical

neuronal network is more synchronized than the hippocampal network. Cortical networks consist mostly of excitatory neurons (Lefort *et al.*, 2009), whereas inhibitory interneurons are important regulators of excitatory neurotransmission in the hippocampus (Gulyas *et al.*, 1999). Although network synchronization is generally attributed to the balance in excitatory and inhibitory signaling (Borgers and Kopell, 2003), cortical neurons, in particular, are able to form a highly synchronized network through primarily excitation (Acker *et al.*, 2003), despite the sparse tissue architecture of the cortex (Brunel, 2000). This difference in architecture may explain the higher network synchronization observed in the uninjured cortex compared to the uninjured hippocampus. In addition, the columnar organization of the cortex may contribute to the differences observed in network synchronization between the cortex and hippocampus. Neurons in different layers of the cortex exhibit layer-specific firing characteristics and activity patterns (Sun and Dan, 2009). Neurons in each cortical layer can form their own "small-world networks" with sparse long-range connections in between layers (Douglas *et al.*, 1995, Watts and Strogatz, 1998). In our studies, we did not segregate the cortical slice cultures into distinct areas. Differentiating the electrophysiological responses by cortical layer may elucidate the response of each cortical layer to mechanical injury, particularly in terms of network synchronization.

In Chapter 6, we quantified electrophysiological function in hippocampal slices cultured on SMEAs before and after mechanical stretch injury with average strain of 0.22 ± 0.02 and average strain rate of 2.37 ± 0.39. We compared the experimental results from Chapter 6 with predicted values for stimulus-response and spontaneous electrophysiological function using the predictive functions that were determined in Chapter 3 for the hippocampus (Table 7.2, Figure 7.1).

DG						CA3					CA1				
Parameter	Predicted Pre	Actual Pre	Predicted Injury	Actual Injury (Acute)	Actual Injury (24h post)	Predicted Pre	Actual Pre	Predicted Injury	Actual Injury (Acute)	Actual Injury (24h post)	Predicted Pre	Actual Pre	Predicted Injury	Actual Injury (Acute)	Actual Injury (24h post)
R_{max} (μV)	601 ±33	1080 ±101	593 ±181	829 ±114	1450 ±409	774 ±70	1176 ±113	665 ±70	792 ±158	1819 ±479	508 ±25	1177 ±94	515 ±25	842 ±111	884 ±147
I_{50} (μA)	26 ±2	26 ±1	38 ±3	33 ±2	19 ±1	26 ±2	25 ±1	38 ±3	36 ±3	21 ±1	26 ±2	23 ±1	38 ±3	31 ±1	21 ±1
M (μV/μA)	0.16 ±0.01	0.22 ±0.02	0.12 ±0.02	0.14 ±0.01	0.37 ±0.07	0.16 ±0.01	0.25 ±0.04	0.12 ±0.02	0.12 ±0.02	0.23 ±0.04	0.16 ±0.01	0.28 ±0.02	0.12 ±0.02	0.18 ±0.02	0.25 ±0.03
Event Rate (s^{-1})	0.08 ±0.01	0.12 ±0.02	0.10 ±0.01	0.31 ±0.07	0.06 ±0.02	0.08 ±0.01	0.10 ±0.06	0.10 ±0.01	0.61 ±0.17	0.21 ±0.12	0.08 ±0.01	0.08 ±0.03	0.10 ±0.01	0.16 ±0.05	0.12 ±0.05
Event Duration (s)	5.18 ±0.59	4.68 ±0.57	5.67 ±0.44	5.61 ±0.65	8.20 ±1.69	5.18 ±0.59	4.83 ±0.72	5.67 ±0.44	4.73 ±0.44	8.06 ±1.14	5.18 ±0.59	5.35 ±0.60	5.67 ±0.44	7.10 ±0.71	14.79 ±3.02
Event Magnitude (μV)	27 ±1	44 ±4	26 ±1	35 ±2	71 ±15	27 ±1	41 ±4	26 ±1	40 ±3	69 ±15	27 ±1	38 ±4	26 ±1	34 ±2	66 ±11

Table 7.2 Predicted and experimental values for stimulus-response and spontaneous electrophysiological function. Values are presented as mean ± SEM.

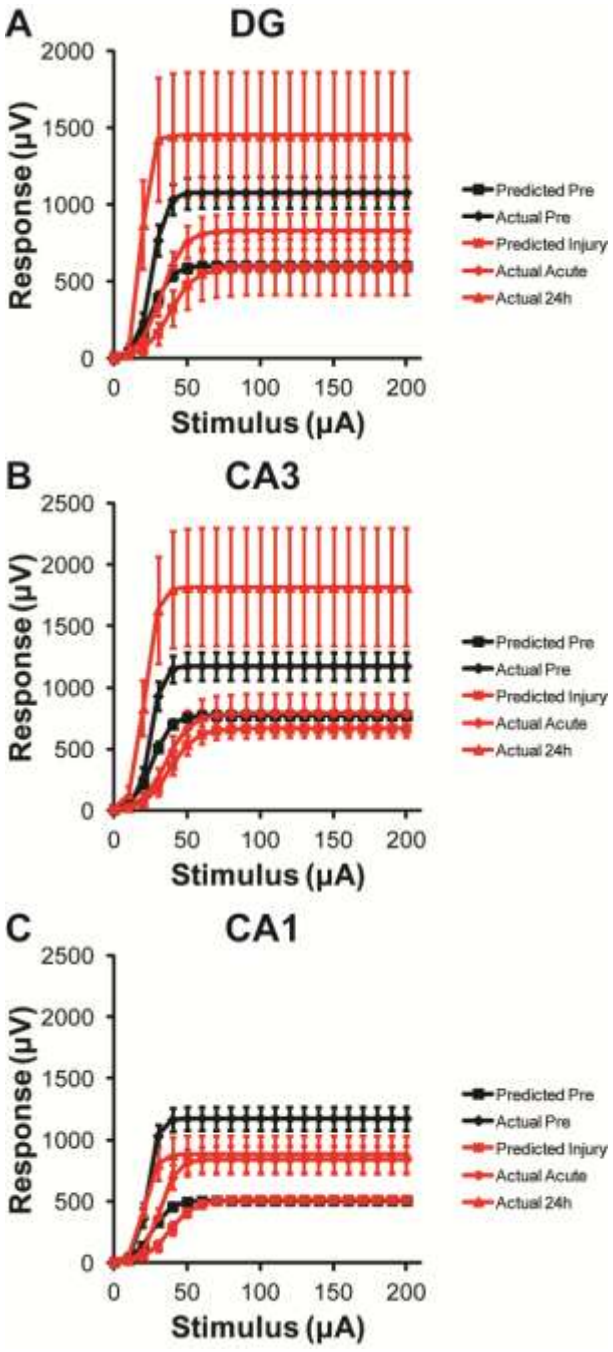

Figure 7.1 Comparison of S/R curves generated from experimental data from Chapter 6 and predictive functions from Chapter 3. Experimental data from hippocampal slices cultured on SMEAs (marked

'Actual') were compared to data from the predictive equations (marked 'Predicted') determined for the hippocampus in Chapter 2. Data is plotted for the uninjured, pre-injury state (black) and the injured state, at tissue strain of 0.22 and strain rate of 2.37 (red).

For S/R data, the predicted values of I_{50} were closest to the experimental values, particularly for the uninjured state, while predicted values of R_{max} were much lower than experimental values. For spontaneous data, predicted values of event rate and duration were close to experimental values, while predicted values of event magnitude were generally lower than experimental values. The discrepancies between the experimental and predicted values could be attributed to the differences in post-injury recording time points and the ages of the slice cultures. To determine the predictive equations in Chapter 3, electrophysiological function was assessed 4-6 days post-injury, whereas in Chapter 6, electrophysiological function was assessed acutely post-injury (within 20 min of injury) and 24 hours post-injury. The different time points post-injury resulted in different values for most electrophysiological parameters, particularly R_{max} and I_{50}, consistent with previous studies reporting a dependence on time post-injury for changes in evoked responses and paired-pulse responses (Yu and Morrison, 2010).

The different ages of the slice cultures led to different values of electrophysiological parameters at the pre-injury time points. In Chapter 3, pre-injury electrophysiological function was assessed as early as 14 days *in vitro*. In Chapter 6, pre-injury electrophysiological function was assessed sooner, as early as 8 days *in vitro*. The difference in age of the slice cultures led to different baseline levels for R_{max}, m and event duration, with all other electrophysiological parameters not significantly different between the experimental values and the predicted values. In previous studies, R_{max} and I_{50} significantly changed depending on the age of the slice cultures

(Yu and Morrison, 2010). The discrepancy between the experimental data and the predicted data in this example highlights the importance of controlling the experimental conditions of tissue culture and injury, to ensure consistency between experiments.

Quantification of biologically relevant functional changes in response to brain tissue deformation may increase our understanding of the mechanisms underlying the behavioral and functional consequences of TBI. In addition, our data sets could be incorporated into computational models of TBI to more accurately simulate the effects of tissue-level brain deformation during an injury event. Current FE models of TBI feature detailed predictions of the mechanical events that occur in various brain structures during TBI (Kleiven and Hardy, 2002, Takhounts *et al.*, 2008, Lamy *et al.*, 2011). Enhancing current FE models with the capability of predicting the functional and biological consequences of mechanical loading will enable the design and testing of more effective safety systems to prevent TBI. The ability to conduct *in silico* testing of prototypes of protective equipment and safety systems can greatly reduce the cost of prototype development, while increasing the rate of production (Moss *et al.*, 2014, Post *et al.*, 2014).

7.3 SMEAs as a Platform for TBI Research

Properly interfacing living brain tissue and electronic circuitry is a challenge that is being overcome by recent advances in stretchable electronics. Previous electrode array technologies were made of rigid materials such as glass, silicon, or metals that were up to 8 orders of magnitude stiffer than brain tissue. In contrast, moduli of SMEAs are only 4 orders of magnitude stiffer than neural tissues such as brain, spinal cord, and peripheral nerves.

Importantly for TBI research, SMEAs can also undergo large, rapid deformations relevant to TBI and maintain their conductive properties. The consequences of TBI are the result of brain tissue deformation, with tissue strain and strain rate identified as significant predictors of injury (Cater *et al.*, 2006, Elkin and Morrison, 2007). SMEAs must be able to deform with tissue to prevent additional mechanical damage as a result of the electrodes or SMEA substrate. In Chapter 5, we identified two major classes of SMEAs (planar and cuff) and reviewed the current state-of-the-art in SMEA technology, with critical assessments of the advantages and limitations associated with each of the classes and types. In Chapter 6, we discussed in detail a specific application of one particular SMEA design on investigating the mechanisms that may cause functional deficits post-TBI.

Using a more advanced generation of SMEAs compared to those that were characterized previously (Yu *et al.*, 2009a), we reported significant changes in hippocampal network synchronization after mechanical stretch injury. The SMEA allowed for quantification of spontaneous network function both before and after mechanical stretch injury and pharmacological treatment in the same culture. In addition, we measured spontaneous electrophysiological function without compromising slice culture sterility and while maintaining the relative position of the slice culture on the electrodes, thus enabling serial and long-term measurements over multiple hours and days within the same slice culture, and presumably, the same groups of neurons at each electrode. Our results highlight the utility of the SMEA as a platform for investigating the injury mechanisms that result in alterations in electrophysiological function. The SMEA could be used in studies of mechanotransduction after TBI as a platform for high-content drug screening, potentially increasing the rate of discovery of therapeutics for the treatment of TBI.

The SMEA could be utilized to test novel hypotheses regarding the underlying mechanisms that contributed to the post-injury changes in electrophysiological function described in this thesis. In Chapter 2, a TAT-conjugated peptide inhibitor of JNK was administered to a monoculture of primary astrocytes to modulate outcome measures of astrocyte activation. While the TAT-JNK inhibitor was successful in attenuating injury-induced astrocyte activation, the functional consequences of this therapeutic strategy are unknown. In future studies, primary astrocytes could be cultured directly on SMEAs and electrophysiological function could be assessed before and after injury, and before and after treatment with the TAT-JNK inhibitor. This experimental strategy would help determine the effect of modulating the JNK intracellular signaling pathway on the electrophysiological function of astrocytes. Although the outcome measures of astrocyte activation may be attenuated after TAT-JNK inhibitor treatment, it will be important to verify that normal astrocyte function is still intact, as astrocytes have essential roles in alleviating the negative effects of TBI. Additionally, the TAT-JNK inhibitor was only delivered to activated astrocytes in a monoculture of primary astrocytes. The next step in developing this potential therapeutic for TBI would be to test the effect of TAT-JNK inhibitor treatment on astrocyte activation and electrophysiological function in a mixed culture of neural cell types, such as cocultures of neurons and astrocytes, or even within organotypic slice cultures. The SMEA would be an ideal platform to test the functional consequences of TAT-JNK inhibitor treatment in injured cocultures or slice cultures.

In Chapter 3 and 4, we reported alterations in electrophysiological function in response to tissue strain and strain rate in the hippocampus and cortex, respectively. In general, electrophysiological function changed in a complex, nonlinear manner in response to injury parameters. The underlying mechanotransduction mechanisms of strain and strain rate to

changes in electrophysiological function remain unclear. One hypothesis is that the different types of neurons that contribute to the population-level electrophysiological function of the hippocampus and cortex could be susceptible to mechanical injury to different degrees, resulting in different effects on electrophysiological function depending on the magnitude of the mechanical stimuli. SMEAs could be used to help test this hypothesis by quantifying changes in electrophysiological function after stretch injury of monocultures of excitatory neurons versus interneurons. In this way, we could begin to clarify the contribution of each class of neurons to population-level electrophysiological responses after specific mechanical stimuli.

TBI also alters expression and function of neurotransmitter receptors, such as *N*-methyl-D-aspartate (NMDA) (Sihver *et al.*, 2001), AMPA (Schwarzbach *et al.*, 2006), and GABA (Reeves *et al.*, 1997) receptors. Within the hippocampal circuitry, in particular, synaptic transmission is regulated by the careful balance of excitatory and inhibitory neurotransmission. Modulation of any of these and other neurotransmitter receptors may result in alterations in population-level, electrophysiological function (Goforth *et al.*, 2004). It may be possible that certain neurotransmitter receptors may be more susceptible to strain and strain rate than others, which would lead to potentially complex consequences on the population-level, electrophysiological function. The SMEA could be utilized to help test this hypothesis by quantifying changes in electrophysiological function in hippocampal and cortical slice cultures after stretch injury and pharmacological blockade of various receptors. In this way, we could begin to quantify the specific contributions of neurotransmitters to population-level, electrophysiological function at different magnitudes of mechanical stretch injury.

7.4 Limitations

All of the studies in this thesis utilized *in vitro* approaches to approximate the effects of TBI in humans, whether it was through primary cell culture (Chapter 2) or organotypic brain slice culture (Chapter 3, 4, and 6). In Chapter 2, primary astrocytes were harvested from 8- to 10-day old Sprague-Dawley rat pups and were used to test the efficacy of delivering a TAT-conjugated JNK inhibitor to attenuate astrocyte activation. The validity of translating the results from an *in vitro* cell culture model derived from animals to humans is a limitation that could be overcome by a direct comparison of our results to human cells, either through primary culture from human brain tissue or established human cell lines (Allen *et al.*, 2005).

In Chapters 3 and 4, organotypic hippocampal and cortical slice cultures were generated from 8- to 11-day old Sprague-Dawley rat pups and were used to determine functional tolerance to tissue deformation. In Chapter 6, organotypic hippocampal slice cultures generated from 8- to 11-day old Sprague-Dawley rat pups were mechanically injured and the subsequent changes in spontaneous network activity were quantified using SMEAs. Again, a common limitation in these studies is whether the results can be translated to humans or are specific for the rat. For the functional tolerance studies, FE models also exist for TBI in the rat brain, which should be compatible with our data sets without any necessary scaling (Levchakov *et al.*, 2006, Lamy *et al.*, 2011, Lamy *et al.*, 2013). Additionally, findings from electrophysiology studies from small animal models are often translated to understanding electrophysiological function in human neural tissue (Cohen *et al.*, 2007, Reeves and Colley, 2012). . In addition, the cellular- and tissue-level changes after TBI in rat and human brains may not be significantly different, despite macroscopic differences in structure of the whole brain (Shreiber *et al.*, 1999). Therefore, since changes in electrophysiological function are the cumulative effect of changes in cellular and

molecular homeostasis, it may be possible to justify a comparison between the mechanotransduction of strain and strain rate into changes in electrophysiological function in our animal study and the human condition. The best way to address this limitation would be to conduct similar experiments on living cultures of human brain tissue.

In Chapter 2, a TAT-JNK inhibitor was delivered to astrocytes that were mechanically activated to attenuate the levels of GAG and nitrite, hallmarks of astrocyte activation. However, conclusive evidence is lacking whether this strategy would preferentially target only activated astrocytes over quiescent astrocytes as well. Mechanically injuring only a portion of a population of cultured astrocytes with modified injury devices (Miller *et al.*, 2009) and then quantifying the differences in immunofluorescence for GFAP and levels of GFP-TAT transduction between the injured and uninjured astrocyte subpopulations, would begin to test the specificity of the TAT-JNK inhibitor to activated astrocytes.

In addition, we have not shown conclusively that the TAT-JNK inhibitor would preferentially target activated astrocytes over other cell types in the brain, such as neurons and microglia. In the brains of patients suffering from Alzheimer's disease and other neurological disorders, increased levels of the intracellular GAG, heparan sulfate, were detected in neurons and, to a lesser extent, in microglia (Snow *et al.*, 1990, Su *et al.*, 1992). Following controlled cortical impact injury in mice, increased levels of the GAG, chondroitin sulfate, were detected in microglia and fibroblasts near the injury site (Yi *et al.*, 2012). Additionally, spinal cord injury increased expression of the GAG, keratan sulfate, by macrophages, microglia, and oligodendrocytes (Jones and Tuszynski, 2002). Experiments involving co-cultures of astrocytes and other neural cell types would help elucidate the extent of TAT-JNK inhibitor specificity to

activated astrocytes. Experiments with organotypic slice cultures would address this limitation as well.

Finally, the use of TAT-mediated drug therapeutics suffers from a practical limitation, in that TAT may not be capable of transcellular delivery across the blood-brain barrier (BBB) (Simon *et al.*, 2011). The BBB is a layer of specialized endothelial cells that separates the brain parenchyma from the vasculature and serves as a protective barrier against infectious pathogens. It is critical for any cell-penetrating peptide therapeutic to be able to cross the BBB without deleterious effect in order to preserve the beneficial, protective functions of the BBB. After TBI, the BBB breaks down locally around the site of injury, engendering the possibility of delivering TAT-mediated therapeutics specifically to the site of damage (Baskaya *et al.*, 1997). Experiments involving *in vivo* animal models of TBI will be necessary to investigate the effectiveness of TAT-mediated drug delivery. In addition, a targeted, noninvasive method of opening the BBB based on focused ultrasound and microbubbles has been developed, a potential workaround to the impermeability of the BBB to targeted therapeutics (Baseri *et al.*, 2012).

In Chapters 3 and 4, alterations in electrophysiological function in response to precisely controlled mechanical stimuli were reported in the hippocampus and cortex, respectively. Electrophysiological responses recorded from organotypic slice cultures by MEAs represent the summed population responses of a large number of neurons near each electrode. Both inhibitory and excitatory neurons contribute to a population response, with each type of neuron exhibiting different functional properties depending on the region of the brain (Csicsvari *et al.*, 1999, Hussar and Pasternak, 2012). In addition, network synchronization is dependent on the balance of inhibitory and excitatory neurons (Economo and White, 2012). Our results cannot capture the exact contributions of excitatory and inhibitory neurons to the population responses or the extent

to which the ratio of excitatory to inhibitory activity changes after injury. The organotypic slice culture model also contains all nerve and glial cell types found *in vivo* (Gahwiler *et al.*, 1997), with neurons and glia possessing differential susceptibility to mechanical injury (Zhao *et al.*, 2003). Therefore, it is difficult to conclude with certainty the exact mechanisms underlying the specific changes in electrophysiological function after mechanical injury. Additional studies regarding mechanotransduction mechanisms of changes in electrophysiological function are discussed below.

A further limitation to the functional tolerance studies in Chapters 3 and 4 is the somewhat limited range of strain and strain rate values used as inputs to determine the predictive function for each electrophysiological parameter. In Chapter 3, a maximum tissue strain of 0.44 and a maximum tissue strain rate of 30 s^{-1} were achieved in the hippocampus. In Chapter 4, we achieved maximum tissue strain of 0.59 and maximum tissue strain rate of 26 s^{-1} in the cortex. Although these values of strain and strain rate are relevant to mild and moderate TBI (Cater *et al.*, 2006, Elkin and Morrison, 2007), the strains and strain rates for more severe TBIs may surpass the upper bounds of our data set. For example, a combination of physical injury reconstruction and FE modeling of helmet-to-helmet collisions of NFL players reported that a collision with a 50% probability of concussion was predicted to produce strain of 0.26 and strain rate of 48.5 s^{-1} in gray matter (Kleiven, 2007). Other computational studies have implicated even higher brain strain and strain rate values in moderate to severe TBI (Kimpara and Iwamoto, 2012, Post *et al.*, 2012). Extrapolated predictions from our fit equations could potentially become less accurate in these cases. Our data set may be most appropriate for simulations of mild to moderate TBI that produce strain and strain rate values within or very near the upper bounds of our injury parameter data. In addition, future studies may require modifications to our

coating and slice culture procedure to better transfer the substrate strain to the cultured tissue to produce the high strains and strain rates relevant to severe TBI (see below).

In Chapter 6, we reported significant changes in spontaneous network activity 24 hours after mechanical stretch injury using SMEAs. A major advantage of the SMEA over traditional, rigid MEAs is the ability to conduct serial and long-term electrophysiological measurements over multiple hours and days within the same slice culture and the same groups of neurons at each electrode. However, we have not shown conclusive evidence that the electrodes are in the identical location before and after stretch injury. Image analysis of high-resolution, high-speed video of the injury event could confirm the adhesion of the slice culture to the SMEA throughout the injury event.

The SMEAs have some limitations when compared to traditional, rigid MEAs in terms of materials and dimensions. Despite improvements to fabrication techniques, the size of the recording electrodes is still 100 μm x 100 μm, larger than the smallest, current MEAs that feature electrodes as small as 10 μm in diameter (Borkholder *et al.*, 1997). SMEA electrodes are also relatively large compared to individual neurons. While patterning of smaller features has been demonstrated on PDMS and with the encapsulating PPS layer, adhesion between PPS and PDMS remains weak during the patterning process (Gao *et al.*, 2011). Improvements in interfacing the PPS layer and PDMS substrate of the SMEA will be necessary to reduce electrode feature size further to enable higher spatial resolution of future SMEA-based studies.

Another limitation of the SMEA is the lower number of recording electrodes in comparison to traditional MEAs. The larger electrode feature size of the SMEA constrains the number of electrodes that can reasonably interface with a brain slice culture simultaneously.

Currently, SMEAs feature 28 recording electrodes, substantially more than the 12 electrodes in a previous generation of SMEAs (Yu *et al.*, 2009a), but still less than commercially available rigid MEAs that feature between 60 and 256 electrodes (Charvet *et al.*, 2010).

Finally, we observed changes in spontaneous network activity after mechanical stretch injury of approximately 20% strain and 2 s^{-1}, values that are in the range of moderate TBI. However, strain and strain rate for more severe TBIs can exceed these values, and it remains an open question as to whether the SMEA can still function at very high biaxial strain and strain rate. Bare thin-film conductors have withstood uniaxial strains in excess of 60% (Lacour *et al.*, 2005). The previous generation of SMEAs was able to maintain conduction during 12% biaxial strain (Lacour *et al.*, 2006, Lacour and Adrega, 2010) and remained electrically conductive after uniaxial strain of up to 80% (Graudejus *et al.*, 2009). However, at this time, we have not investigated the upper bounds of biaxial strain that the current SMEA generation can withstand while still maintaining conduction.

7.5 Future Directions

In Chapter 2, inhibition of the JNK pathway was effective in decreasing astrocyte activation in mechanically injured astrocytes. However, it remains an open question whether decreasing astrocyte activation is completely beneficial for recovery from injury. Inhibiting the supporting role of activated astrocytes may worsen injury given their normal function in the brain. Selective ablation of reactive astrocytes after spinal cord injury in mice expressing a GFAP-herpes simplex virus-thymidine kinase transgene with ganciclovir was shown to result in widespread neurological damage (Faulkner *et al.*, 2004). The complete ablation of reactive

astrocytes after spinal cord injury resulted in failure of blood-brain barrier repair, leukocyte infiltration, local tissue disruption, severe demyelination, neuronal and oligodendrocyte death, and pronounce motor deficits. Ablation of reactive astrocytes after spinal cord injury resulted in more severe damage in all outcome measures of neurological damage than spinal cord injury alone. Our strategy of inhibiting the JNK pathway, however, could preserve homeostatic astrocytic processes by downregulating activated astrocytes rather than eliminating them altogether. To verify the beneficial effects of downregulating astrocyte activation, organotypic hippocampal slice cultures can be subjected to chemical and mechanical stimulation, and cell death and electrophysiological function can be assessed before and after TAT-JNK inhibitor treatment. The evolution of cell death and any changes in electrophysiological function could be used as indicators of the effect of the TAT-JNK inhibitor on the overall health and normal function of the slice culture. Additionally, *in vivo* experiments involving controlled cortical impact injury on mice could be used to directly probe for any behavioral or functional changes as a result of TAT-JNK inhibitor administration post-injury.

We confirmed the role of three different MAPK signaling pathways (p38, JNK, and ERK) in astrocyte activation, but chose to focus on the JNK pathway due to the commercial availability of a pre-conjugated TAT-JNK inhibitor at the time of writing. It would be beneficial to gain a more complete understanding of the role of MAPK on astrocyte activation by utilizing similar TAT-conjugated peptide inhibitors for p38 and ERK. A peptide inhibitor of ERK pre-conjugated to TAT is now commercially available (Monick *et al.*, 2006), while a peptide inhibitor of p38 conjugated to TAT has been designed, but is not yet available (Fu *et al.*, 2008). Each of these TAT-conjugated peptide inhibitors could be used separately and in combination to

identify an optimal therapeutic treatment for the negative consequences of astrocyte activation after TBI.

In Chapters 3 and 4, we identified changes in electrophysiological function after mechanical injury in the hippocampus and cortex, respectively. We reported that electrophysiological parameters associated with evoked responses (R_{max}, I_{50}, and m), paired-pulse responses (Short Term, Early-Mid, Late-Mid, and Long Term ISIs), and spontaneous activity (event rate, duration, and magnitude) all responded differently to applied tissue strains and strain rates. Unlike the development of cell death after stretch injury (Cater *et al.*, 2006, Elkin and Morrison, 2007), alterations in electrophysiological function were not monotonically dependent on strain or strain rate. The underlying mechanisms that govern these strain- and strain-rate- dependent changes in electrophysiological function remain unclear. One hypothesis is that the different types of neurons that contribute to the population-level electrophysiological activity in the hippocampus and cortex could be susceptible to mechanical injury to different degrees, resulting in different effects on electrophysiological function depending on the magnitude of the mechanical stimuli. SMEAs could be used to help test this hypothesis by quantifying changes in electrophysiological function after stretch injury of monocultures of excitatory neurons versus interneurons. In this way, we could begin to clarify the contribution of each class of neurons to population-level electrophysiological responses after specific mechanical stimuli.

As mentioned above, the upper bounds of strain and strain rate in our experimental data set limit the utility of the predictive functions that were determined in Chapters 3 and 4. While the data set that was used to determine the predictive functions covers the possible strain and strain rate that the brain experiences during mild and moderate TBI, it does not include the high

strain and strain rate values that are believed to be typical of severe TBIs. While our predictive functions allow for the extrapolation of changes in electrophysiological parameters at injuries of high strain and strain rate, caution should be exercised in interpreting these results if they exceed the maximal experimental values that comprise our data set. To ensure that our system of predictive functions covers the entire range of tissue deformation possible during TBI, it will be necessary to add high strain and strain rate injury data to our existing data set. The limiting factor in achieving these more severe injuries has been tissue culture adherence to the PDMS substrate. A combination of laminin and poly-L-lysine coating and Neurobasal incubation has proven effective for mild to moderate levels of strain and strain rate. However, we will need to improve and optimize the coating procedure to ensure slice cultures remain adhered to the PDMS membrane during high magnitude stretch injuries. Different coating solution formulations could be tested for improved slice culture adhesion, using polymers such as poly-D-lysine, poly-L-ornithine, PEI, gelatin, or any possible combination of these polymers.

The ultimate goal of the functional tolerance studies of Chapters 3 and 4 is to provide data, in the form of predictive functions, to FE models of TBI to improve their biofidelity and accuracy in terms of the functional consequences of TBI. However, we have only determined predictive functions for the hippocampus and cortex. FE models of TBI include other important structures of the brain, such as the cerebellum (Mao *et al.*, 2006), striatum (Lamy *et al.*, 2013), thalamus (Lamy *et al.*, 2011), corpus callosum (Patton *et al.*, 2012), and other white matter tracts (Pan *et al.*, 2013). Additionally for the cortex, FE models subdivide the largest structure of the brain based on the commonly classified lobes of the brain (Lamy *et al.*, 2011). It will be critical to characterize the functional response of as many major regions of the brain as possible because the spatial pattern of TBI-induced damage is not homogeneous (Lifshitz *et al.*, 2003, Levine *et*

al., 2006). The challenge lies in developing viable organotypic slice cultures of each brain region. To our knowledge, while organotypic hippocampal and cortical slice cultures are common in studies of TBI, very few slice culture preparations of other brain regions have been developed in models of TBI. While slice culture preparations of the cerebellum (Birgbauer *et al.*, 2004), striatum (Ostergaard *et al.*, 1995), thalamus (Yamada *et al.*, 2010), corpus callosum (Mi *et al.*, 2009), and white matter (Dean *et al.*, 2011) exist in the literature, they may not be compatible with our *in vitro* stretch injury device. Long-term survival and viability of each of these slice culture preparations would also need to be tested and confirmed.

The SMEA is a versatile tool that will allow the testing of novel mechanistic hypotheses regarding the functional consequences of TBI. An important component of understanding mechanisms of injury is the temporal development of changes in electrophysiological function, and concomitant cellular or molecular changes. The ability to monitor changes in electrophysiological function and other quantifiable outcome measures within the same slice culture over many hours and days offers a distinct advantage over studies using traditional rigid MEAs. For example, changes in protein expression of various $GABA_AR$ subunits are time-dependent after TBI (Gibson *et al.*, 2010), with alterations in normal $GABA_AR$ subunit activity known to induce changes in electrophysiological function (Bormann, 1988, Hollands *et al.*, 2009). SMEAs could be utilized to directly correlate TBI-induced changes in $GABA_AR$ subunit expression to electrophysiological function over multiple long-term time points. The rigid nature of most current MEAs would prevent direct testing of this, and many other, mechanisms of mechanotransduction. While we observed changes in spontaneous network activity over a 24 hour time period, longer duration studies could be performed, particularly in the clinically relevant 48 to 96 hour post-injury time window. The biggest hurdle to achieving longer term

studies remains the maintenance of culture sterility. The SMEAs are not autoclavable, so hydrogen peroxide treatment has been used as a surrogate for common sterilization techniques. Optimizing the cleaning and sterilization procedure will be critical to ensure successful long term studies using the SMEAs. Chemical sterilization with agents such as chlorine bleach could be effective, although bleach is highly corrosive and also is not completely effective against certain spores (Perez *et al.*, 2005). An alternative method of sterilization is radiation sterilization, such as ultraviolet light irradiation (UV). However, prolonged UV exposure may degrade PDMS crosslinks (Zheng *et al.*, 2013), limiting the number of re-use cycles of individual SMEAs.

In Chapter 6, we were able to quantify changes in electrophysiological function in slice cultures that were stretched at an average strain and strain rate of 0.22 and 2.37, respectively. The strains and strain rates associated with mild and moderate TBI can be captured using the SMEA. However, we have not tested the ability of the SMEA to function after very high biaxial strain and strain rate values that are appropriate for simulating severe TBI. It will be important to verify the ability of the SMEA to withstand and function after very high biaxial strain injuries.

8 References

Aare M, Kleiven S, Halldin P (2004) Injury tolerances for oblique impact helmet testing. Int J Crashworthines 9:15-23.

Abbott LF, Varela JA, Sen K, Nelson SB (1997) Synaptic depression and cortical gain control. Science 275:220-224.

Acker CD, Kopell N, White JA (2003) Synchronization of strongly coupled excitatory neurons: relating network behavior to biophysics. J Comput Neurosci 15:71-90.

Adelson PD, Dixon CE, Robichaud P, Kochanek PM (1997) Motor and cognitive functional deficits following diffuse traumatic brain injury in the immature rat. J Neurotrauma 14:99-108.

Ahn BY, Duoss EB, Motala MJ, Guo X, Park SI, Xiong Y, Yoon J, Nuzzo RG, Rogers JA, Lewis JA (2009) Omnidirectional printing of flexible, stretchable, and spanning silver microelectrodes. Science 323:1590-1593.

Akaike H (1973) Information theory and an extension of the maximum likelihood principle. Second International Symposium on Information Theory 267-281.

Allen DD, Caviedes R, Cardenas AM, Shimahara T, Segura-Aguilar J, Caviedes PA (2005) Cell lines as in vitro models for drug screening and toxicity studies. Drug Dev Ind Pharm 31:757-768.

Allen MP (1997) Understanding regression analysis. New York; London: Plenum Press.

Alloway KD, Johnson MJ, Wallace MB (1993) Thalamocortical interactions in the somatosensory system: interpretations of latency and cross-correlation analyses. J Neurophysiol 70:892-908.

Aloisi F, Care A, Borsellino G, Gallo P, Rosa S, Bassani A, Cabibbo A, Testa U, Levi G, Peschle C (1992) Production of hemolymphopoietic cytokines (IL-6, IL-8, colony-stimulating factors) by normal human astrocytes in response to IL-1 beta and tumor necrosis factor-alpha. J Immunol 149:2358-2366.

Annegers JF, Hauser WA, Coan SP, Rocca WA (1998) A population-based study of seizures after traumatic brain injuries. N Engl J Med 338:20-24.

Arbogast KB, Margulies SS (1998) Material characterization of the brainstem from oscillatory shear tests. J Biomech 31:801-807.

Arciniegas DB, Held K, Wagner P (2002) Cognitive impairment following traumatic brain injury. Curr Treat Options Neurol 4:43-57.

Arlot S, Celisse A (2010) A survey of cross-validation procedures for model selection. Statis Surv 4:40-79.

Armstrong-James M, Fox K, Das-Gupta A (1992) Flow of excitation within rat barrel cortex on striking a single vibrissa. J Neurophysiol 68:1345-1358.

Arnold FJ, Hofmann F, Bengtson CP, Wittmann M, Vanhoutte P, Bading H (2005) Microelectrode array recordings of cultured hippocampal networks reveal a simple model for transcription and protein synthesis-dependent plasticity. J Physiol 564:3-19.

Asikainen I, Kaste M, Sarna S (1999) Early and late posttraumatic seizures in traumatic brain injury rehabilitation patients: brain injury factors causing late seizures and influence of seizures on long-term outcome. Epilepsia 40:584-589.

Atkins CM, Falo MC, Alonso OF, Bramlett HM, Dietrich WD (2009) Deficits in ERK and CREB activation in the hippocampus after traumatic brain injury. Neurosci Lett 459:52-56.

Atkins CM, Oliva AA, Jr., Alonso OF, Chen S, Bramlett HM, Hu BR, Dietrich WD (2007a) Hypothermia treatment potentiates ERK1/2 activation after traumatic brain injury. Eur J Neurosci 26:810-819.

Atkins CM, Oliva AA, Jr., Alonso OF, Pearse DD, Bramlett HM, Dietrich WD (2007b) Modulation of the cAMP signaling pathway after traumatic brain injury. Exp Neurol 208:145-158.

Audouy S, Mallet J, Privat A, Gimenez y Ribotta M (1999) Adenovirus-mediated suicide gene therapy in an in vitro model of reactive gliosis. Glia 25:293-303.

Bahner F, Weiss EK, Birke G, Maier N, Schmitz D, Rudolph U, Frotscher M, Traub RD, Both M, Draguhn A (2011) Cellular correlate of assembly formation in oscillating hippocampal networks in vitro. Proc Natl Acad Sci U S A 108:E607-616.

Bain AC, Meaney DF (2000) Tissue-level thresholds for axonal damage in an experimental model of central nervous system white matter injury. J Biomech Eng 122:615-622.

Barreto GE, Sun X, Xu L, Giffard RG (2011) Astrocyte proliferation following stroke in the mouse depends on distance from the infarct. PLoS One 6:e27881.

Baseri B, Choi JJ, Deffieux T, Samiotaki G, Tung YS, Olumolade O, Small SA, Morrison B, Konofagou EE (2012) Activation of signaling pathways following localized delivery of systemically administered neurotrophic factors across the blood-brain barrier using focused ultrasound and microbubbles. Phys Med Biol 57:N65-81.

Baskaya MK, Rao AM, Dogan A, Donaldson D, Dempsey RJ (1997) The biphasic opening of the blood-brain barrier in the cortex and hippocampus after traumatic brain injury in rats. Neurosci Lett 226:33-36.

Bayly PV, Black EE, Pedersen RC, Leister EP, Genin GM (2006) In vivo imaging of rapid deformation and strain in an animal model of traumatic brain injury. J Biomech 39:1086-1095.

Bayly PV, Cohen TS, Leister EP, Ajo D, Leuthardt EC, Genin GM (2005) Deformation of the human brain induced by mild acceleration. J Neurotrauma 22:845-856.

Beggs JM, Plenz D (2004) Neuronal avalanches are diverse and precise activity patterns that are stable for many hours in cortical slice cultures. J Neurosci 24:5216-5229.

Bennett BL, Sasaki DT, Murray BW, O'Leary EC, Sakata ST, Xu W, Leisten JC, Motiwala A, Pierce S, Satoh Y, Bhagwat SS, Manning AM, Anderson DW (2001) SP600125, an anthrapyrazolone inhibitor of Jun N-terminal kinase. Proc Natl Acad Sci U S A 98:13681-13686.

Bhat NR, Zhang P, Lee JC, Hogan EL (1998) Extracellular signal-regulated kinase and p38 subgroups of mitogen-activated protein kinases regulate inducible nitric oxide synthase and tumor necrosis factor-alpha gene expression in endotoxin-stimulated primary glial cultures. J Neurosci 18:1633-1641.

Bilston LE, Thibault LE (1996) The mechanical properties of the human cervical spinal cord in vitro. Ann Biomed Eng 24:67-74.

Biran R, Martin DC, Tresco PA (2005) Neuronal cell loss accompanies the brain tissue response to chronically implanted silicon microelectrode arrays. Exp Neurol 195:115-126.

Biran R, Martin DC, Tresco PA (2007) The brain tissue response to implanted silicon microelectrode arrays is increased when the device is tethered to the skull. J Biomed Mater Res A 82:169-178.

Birgbauer E, Rao TS, Webb M (2004) Lysolecithin induces demyelination in vitro in a cerebellar slice culture system. J Neurosci Res 78:157-166.

Blue ME, Parnavelas JG (1983a) The formation and maturation of synapses in the visual cortex of the rat. I. Qualitative analysis. J Neurocytol 12:599-616.

Blue ME, Parnavelas JG (1983b) The formation and maturation of synapses in the visual cortex of the rat. II. Quantitative analysis. J Neurocytol 12:697-712.

Bonislawski DP, Schwarzbach EP, Cohen AS (2007) Brain injury impairs dentate gyrus inhibitory efficacy. Neurobiol Dis 25:163-169.

Bonny C, Oberson A, Negri S, Sauser C, Schorderet DF (2001) Cell-permeable peptide inhibitors of JNK: novel blockers of beta-cell death. Diabetes 50:77-82.

Borgers C, Kopell N (2003) Synchronization in networks of excitatory and inhibitory neurons with sparse, random connectivity. Neural Comput 15:509-538.

Borkholder DA, Bao J, Maluf NI, Perl ER, Kovacs GT (1997) Microelectrode arrays for stimulation of neural slice preparations. J Neurosci Methods 77:61-66.

Bormann J (1988) Electrophysiology of GABAA and GABAB receptor subtypes. Trends Neurosci 11:112-116.

Borschel GH, Kia KF, Kuzon WM, Jr., Dennis RG (2003) Mechanical properties of acellular peripheral nerve. J Surg Res 114:133-139.

Borsello T, Clarke PG, Hirt L, Vercelli A, Repici M, Schorderet DF, Bogousslavsky J, Bonny C (2003) A peptide inhibitor of c-Jun N-terminal kinase protects against excitotoxicity and cerebral ischemia. Nat Med 9:1180-1186.

Bradbury EJ, Moon LD, Popat RJ, King VR, Bennett GS, Patel PN, Fawcett JW, McMahon SB (2002) Chondroitinase ABC promotes functional recovery after spinal cord injury. Nature 416:636-640.

Brooks H, Lebleu B, Vives E (2005) Tat peptide-mediated cellular delivery: back to basics. Adv Drug Deliv Rev 57:559-577.

Browne KD, Chen XH, Meaney DF, Smith DH (2011) Mild traumatic brain injury and diffuse axonal injury in swine. J Neurotrauma 28:1747-1755.

Brunel N (2000) Dynamics of sparsely connected networks of excitatory and inhibitory spiking neurons. J Comput Neurosci 8:183-208.

Buchs PA, Stoppini L, Muller D (1993) Structural modifications associated with synaptic development in area CA1 of rat hippocampal organotypic cultures. Brain Res Dev Brain Res 71:81-91.

Burnham KP, Anderson DR (2002) Model selection and multimodel inference : a practical information-theoretic approach. New York: Springer.

Burnham KP, Anderson DR (2004) Multimodel inference - understanding AIC and BIC in model selection. Sociol Method Res 33:261-304.

Buzsaki G (1989) Two-stage model of memory trace formation: a role for "noisy" brain states. Neuroscience 31:551-570.

Cao WZ, Gorrn P, Wagner S (2011) Modeling the electrical resistance of gold film conductors on uniaxially stretched elastomeric substrates. Appl Phys Lett 98.

Carmena JM, Lebedev MA, Henriquez CS, Nicolelis MA (2005) Stable ensemble performance with single-neuron variability during reaching movements in primates. J Neurosci 25:10712-10716.

Cater HL, Gitterman D, Davis SM, Benham CD, Morrison B, 3rd, Sundstrom LE (2007) Stretch-induced injury in organotypic hippocampal slice cultures reproduces in vivo post-

traumatic neurodegeneration: role of glutamate receptors and voltage-dependent calcium channels. J Neurochem 101:434-447.

Cater HL, Sundstrom LE, Morrison B, 3rd (2006) Temporal development of hippocampal cell death is dependent on tissue strain but not strain rate. J Biomech 39:2810-2818.

Cawley GC, Talbot NLC (2010) On over-fitting in model selection and subsequent selection bias in performance evaluation. J Mach Learn Res 11:2079-2107.

Charvet G, Rousseau L, Billoint O, Gharbi S, Rostaing JP, Joucla S, Trevisiol M, Bourgerette A, Chauvet P, Moulin C, Goy F, Mercier B, Colin M, Spirkovitch S, Fanet H, Meyrand P, Guillemaud R, Yvert B (2010) BioMEA: a versatile high-density 3D microelectrode array system using integrated electronics. Biosens Bioelectron 25:1889-1896.

Chen CS, Gray DS, Tien J (2004) High-conductivity elastomeric electronics. Adv Mater 16:393-397.

Chen J, Thorpe MF, Davis LC (1995) Elastic properties of rigid fiber-reinforced composites. J Appl Phys 77:4349-4360.

Cheung KC (2007) Implantable microscale neural interfaces. Biomed Microdevices 9:923-938.

Cheung KC, Renaud P, Tanila H, Djupsund K (2007) Flexible polyimide microelectrode array for in vivo recordings and current source density analysis. Biosens Bioelectron 22:1783-1790.

Chiu SL, Leu J, Ho PS (1994) Fracture of metal-polymer line structures. 1. semiflexible polyimide. J Appl Phys 76:5136-5142.

Choi JH, Jung HK, Kim T (2006) A new action potential detector using the MTEO and its effects on spike sorting systems at low signal-to-noise ratios. IEEE Trans Biomed Eng 53:738-746.

Choo AM, Miller WJ, Chen YC, Nibley P, Patel TP, Goletiani C, Morrison B, 3rd, Kutzing MK, Firestein BL, Sul JY, Haydon PG, Meaney DF (2013) Antagonism of purinergic signalling improves recovery from traumatic brain injury. Brain 136:65-80.

Christidi F, Bigler ED, McCauley SR, Schnelle KP, Merkley TL, Mors MB, Li X, Macleod M, Chu Z, Hunter JV, Levin HS, Clifton GL, Wilde EA (2011) Diffusion tensor imaging of the perforant pathway zone and its relation to memory function in patients with severe traumatic brain injury. J Neurotrauma 28:711-725.

Christodoulou C, DeLuca J, Ricker JH, Madigan NK, Bly BM, Lange G, Kalnin AJ, Liu WC, Steffener J, Diamond BJ, Ni AC (2001) Functional magnetic resonance imaging of working memory impairment after traumatic brain injury. J Neurol Neurosurg Psychiatry 71:161-168.

Chung IY, Benveniste EN (1990) Tumor necrosis factor-alpha production by astrocytes. Induction by lipopolysaccharide, IFN-gamma, and IL-1 beta. J Immunol 144:2999-3007.

Clark RS, Kochanek PM, Watkins SC, Chen M, Dixon CE, Seidberg NA, Melick J, Loeffert JE, Nathaniel PD, Jin KL, Graham SH (2000) Caspase-3 mediated neuronal death after traumatic brain injury in rats. J Neurochem 74:740-753.

Coats B, Eucker SA, Sullivan S, Margulies SS (2012) Finite element model predictions of intracranial hemorrhage from non-impact, rapid head rotations in the piglet. Int J Dev Neurosci 30:191-200.

Cohen AS, Pfister BJ, Schwarzbach E, Grady MS, Goforth PB, Satin LS (2007) Injury-induced alterations in CNS electrophysiology. Prog Brain Res 161:143-169.

Cohen D, Nicolelis MA (2004) Reduction of single-neuron firing uncertainty by cortical ensembles during motor skill learning. J Neurosci 24:3574-3582.

Cole-Edwards KK, Musto AE, Bazan NG (2006) c-Jun N-terminal kinase activation responses induced by hippocampal kindling are mediated by reactive astrocytes. J Neurosci 26:8295-8304.

Colgan NC, Gilchrist MD, Curran KM (2010) Applying DTI white matter orientations to finite element head models to examine diffuse TBI under high rotational accelerations. Prog Biophys Mol Biol 103:304-309.

Commins S, Gigg J, Anderson M, O'Mara SM (1998) Interaction between paired-pulse facilitation and long-term potentiation in the projection from hippocampal area CA1 to the subiculum. Neuroreport 9:4109-4113.

Crown ED, Ye Z, Johnson KM, Xu GY, McAdoo DJ, Hulsebosch CE (2006) Increases in the activated forms of ERK 1/2, p38 MAPK, and CREB are correlated with the expression of at-level mechanical allodynia following spinal cord injury. Exp Neurol 199:397-407.

Csicsvari J, Hirase H, Czurko A, Mamiya A, Buzsaki G (1999) Oscillatory coupling of hippocampal pyramidal cells and interneurons in the behaving rat. J Neurosci 19:274-287.

Cullen DK, Simon CM, LaPlaca MC (2007) Strain rate-dependent induction of reactive astrogliosis and cell death in three-dimensional neuronal-astrocytic co-cultures. Brain Res 1158:103-115.

D'Ambrosio R, Maris DO, Grady MS, Winn HR, Janigro D (1998) Selective loss of hippocampal long-term potentiation, but not depression, following fluid percussion injury. Brain Res 786:64-79.

Dalva MB, Katz LC (1994) Rearrangements of synaptic connections in visual cortex revealed by laser photostimulation. Science 265:255-258.

Darvish KK, Crandall JR (2001) Nonlinear viscoelastic effects in oscillatory shear deformation of brain tissue. Med Eng Phys 23:633-645.

Dash PK, Johnson D, Clark J, Orsi SA, Zhang M, Zhao J, Grill RJ, Moore AN, Pati S (2011) Involvement of the glycogen synthase kinase-3 signaling pathway in TBI pathology and neurocognitive outcome. PLoS One 6:e24648.

Dash PK, Mach SA, Moore AN (2002) The role of extracellular signal-regulated kinase in cognitive and motor deficits following experimental traumatic brain injury. Neuroscience 114:755-767.

De Curtis M, Biella G, Forti M, Panzica F (1994) Multifocal spontaneous epileptic activity induced by restricted bicuculline ejection in the piriform cortex of the isolated guinea pig brain. J Neurophysiol 71:2463-2476.

de Laszlo SE, Visco D, Agarwal L, Chang L, Chin J, Croft G, Forsyth A, Fletcher D, Frantz B, Hacker C, Hanlon W, Harper C, Kostura M, Li B, Luell S, MacCoss M, Mantlo N, O'Neill EA, Orevillo C, Pang M, Parsons J, Rolando A, Sahly Y, Sidler K, O'Keefe SJ, et al. (1998) Pyrroles and other heterocycles as inhibitors of p38 kinase. Bioorg Med Chem Lett 8:2689-2694.

Deadwyler SA, Hampson RE (1995) Ensemble activity and behavior: what's the code? Science 270:1316-1318.

Dean JM, Riddle A, Maire J, Hansen KD, Preston M, Barnes AP, Sherman LS, Back SA (2011) An organotypic slice culture model of chronic white matter injury with maturation arrest of oligodendrocyte progenitors. Mol Neurodegener 6:46.

Devanne H, Lavoie BA, Capaday C (1997) Input-output properties and gain changes in the human corticospinal pathway. Exp Brain Res 114:329-338.

DeWeerth SP, Guo LA (2010) High-density stretchable electronics: toward an integrated multilayer composite. Adv Mater 22:4030-4033.

Ding MC, Wang Q, Lo EH, Stanley GB (2011) Cortical excitation and inhibition following focal traumatic brain injury. J Neurosci 31:14085-14094.

Diogo AC, Soares JG, Koulakov A, Albright TD, Gattass R (2003) Electrophysiological imaging of functional architecture in the cortical middle temporal visual area of Cebus apella monkey. J Neurosci 23:3881-3898.

DiScenna PG, Teyler TJ (1994) Development of inhibitory and excitatory synaptic transmission in the rat dentate gyrus. Hippocampus 4:569-576.

Dobbing J, Sands J (1979) Comparative aspects of the brain growth spurt. Early Hum Dev 3:79-83.

Doetsch GS (2000) Patterns in the brain. Neuronal population coding in the somatosensory system. Physiol Behav 69:187-201.

Donaldson N, Rieger R, Schuettler M, Taylor J (2008) Noise and selectivity of velocity-selective multi-electrode nerve cuffs. Med Biol Eng Comput 46:1005-1018.

Dong Y, Benveniste EN (2001) Immune function of astrocytes. Glia 36:180-190.

Dou CL, Levine JM (1995) Differential effects of glycosaminoglycans on neurite growth on laminin and L1 substrates. J Neurosci 15:8053-8066.

Douglas RJ, Koch C, Mahowald M, Martin KA, Suarez HH (1995) Recurrent excitation in neocortical circuits. Science 269:981-985.

Economo MN, White JA (2012) Membrane properties and the balance between excitation and inhibition control gamma-frequency oscillations arising from feedback inhibition. PLoS Comput Biol 8:e1002354.

Edell DJ (1986) A peripheral nerve information transducer for amputees: long-term multichannel recordings from rabbit peripheral nerves. IEEE Trans Biomed Eng 33:203-214.

Effgen GB, Hue CD, Vogel E, 3rd, Panzer MB, Meaney DF, Bass CR, Morrison B, 3rd (2012) A multiscale approach to blast neurotrauma modeling: part II: methodology for inducing blast injury to in vitro models. Front Neurol 3:23.

Egert U, Meyer T (2005) Heart on a Chip — Extracellular Multielectrode Recordings from Cardiac Myocytes in Vitro. In: Practical Methods in Cardiovascular Research (Dhein, S. *et al.*, eds), pp 432-453: Springer Berlin Heidelberg.

Egert U, Schlosshauer B, Fennrich S, Nisch W, Fejtl M, Knott T, Muller T, Hammerle H (1998) A novel organotypic long-term culture of the rat hippocampus on substrate-integrated multielectrode arrays. Brain Res Brain Res Protoc 2:229-242.

El Sayed T, Mota A, Fraternali F, Ortiz M (2008) Biomechanics of traumatic brain injury. Comput Method Appl M 197:4692-4701.

Elkin BS, Ilankova A, Morrison B (2011a) Dynamic, regional mechanical properties of the porcine brain: indentation in the coronal plane. J Biomech Eng 133:071009.

Elkin BS, Ilankovan A, Morrison B, 3rd (2010) Age-dependent regional mechanical properties of the rat hippocampus and cortex. J Biomech Eng 132:011010.

Elkin BS, Ilankovan AI, Morrison B, 3rd (2011b) A detailed viscoelastic characterization of the P17 and adult rat brain. J Neurotrauma 28:2235-2244.

Elkin BS, Morrison B, 3rd (2007) Region-specific tolerance criteria for the living brain. Stapp Car Crash J 51:127-138.

Eng LF, Ghirnikar RS (1994) GFAP and astrogliosis. Brain Pathol 4:229-237.

Engel AK, Fries P, Singer W (2001) Dynamic predictions: oscillations and synchrony in top-down processing. Nat Rev Neurosci 2:704-716.

Espinosa HD, Prorok BC (2003) Size effects on the mechanical behavior of gold thin films. J Mater Sci 38:4125-4128.

Exo J, Smith C, Smith R, Bell M (2009) Emergency treatment options for pediatric traumatic brain injury. Ped Health 3:533-541.

Falsig J, Porzgen P, Lotharius J, Leist M (2004) Specific modulation of astrocyte inflammation by inhibition of mixed lineage kinases with CEP-1347. J Immunol 173:2762-2770.

Farndale RW, Buttle DJ, Barrett AJ (1986) Improved quantitation and discrimination of sulphated glycosaminoglycans by use of dimethylmethylene blue. Biochim Biophys Acta 883:173-177.

Faul M, Xu L, Wald MM, Coronado V, Dellinger AM (2010) Traumatic brain injury in the United States: national estimates of prevalence and incidence, 2002-2006. Injury Prev 16:A268-A268.

Faulkner JR, Herrmann JE, Woo MJ, Tansey KE, Doan NB, Sofroniew MV (2004) Reactive astrocytes protect tissue and preserve function after spinal cord injury. J Neurosci 24:2143-2155.

Favata MF, Horiuchi KY, Manos EJ, Daulerio AJ, Stradley DA, Feeser WS, Van Dyk DE, Pitts WJ, Earl RA, Hobbs F, Copeland RA, Magolda RL, Scherle PA, Trzaskos JM (1998) Identification of a novel inhibitor of mitogen-activated protein kinase kinase. J Biol Chem 273:18623-18632.

Fawcett JW, Asher RA (1999) The glial scar and central nervous system repair. Brain Res Bull 49:377-391.

Feng Y, Abney TM, Okamoto RJ, Pless RB, Genin GM, Bayly PV (2010) Relative brain displacement and deformation during constrained mild frontal head impact. J R Soc Interface 7:1677-1688.

Fernaud-Espinosa I, Nieto-Sampedro M, Bovolenta P (1994) Differential effects of glycosaminoglycans on neurite outgrowth from hippocampal and thalamic neurones. J Cell Sci 107 (Pt 6):1437-1448.

Finan JD, Elkin BS, Pearson EM, Kalbian IL, Morrison B, 3rd (2012) Viscoelastic properties of the rat brain in the sagittal plane: effects of anatomical structure and age. Ann Biomed Eng 40:70-78.

Finkelstein E, Corso PS, Miller TR (2006) The incidence and economic burden of injuries in the United States. Oxford; New York: Oxford University Press.

Flint AC, Dammerman RS, Kriegstein AR (1999) Endogenous activation of metabotropic glutamate receptors in neocortical development causes neuronal calcium oscillations. Proc Natl Acad Sci U S A 96:12144-12149.

Frankel AD, Pabo CO (1988) Cellular uptake of the tat protein from human immunodeficiency virus. Cell 55:1189-1193.

Fu J, Meng X, He J, Gu J (2008) Inhibition of inflammation by a p38 MAP kinase targeted cell permeable peptide. Med Chem 4:597-604.

Fueta Y, Kawano H, Ono T, Mita T, Fukata K, Ohno K (1998) Regional differences in hippocampal excitability manifested by paired-pulse stimulation of genetically epileptic El mice. Brain Res 779:324-328.

Fujimoto ST, Longhi L, Saatman KE, Conte V, Stocchetti N, McIntosh TK (2004) Motor and cognitive function evaluation following experimental traumatic brain injury. Neurosci Biobehav Rev 28:365-378.

Gahwiler BH, Capogna M, Debanne D, McKinney RA, Thompson SM (1997) Organotypic slice cultures: a technique has come of age. Trends Neurosci 20:471-477.

Galarreta M, Hestrin S (1998) Frequency-dependent synaptic depression and the balance of excitation and inhibition in the neocortex. Nat Neurosci 1:587-594.

Galbraith JA, Thibault LE, Matteson DR (1993) Mechanical and electrical responses of the squid giant axon to simple elongation. J Biomech Eng 115:13-22.

Gao S, Simon MJ, Morrison B, 3rd, Banta S (2009) Bifunctional chimeric fusion proteins engineered for DNA delivery: Optimization of the protein to DNA ratio. Biochim Biophys Acta.

Gao X, Chen J (2011) Mild traumatic brain injury results in extensive neuronal degeneration in the cerebral cortex. J Neuropathol Exp Neurol 70:183-191.

Gao X, Deng P, Xu ZC, Chen J (2011) Moderate traumatic brain injury causes acute dendritic and synaptic degeneration in the hippocampal dentate gyrus. PLoS One 6:e24566.

Garaschuk O, Hanse E, Konnerth A (1998) Developmental profile and synaptic origin of early network oscillations in the CA1 region of rat neonatal hippocampus. J Physiol 507 (Pt 1):219-236.

Garaschuk O, Linn J, Eilers J, Konnerth A (2000) Large-scale oscillatory calcium waves in the immature cortex. Nat Neurosci 3:452-459.

Gean AD, Fischbein NJ (2010) Head trauma. Neuroimaging Clin N Am 20:527-556.

Geddes DM, LaPlaca MC, Cargill RS, 2nd (2003) Susceptibility of hippocampal neurons to mechanically induced injury. Exp Neurol 184:420-427.

Georgiou AP, Manara AR (2013) Role of therapeutic hypothermia in improving outcome after traumatic brain injury: a systematic review. Br J Anaesth 110:357-367.

Ghirnikar RS, Yu AC, Eng LF (1994) Astrogliosis in culture: III. Effect of recombinant retrovirus expressing antisense glial fibrillary acidic protein RNA. J Neurosci Res 38:376-385.

Gibson CJ, Meyer RC, Hamm RJ (2010) Traumatic brain injury and the effects of diazepam, diltiazem, and MK-801 on GABA-A receptor subunit expression in rat hippocampus. J Biomed Sci 17:38.

Giordano C, Cloots RJ, van Dommelen JA, Kleiven S (2014) The influence of anisotropy on brain injury prediction. J Biomech 47:1052-1059.

Giordano C, Kleiven S (2014) Connecting fractional anisotropy from medical images with mechanical anisotropy of a hyperviscoelastic fibre-reinforced constitutive model for brain tissue. J R Soc Interface 11:20130914.

Giza CC, Maria NS, Hovda DA (2006) N-methyl-D-aspartate receptor subunit changes after traumatic injury to the developing brain. J Neurotrauma 23:950-961.

Glatting G, Kletting P, Reske SN, Hohl K, Ring C (2007) Choosing the optimal fit function: comparison of the Akaike information criterion and the F-test. Med Phys 34:4285-4292.

Godbolt AK, Deboussard CN, Stenberg M, Lindgren M, Ulfarsson T, Borg J (2013) Disorders of consciousness after severe traumatic brain injury: a Swedish-Icelandic study of incidence, outcomes and implications for optimizing care pathways. J Rehabil Med 45:741-748.

Goforth PB, Ellis EF, Satin LS (2004) Mechanical injury modulates AMPA receptor kinetics via an NMDA receptor-dependent pathway. J Neurotrauma 21:719-732.

Gorrn P, Cao WZ, Wagner S (2011) Isotropically stretchable gold conductors on elastomeric substrates. Soft Matter 7:7177-7180.

Graudejus O, Gorrn P, Wagner S (2010) Controlling the morphology of gold films on poly(dimethylsiloxane). ACS Appl Mater Interfaces 2:1927-1933.

Graudejus O, Morrison B, 3rd, Goletiani C, Yu Z, Wagner S (2012) Encapsulating elastically stretchable neural interfaces: Yield, resolution, and recording/stimulation of neural activity. Adv Funct Mater 22:640-651.

Graudejus O, Yu Z, Jones J, Morrison B, Wagner S (2009) Characterization of an elastically stretchable microelectrode array and its application to neural field potential recordings. J Electrochem Soc 156:P85-P94.

Green M, Loewenstein PM (1988) Autonomous functional domains of chemically synthesized human immunodeficiency virus tat trans-activator protein. Cell 55:1179-1188.

Guan QH, Pei DS, Liu XM, Wang XT, Xu TL, Zhang GY (2006a) Neuroprotection against ischemic brain injury by SP600125 via suppressing the extrinsic and intrinsic pathways of apoptosis. Brain Res 1092:36-46.

Guan QH, Pei DS, Zong YY, Xu TL, Zhang GY (2006b) Neuroprotection against ischemic brain injury by a small peptide inhibitor of c-Jun N-terminal kinase (JNK) via nuclear and non-nuclear pathways. Neuroscience 139:609-627.

Gulyas AI, Megias M, Emri Z, Freund TF (1999) Total number and ratio of excitatory and inhibitory synapses converging onto single interneurons of different types in the CA1 area of the rat hippocampus. J Neurosci 19:10082-10097.

Guo L, Meacham KW, Hochman S, DeWeerth SP (2010) A PDMS-based conical-well microelectrode array for surface stimulation and recording of neural tissues. IEEE Trans Biomed Eng 57:2485-2494.

Guo Y, DuBois Bowman F, Kilts C (2008) Predicting the brain response to treatment using a Bayesian hierarchical model with application to a study of schizophrenia. Hum Brain Mapp 29:1092-1109.

Gurkoff GG, Giza CC, Hovda DA (2006) Lateral fluid percussion injury in the developing rat causes an acute, mild behavioral dysfunction in the absence of significant cell death. Brain Res 1077:24-36.

Haigh S, Karanovic O, Wilkinson F, Wilkins A (2012) Cortical hyperexcitability in migraine and aversion to patterns. Cephalalgia 32:236-240.

Hamby ME, Sofroniew MV (2010) Reactive astrocytes as therapeutic targets for CNS disorders. Neurotherapeutics 7:494-506.

Hardy WN, Mason MJ, Foster CD, Shah CS, Kopacz JM, Yang KH, King AI, Bishop J, Bey M, Anderst W, Tashman S (2007) A study of the response of the human cadaver head to impact. Stapp Car Crash J 51:17-80.

Harris KD, Csicsvari J, Hirase H, Dragoi G, Buzsaki G (2003) Organization of cell assemblies in the hippocampus. Nature 424:552-556.

Hefft S, Jonas P (2005) Asynchronous GABA release generates long-lasting inhibition at a hippocampal interneuron-principal neuron synapse. Nat Neurosci 8:1319-1328.

Henle C, Raab M, Cordeiro JG, Doostkam S, Schulze-Bonhage A, Stieglitz T, Rickert J (2011) First long term in vivo study on subdurally implanted micro-ECoG electrodes, manufactured with a novel laser technology. Biomed Microdevices 13:59-68.

Henneberger C, Papouin T, Oliet SH, Rusakov DA (2010) Long-term potentiation depends on release of D-serine from astrocytes. Nature 463:232-236.

Heuschkel MO, Fejtl M, Raggenbass M, Bertrand D, Renaud P (2002) A three-dimensional multi-electrode array for multi-site stimulation and recording in acute brain slices. J Neurosci Meth 114:135-148.

Hicks RR, Smith DH, Lowenstein DH, Saint Marie R, McIntosh TK (1993) Mild experimental brain injury in the rat induces cognitive deficits associated with regional neuronal loss in the hippocampus. J Neurotrauma 10:405-414.

Hillary F, Moelter ST, Schatz P, Chute DL (2001) Seatbelts contribute to location of lesion in moderate to severe closed head trauma. Arch Clin Neuropsychol 16:171-181.

Hollands EC, Dale TJ, Baxter AW, Meadows HJ, Powell AJ, Clare JJ, Trezise DJ (2009) Population patch-clamp electrophysiology analysis of recombinant GABAA alpha1beta3gamma2 channels expressed in HEK-293 cells. J Biomol Screen 14:769-780.

Hopcroft MA, Nix WD, Kenny TW (2010) What is the Young's Modulus of Silicon? J Microelectromech S 19:229-238.

Hoskison MM, Moore AN, Hu B, Orsi S, Kobori N, Dash PK (2009) Persistent working memory dysfunction following traumatic brain injury: evidence for a time-dependent mechanism. Neuroscience 159:483-491.

Hsiao HY, Mak OT, Yang CS, Liu YP, Fang KM, Tzeng SF (2007) TNF-alpha/IFN-gamma-induced iNOS expression increased by prostaglandin E2 in rat primary astrocytes via EP2-evoked cAMP/PKA and intracellular calcium signaling. Glia 55:214-223.

Hua LL, Zhao ML, Cosenza M, Kim MO, Huang H, Tanowitz HB, Brosnan CF, Lee SC (2002) Role of mitogen-activated protein kinases in inducible nitric oxide synthase and TNFalpha expression in human fetal astrocytes. J Neuroimmunol 126:180-189.

Hussar CR, Pasternak T (2012) Memory-guided sensory comparisons in the prefrontal cortex: contribution of putative pyramidal cells and interneurons. J Neurosci 32:2747-2761.

Hyder AA, Wunderlich CA, Puvanachandra P, Gururaj G, Kobusingye OC (2007) The impact of traumatic brain injuries: a global perspective. NeuroRehabilitation 22:341-353.

Ji K, Miyauchi J, Tsirka SE (2013) Microglia: an active player in the regulation of synaptic activity. Neural Plast 2013:627325.

Jia F, Xie X, Zhou Y (2004) Short-term depression of synaptic transmission from rat lateral geniculate nucleus to primary visual cortex in vivo. Brain Res 1002:158-161.

Johnstone M, Gearing AJ, Miller KM (1999) A central role for astrocytes in the inflammatory response to beta-amyloid; chemokines, cytokines and reactive oxygen species are produced. J Neuroimmunol 93:182-193.

Jones EV, Bouvier DS (2014) Astrocyte-secreted matricellular proteins in CNS remodelling during development and disease. Neural Plast 2014:321209.

Jones LL, Tuszynski MH (2002) Spinal cord injury elicits expression of keratan sulfate proteoglycans by macrophages, reactive microglia, and oligodendrocyte progenitors. J Neurosci 22:4611-4624.

Joy RM, Albertson TE (1993) NMDA receptors have a dominant role in population spike-paired pulse facilitation in the dentate gyrus of urethane-anesthetized rats. Brain Res 604:273-282.

Juraska JM, Fifkova E (1979) An electron microscope study of the early postnatal development of the visual cortex of the hooded rat. J Comp Neurol 183:257-267.

Kang WH, Morrison B, 3rd (2014) Functional tolerance to mechanical deformation developed from organotypic hippocampal slice cultures. Biomech Model Mechanobiol.

Kao CQ, Goforth PB, Ellis EF, Satin LS (2004) Potentiation of GABA(A) currents after mechanical injury of cortical neurons. J Neurotrauma 21:259-270.

Katz LC, Shatz CJ (1996) Synaptic activity and the construction of cortical circuits. Science 274:1133-1138.

Kernie SG, Erwin TM, Parada LF (2001) Brain remodeling due to neuronal and astrocytic proliferation after controlled cortical injury in mice. J Neurosci Res 66:317-326.

Kettenmann H, Banati R, Walz W (1993) Electrophysiological behavior of microglia. Glia 7:93-101.

Kharlamov EA, Lepsveridze E, Meparishvili M, Solomonia RO, Lu B, Miller ER, Kelly KM, Mtchedlishvili Z (2011) Alterations of GABA(A) and glutamate receptor subunits and heat shock protein in rat hippocampus following traumatic brain injury and in posttraumatic epilepsy. Epilepsy Res 95:20-34.

Khuman J, Meehan WP, 3rd, Zhu X, Qiu J, Hoffmann U, Zhang J, Giovannone E, Lo EH, Whalen MJ (2011) Tumor necrosis factor alpha and Fas receptor contribute to cognitive deficits independent of cell death after concussive traumatic brain injury in mice. J Cereb Blood Flow Metab 31:778-789.

Kim DH, Viventi J, Amsden JJ, Xiao J, Vigeland L, Kim YS, Blanco JA, Panilaitis B, Frechette ES, Contreras D, Kaplan DL, Omenetto FG, Huang Y, Hwang KC, Zakin MR, Litt B, Rogers JA (2010) Dissolvable films of silk fibroin for ultrathin conformal bio-integrated electronics. Nat Mater 9:511-517.

Kim S, Bhandari R, Klein M, Negi S, Rieth L, Tathireddy P, Toepper M, Oppermann H, Solzbacher F (2009) Integrated wireless neural interface based on the Utah electrode array. Biomed Microdevices 11:453-466.

Kim WR, Kim JY, Moon Y, Kim HJ, Kim H, Sun W (2012) Regional difference of reactive astrogliosis following traumatic brain injury revealed by hGFAP-GFP transgenic mice. Neurosci Lett 513:155-159.

Kim YJ, Hwang SY, Oh ES, Oh S, Han IO (2006) IL-1beta, an immediate early protein secreted by activated microglia, induces iNOS/NO in C6 astrocytoma cells through p38 MAPK and NF-kappaB pathways. J Neurosci Res 84:1037-1046.

Kim YT, Hitchcock RW, Bridge MJ, Tresco PA (2004) Chronic response of adult rat brain tissue to implants anchored to the skull. Biomaterials 25:2229-2237.

Kimelberg HK, Nedergaard M (2010) Functions of astrocytes and their potential as therapeutic targets. Neurotherapeutics 7:338-353.

Kimpara H, Iwamoto M (2012) Mild traumatic brain injury predictors based on angular accelerations during impacts. Ann Biomed Eng 40:114-126.

Kinnunen KM, Greenwood R, Powell JH, Leech R, Hawkins PC, Bonnelle V, Patel MC, Counsell SJ, Sharp DJ (2011) White matter damage and cognitive impairment after traumatic brain injury. Brain 134:449-463.

Kitzmiller J, Beversdorf D, Hansford D (2006) Fabrication and testing of microelectrodes for small-field cortical surface recordings. Biomed Microdevices 8:81-85.

Klausberger T, Magill PJ, Marton LF, Roberts JD, Cobden PM, Buzsaki G, Somogyi P (2003) Brain-state- and cell-type-specific firing of hippocampal interneurons in vivo. Nature 421:844-848.

Kleiven S (2006) Evaluation of head injury criteria using a finite element model validated against experiments on localized brain motion, intracerebral acceleration, and intracranial pressure. Int J Crashworthines 11:65-79.

Kleiven S (2007) Predictors for traumatic brain injuries evaluated through accident reconstructions. Stapp Car Crash J 51:81-114.

Kleiven S, Hardy WN (2002) Correlation of an FE model of the human head with local brain motion--consequences for injury prediction. Stapp Car Crash J 46:123-144.

Kobori N, Dash PK (2006) Reversal of brain injury-induced prefrontal glutamic acid decarboxylase expression and working memory deficits by D1 receptor antagonism. J Neurosci 26:4236-4246.

Kolias AG, Guilfoyle MR, Helmy A, Allanson J, Hutchinson PJ (2013) Traumatic brain injury in adults. Pract Neurol 13:228-235.

Kralik JD, Dimitrov DF, Krupa DJ, Katz DB, Cohen D, Nicolelis MA (2001) Techniques for long-term multisite neuronal ensemble recordings in behaving animals. Methods 25:121-150.

Kumar A, Zou L, Yuan X, Long Y, Yang K (2002) N-methyl-D-aspartate receptors: transient loss of NR1/NR2A/NR2B subunits after traumatic brain injury in a rodent model. J Neurosci Res 67:781-786.

Kumar S, McDonnell PC, Gum RJ, Hand AT, Lee JC, Young PR (1997) Novel homologues of CSBP/p38 MAP kinase: activation, substrate specificity and sensitivity to inhibition by pyridinyl imidazoles. Biochem Biophys Res Commun 235:533-538.

Lacour SP, Adrega T (2010) Stretchable gold conductors embedded in PDMS and patterned by photolithography: fabrication and electromechanical characterization. J Micromech Microeng 20.

Lacour SP, Benmerah S, Tarte E, FitzGerald J, Serra J, McMahon S, Fawcett J, Graudejus O, Yu Z, Morrison B, 3rd (2010) Flexible and stretchable micro-electrodes for in vitro and in vivo neural interfaces. Med Biol Eng Comput 48:945-954.

Lacour SP, Chan D, Wagner S, Li T, Suo ZG (2006) Mechanisms of reversible stretchability of thin metal films on elastomeric substrates. Appl Phys Lett 88.

Lacour SP, Graz IM, Cotton DPJ, Robinson A (2011) Silicone substrate with in situ strain relief for stretchable thin-film transistors. Appl Phys Lett 98.

Lacour SP, Jones J, Wagner S, Li T, Suo ZG (2005) Stretchable interconnects for elastic electronic surfaces. P Ieee 93:1459-1467.

Lacour SP, Wagner S, Huang ZY, Suo Z (2003) Stretchable gold conductors on elastomeric substrates. Appl Phys Lett 82:2404-2406.

Laird MD, Vender JR, Dhandapani KM (2008) Opposing roles for reactive astrocytes following traumatic brain injury. Neurosignals 16:154-164.

Lamy M, Baumgartner D, Willinger R, Yoganandan N, Stemper BD (2011) Study of mild traumatic brain injuries using experiments and finite element modeling. Annals of advances in automotive medicine / Annual Scientific Conference Association for the Advancement of Automotive Medicine Association for the Advancement of Automotive Medicine Scientific Conference 55:125-135.

Lamy M, Baumgartner D, Yoganandan N, Stemper BD, Willinger R (2013) Experimentally validated three-dimensional finite element model of the rat for mild traumatic brain injury. Med Biol Eng Comput 51:353-365.

Langlois JA, Rutland-Brown W, Thomas KE (2005) The incidence of traumatic brain injury among children in the United States: differences by race. J Head Trauma Rehabil 20:229-238.

Langlois JA, Rutland-Brown W, Wald MM (2006) The epidemiology and impact of traumatic brain injury: a brief overview. J Head Trauma Rehabil 21:375-378.

LaPlaca MC, Cullen DK, McLoughlin JJ, Cargill RS, 2nd (2005) High rate shear strain of three-dimensional neural cell cultures: a new in vitro traumatic brain injury model. J Biomech 38:1093-1105.

Lea PM, Custer SJ, Vicini S, Faden AI (2002) Neuronal and glial mGluR5 modulation prevents stretch-induced enhancement of NMDA receptor current. Pharmacol Biochem Behav 73:287-298.

Lee JC, Kumar S, Griswold DE, Underwood DC, Votta BJ, Adams JL (2000) Inhibition of p38 MAP kinase as a therapeutic strategy. Immunopharmacology 47:185-201.

Lee JW, Lee YK, Yuk DY, Choi DY, Ban SB, Oh KW, Hong JT (2008) Neuro-inflammation induced by lipopolysaccharide causes cognitive impairment through enhancement of beta-amyloid generation. J Neuroinflammation 5:37.

Lee S, Hjerling-Leffler J, Zagha E, Fishell G, Rudy B (2010) The largest group of superficial neocortical GABAergic interneurons expresses ionotropic serotonin receptors. J Neurosci 30:16796-16808.

Lee S, Ueno M, Yamashita T (2011) Axonal remodeling for motor recovery after traumatic brain injury requires downregulation of gamma-aminobutyric acid signaling. Cell Death Dis 2:e133.

Lee SC, Dickson DW, Brosnan CF (1995) Interleukin-1, nitric oxide and reactive astrocytes. Brain Behav Immun 9:345-354.

Lefort S, Tomm C, Floyd Sarria JC, Petersen CC (2009) The excitatory neuronal network of the C2 barrel column in mouse primary somatosensory cortex. Neuron 61:301-316.

Leinekugel X, Khalilov I, McLean H, Caillard O, Gaiarsa JL, Ben-Ari Y, Khazipov R (1999) GABA is the principal fast-acting excitatory transmitter in the neonatal brain. Adv Neurol 79:189-201.

Levchakov A, Linder-Ganz E, Raghupathi R, Margulies SS, Gefen A (2006) Computational studies of strain exposures in neonate and mature rat brains during closed head impact. J Neurotrauma 23:1570-1580.

Levin HS, Hanten G, Chang CC, Zhang L, Schachar R, Ewing-Cobbs L, Max JE (2002) Working memory after traumatic brain injury in children. Ann Neurol 52:82-88.

Levine B, Fujiwara E, O'Connor C, Richard N, Kovacevic N, Mandic M, Restagno A, Easdon C, Robertson IH, Graham SJ, Cheung G, Gao F, Schwartz ML, Black SE (2006) In vivo characterization of traumatic brain injury neuropathology with structural and functional neuroimaging. J Neurotrauma 23:1396-1411.

Lewis DA (2000) GABAergic local circuit neurons and prefrontal cortical dysfunction in schizophrenia. Brain Res Brain Res Rev 31:270-276.

Li G, Simon MJ, Cancel LM, Shi ZD, Ji X, Tarbell JM, Morrison B, 3rd, Fu BM (2010a) Permeability of endothelial and astrocyte cocultures: in vitro blood-brain barrier models for drug delivery studies. Ann Biomed Eng 38:2499-2511.

Li LM, Menon DK, Janowitz T (2014) Cross-sectional analysis of data from the U.S. clinical trials database reveals poor translational clinical trial effort for traumatic brain injury, compared with stroke. PLoS One 9:e84336.

Li T, Huang ZY, Suo Z, Lacour SP, Wagner S (2004) Stretchability of thin metal films on elastomer substrates. Appl Phys Lett 85:3435-3437.

Li X, Cui D, Jiruska P, Fox JE, Yao X, Jefferys JG (2007a) Synchronization measurement of multiple neuronal populations. J Neurophysiol 98:3341-3348.

Li X, Ouyang G, Usami A, Ikegaya Y, Sik A (2010b) Scale-free topology of the CA3 hippocampal network: a novel method to analyze functional neuronal assemblies. Biophys J 98:1733-1741.

Li X, Zhou W, Zeng S, Liu M, Luo Q (2007b) Long-term recording on multi-electrode array reveals degraded inhibitory connection in neuronal network development. Biosens Bioelectron 22:1538-1543.

Lifshitz J, Friberg H, Neumar RW, Raghupathi R, Welsh FA, Janmey P, Saatman KE, Wieloch T, Grady MS, McIntosh TK (2003) Structural and functional damage sustained by mitochondria after traumatic brain injury in the rat: evidence for differentially sensitive populations in the cortex and hippocampus. J Cereb Blood Flow Metab 23:219-231.

Lyeth BG, Jenkins LW, Hamm RJ, Dixon CE, Phillips LL, Clifton GL, Young HF, Hayes RL (1990) Prolonged memory impairment in the absence of hippocampal cell death following traumatic brain injury in the rat. Brain Res 526:249-258.

Maas AI, Roozenbeek B, Manley GT (2010) Clinical trials in traumatic brain injury: past experience and current developments. Neurotherapeutics 7:115-126.

Maas AI, Steyerberg EW, Murray GD, Bullock R, Baethmann A, Marshall LF, Teasdale GM (1999) Why have recent trials of neuroprotective agents in head injury failed to show convincing efficacy? A pragmatic analysis and theoretical considerations. Neurosurgery 44:1286-1298.

Maas AI, Stocchetti N, Bullock R (2008) Moderate and severe traumatic brain injury in adults. Lancet Neurol 7:728-741.

Maddahi A, Edvinsson L (2010) Cerebral ischemia induces microvascular pro-inflammatory cytokine expression via the MEK/ERK pathway. J Neuroinflammation 7:14.

Mandell JW, Gocan NC, Vandenberg SR (2001) Mechanical trauma induces rapid astroglial activation of ERK/MAP kinase: Evidence for a paracrine signal. Glia 34:283-295.

Mao H, Elkin BS, Genthikatti VV, Morrison B, 3rd, Yang KH (2013) Why is CA3 more vulnerable than CA1 in experimental models of controlled cortical impact-induced brain injury? J Neurotrauma 30:1521-1530.

Mao H, Zhang L, Yang KH, King AI (2006) Application of a finite element model of the brain to study traumatic brain injury mechanisms in the rat. Stapp Car Crash J 50:583-600.

Maragakis NJ, Rothstein JD (2006) Mechanisms of Disease: astrocytes in neurodegenerative disease. Nat Clin Pract Neurol 2:679-689.

Margineanu DG, Wulfert E (2000) Differential paired-pulse effects of gabazine and bicuculline in rat hippocampal CA3 area. Brain Res Bull 51:69-74.

Margulies SS, Thibault LE (1989) An analytical model of traumatic diffuse brain injury. J Biomech Eng 111:241-249.

Margulies SS, Thibault LE (1992) A proposed tolerance criterion for diffuse axonal injury in man. J Biomech 25:917-923.

Margulies SS, Thibault LE, Gennarelli TA (1990) Physical model simulations of brain injury in the primate. J Biomech 23:823-836.

Matsuyama S, Taniguchi T, Kadoyama K, Matsumoto A (2008) Long-term potentiation-like facilitation through GABAA receptor blockade in the mouse dentate gyrus in vivo. Neuroreport 19:1809-1813.

McAllister TW, Ford JC, Ji S, Beckwith JG, Flashman LA, Paulsen K, Greenwald RM (2012) Maximum principal strain and strain rate associated with concussion diagnosis correlates with changes in corpus callosum white matter indices. Ann Biomed Eng 40:127-140.

McAllister TW, Saykin AJ, Flashman LA, Sparling MB, Johnson SC, Guerin SJ, Mamourian AC, Weaver JB, Yanofsky N (1999) Brain activation during working memory 1 month after mild traumatic brain injury: a functional MRI study. Neurology 53:1300-1308.

McClain MA, Clements IP, Shafer RH, Bellamkonda RV, LaPlaca MC, Allen MG (2011) Highly-compliant, microcable neuroelectrodes fabricated from thin-film gold and PDMS. Biomed Microdevices 13:361-373.

McKeon RJ, Hoke A, Silver J (1995) Injury-induced proteoglycans inhibit the potential for laminin-mediated axon growth on astrocytic scars. Exp Neurol 136:32-43.

McKeon RJ, Schreiber RC, Rudge JS, Silver J (1991) Reduction of neurite outgrowth in a model of glial scarring following CNS injury is correlated with the expression of inhibitory molecules on reactive astrocytes. J Neurosci 11:3398-3411.

Meacham KW, Giuly RJ, Guo L, Hochman S, DeWeerth SP (2008) A lithographically-patterned, elastic multi-electrode array for surface stimulation of the spinal cord. Biomed Microdevices 10:259-269.

Meacham KW, Guo L, Deweerth SP, Hochman S (2011) Selective stimulation of the spinal cord surface using a stretchable microelectrode array. Front Neuroeng 4:5.

Meaney DF, Smith DH, Shreiber DI, Bain AC, Miller RT, Ross DT, Gennarelli TA (1995) Biomechanical analysis of experimental diffuse axonal injury. J Neurotrauma 12:689-694.

Mehring C, Rickert J, Vaadia E, Cardosa de Oliveira S, Aertsen A, Rotter S (2003) Inference of hand movements from local field potentials in monkey motor cortex. Nat Neurosci 6:1253-1254.

Merker J, Lupton D, Topfer M, Knake H (2001) High Temperature Mechanical Properties of the Platinum Group Metals ELASTIC PROPERTIES OF PLATINUM, RHODIUM AND IRIDIUM AND THEIR ALLOYS AT HIGH TEMPERATURES. Platin Met Rev 45:74-82.

Mi S, Miller RH, Tang W, Lee X, Hu B, Wu W, Zhang Y, Shields CB, Zhang Y, Miklasz S, Shea D, Mason J, Franklin RJ, Ji B, Shao Z, Chedotal A, Bernard F, Roulois A, Xu J, Jung V, Pepinsky B (2009) Promotion of central nervous system remyelination by induced differentiation of oligodendrocyte precursor cells. Ann Neurol 65:304-315.

Miller WJ, Leventhal I, Scarsella D, Haydon PG, Janmey P, Meaney DF (2009) Mechanically induced reactive gliosis causes ATP-mediated alterations in astrocyte stiffness. J Neurotrauma 26:789-797.

Minev IR, Lacour SP (2010) Impedance spectroscopy on stretchable microelectrode arrays. Appl Phys Lett 97.

Molina JA, Jimenez-Jimenez FJ, Orti-Pareja M, Navarro JA (1998) The role of nitric oxide in neurodegeneration. Potential for pharmacological intervention. Drugs Aging 12:251-259.

Molinaro AM, Simon R, Pfeiffer RM (2005) Prediction error estimation: a comparison of resampling methods. Bioinformatics 21:3301-3307.

Monick MM, Powers LS, Gross TJ, Flaherty DM, Barrett CW, Hunninghake GW (2006) Active ERK contributes to protein translation by preventing JNK-dependent inhibition of protein phosphatase 1. J Immunol 177:1636-1645.

Moon LD, Asher RA, Rhodes KE, Fawcett JW (2001) Regeneration of CNS axons back to their target following treatment of adult rat brain with chondroitinase ABC. Nat Neurosci 4:465-466.

Morganti-Kossmann MC, Rancan M, Stahel PF, Kossmann T (2002) Inflammatory response in acute traumatic brain injury: a double-edged sword. Curr Opin Crit Care 8:101-105.

Mori T, Wang X, Jung JC, Sumii T, Singhal AB, Fini ME, Dixon CE, Alessandrini A, Lo EH (2002) Mitogen-activated protein kinase inhibition in traumatic brain injury: in vitro and in vivo effects. J Cereb Blood Flow Metab 22:444-452.

Morrison B, 3rd, Cater HL, Benham CD, Sundstrom LE (2006) An in vitro model of traumatic brain injury utilising two-dimensional stretch of organotypic hippocampal slice cultures. J Neurosci Methods 150:192-201.

Morrison B, 3rd, Cater HL, Wang CC, Thomas FC, Hung CT, Ateshian GA, Sundstrom LE (2003) A tissue level tolerance criterion for living brain developed with an in vitro model of traumatic mechanical loading. Stapp Car Crash J 47:93-105.

Morrison B, 3rd, Saatman KE, Meaney DF, McIntosh TK (1998) In vitro central nervous system models of mechanically induced trauma: a review. J Neurotrauma 15:911-928.

Morrison III B, Elkin BS, Dolle JP, Yarmush ML (2011) In vitro models of traumatic brain injury. Annual Review of Biomedical Engineering 13:91-126.

Morrison III B, Saatman KE, Meaney DF, McIntosh TK (1998) In vitro central nervous system models of mechanically induced trauma: a review. JNeurotrauma 15:911-928.

Moss WC, King MJ, Blackman EG (2014) Towards reducing impact-induced brain injury: lessons from a computational study of army and football helmet pads. Comput Methods Biomech Biomed Engin 17:1173-1184.

Munoz L, Ralay Ranaivo H, Roy SM, Hu W, Craft JM, McNamara LK, Chico LW, Van Eldik LJ, Watterson DM (2007) A novel p38 alpha MAPK inhibitor suppresses brain proinflammatory cytokine up-regulation and attenuates synaptic dysfunction and behavioral deficits in an Alzheimer's disease mouse model. J Neuroinflammation 4:21.

Murphy S, Simmons ML, Agullo L, Garcia A, Feinstein DL, Galea E, Reis DJ, Minc-Golomb D, Schwartz JP (1993) Synthesis of nitric oxide in CNS glial cells. Trends Neurosci 16:323-328.

Nakajima K, Tohyama Y, Kohsaka S, Kurihara T (2004) Protein kinase C alpha requirement in the activation of p38 mitogen-activated protein kinase, which is linked to the induction of tumor necrosis factor alpha in lipopolysaccharide-stimulated microglia. Neurochem Int 44:205-214.

Namura S, Iihara K, Takami S, Nagata I, Kikuchi H, Matsushita K, Moskowitz MA, Bonventre JV, Alessandrini A (2001) Intravenous administration of MEK inhibitor U0126 affords brain protection against forebrain ischemia and focal cerebral ischemia. Proc Natl Acad Sci U S A 98:11569-11574.

Narayan RK, Michel ME, Ansell B, Baethmann A, Biegon A, Bracken MB, Bullock MR, Choi SC, Clifton GL, Contant CF, Coplin WM, Dietrich WD, Ghajar J, Grady SM, Grossman RG, Hall ED, Heetderks W, Hovda DA, Jallo J, Katz RL, Knoller N, Kochanek PM, Maas AI, Majde J, Marion DW, Marmarou A, Marshall LF, McIntosh TK, Miller E, Mohberg N, Muizelaar JP, Pitts LH, Quinn P, Riesenfeld G, Robertson CS, Strauss KI, Teasdale G, Temkin N, Tuma R, Wade C, Walker MD, Weinrich M, Whyte J, Wilberger J, Young AB, Yurkewicz L (2002) Clinical trials in head injury. J Neurotrauma 19:503-557.

Navarrete M, Perea G, Maglio L, Pastor J, Garcia de Sola R, Araque A (2013) Astrocyte calcium signal and gliotransmission in human brain tissue. Cereb Cortex 23:1240-1246.

Ning B, Li Z, Zhu N, Hou G, Pang Q (2013) Traumatic brain injury induces a downregulation of MSK1 in rat brain cortex. J Mol Neurosci 49:380-386.

Nirula R, Mock CN, Nathens AB, Grossman DC (2004) The new car assessment program: does it predict the relative safety of vehicles in actual crashes? J Trauma 57:779-786.

Nisch W, Bock J, Egert U, Hammerle H, Mohr A (1994) A thin film microelectrode array for monitoring extracellular neuronal activity in vitro. Biosens Bioelectron 9:737-741.

Noraberg J, Kristensen BW, Zimmer J (1999) Markers for neuronal degeneration in organotypic slice cultures. Brain Res Brain Res Protoc 3:278-290.

Novak JL, Wheeler BC (1988) Multisite hippocampal slice recording and stimulation using a 32 element microelectrode array. J Neurosci Methods 23:149-159.

Oka H, Shimono K, Ogawa R, Sugihara H, Taketani M (1999) A new planar multielectrode array for extracellular recording: application to hippocampal acute slice. J Neurosci Methods 93:61-67.

Ommaya AK, Gennarelli TA (1974) Cerebral concussion and traumatic unconsciousness. Correlation of experimental and clinical observations of blunt head injuries. Brain 97:633-654.

Ommaya AK, Ommaya AK, Yarnell P, Hirsch AE, Harris EH (1967) Scaling of experimental data on cerebral concussion in sub-human primates to concussion threshold for man. SAE Technical Papers.

Osteen CL, Giza CC, Hovda DA (2004) Injury-induced alterations in N-methyl-D-aspartate receptor subunit composition contribute to prolonged 45calcium accumulation following lateral fluid percussion. Neuroscience 128:305-322.

Ostergaard K, Finsen B, Zimmer J (1995) Organotypic slice cultures of the rat striatum: an immunocytochemical, histochemical and in situ hybridization study of somatostatin, neuropeptide Y, nicotinamide adenine dinucleotide phosphate-diaphorase, and enkephalin. Exp Brain Res 103:70-84.

Otani N, Nawashiro H, Fukui S, Nomura N, Yano A, Miyazawa T, Shima K (2002) Differential activation of mitogen-activated protein kinase pathways after traumatic brain injury in the rat hippocampus. J Cereb Blood Flow Metab 22:327-334.

Ounpraseuth S, Lensing SY, Spencer HJ, Kodell RL (2012) Estimating misclassification error: a closer look at cross-validation based methods. BMC Res Notes 5:656.

Pan Y, Sullivan D, Shreiber DI, Pelegri AA (2013) Finite element modeling of CNS white matter kinematics: Use of a 3D RVE to determine material properties. Front Bioeng Biotechnol 1:19.

Panatier A, Theodosis DT, Mothet JP, Touquet B, Pollegioni L, Poulain DA, Oliet SH (2006) Glia-derived D-serine controls NMDA receptor activity and synaptic memory. Cell 125:775-784.

Panickar KS, Norenberg MD (2005) Astrocytes in cerebral ischemic injury: morphological and general considerations. Glia 50:287-298.

Pascual O, Ben Achour S, Rostaing P, Triller A, Bessis A (2012) Microglia activation triggers astrocyte-mediated modulation of excitatory neurotransmission. Proc Natl Acad Sci U S A 109:E197-205.

Pashley DW (1960) A study of the deformation and fracture of single-crystal gold films of high strength inside an electron microscope. Proc R Soc Lon Ser-A 255:218-&.

Patel TP, Ventre SC, Meaney DF (2012) Dynamic changes in neural circuit topology following mild mechanical injury in vitro. Ann Biomed Eng 40:23-36.

Patton DA, McIntosh AS, Kleiven S, Fréchède B (2012) Injury data from unhelmeted football head impacts evaluated against critical strain tolerance curves. Proceedings of the Institution of Mechanical Engineers, Part P: Journal of Sports Engineering and Technology 226:177-184.

Pawate S, Bhat NR (2006) C-Jun N-terminal kinase (JNK) regulation of iNOS expression in glial cells: predominant role of JNK1 isoform. Antioxid Redox Signal 8:903-909.

Pekny M, Nilsson M (2005) Astrocyte activation and reactive gliosis. Glia 50:427-434.

Pellman EJ, Viano DC, Tucker AM, Casson IR, Waeckerle JF (2003) Concussion in professional football: reconstruction of game impacts and injuries. Neurosurgery 53:799-812; discussion 812-794.

Perea G, Yang A, Boyden ES, Sur M (2014) Optogenetic astrocyte activation modulates response selectivity of visual cortex neurons in vivo. Nat Commun 5:3262.

Perez J, Springthorpe VS, Sattar SA (2005) Activity of selected oxidizing microbicides against the spores of Clostridium difficile: relevance to environmental control. Am J Infect Control 33:320-325.

Piao CS, Kim JB, Han PL, Lee JK (2003) Administration of the p38 MAPK inhibitor SB203580 affords brain protection with a wide therapeutic window against focal ischemic insult. J Neurosci Res 73:537-544.

Pimashkin A, Kastalskiy I, Simonov A, Koryagina E, Mukhina I, Kazantsev V (2011) Spiking signatures of spontaneous activity bursts in hippocampal cultures. Front Comput Neurosci 5:46.

Pitcher JB, Ogston KM, Miles TS (2003) Age and sex differences in human motor cortex input-output characteristics. J Physiol 546:605-613.

Polikov VS, Tresco PA, Reichert WM (2005) Response of brain tissue to chronically implanted neural electrodes. J Neurosci Methods 148:1-18.

Posmantur RM, Newcomb JK, Kampfl A, Hayes RL (2000) Light and confocal microscopic studies of evolutionary changes in neurofilament proteins following cortical impact injury in the rat. Exp Neurol 161:15-26.

Post A, Hoshizaki TB, Gilchrist M, Brien S (2012) Analysis of the influence of independent variables used for reconstruction of a traumatic brain injury incident. P I Mech Eng P-J Spo 226:290-298.

Post A, Oeur A, Walsh E, Hoshizaki B, Gilchrist MD (2014) A centric/non-centric impact protocol and finite element model methodology for the evaluation of American football helmets to evaluate risk of concussion. Comput Methods Biomech Biomed Engin 17:1785-1800.

Prange MT, Margulies SS (2002) Regional, directional, and age-dependent properties of the brain undergoing large deformation. J Biomech Eng 124:244-252.

Properzi F, Lin R, Kwok J, Naidu M, van Kuppevelt TH, Ten Dam GB, Camargo LM, Raha-Chowdhury R, Furukawa Y, Mikami T, Sugahara K, Fawcett JW (2008) Heparan sulphate proteoglycans in glia and in the normal and injured CNS: expression of sulphotransferases and changes in sulphation. Eur J Neurosci 27:593-604.

Quagliarello VJ, Wispelwey B, Long WJ, Jr., Scheld WM (1991) Recombinant human interleukin-1 induces meningitis and blood-brain barrier injury in the rat. Characterization and comparison with tumor necrosis factor. J Clin Invest 87:1360-1366.

Raghupathi R, Conti AC, Graham DI, Krajewski S, Reed JC, Grady MS, Trojanowski JQ, McIntosh TK (2002) Mild traumatic brain injury induces apoptotic cell death in the cortex that is preceded by decreases in cellular Bcl-2 immunoreactivity. Neuroscience 110:605-616.

Raghupathi R, Muir JK, Fulp CT, Pittman RN, McIntosh TK (2003) Acute activation of mitogen-activated protein kinases following traumatic brain injury in the rat: implications for posttraumatic cell death. Exp Neurol 183:438-448.

Reeves TM, Colley BS (2012) Electrophysiological Approaches in Traumatic Brain Injury. In: Animal Models of Acute Neurological Injuries II (Chen, J. *et al.*, eds), pp 313-330: Humana Press.

Reeves TM, Lyeth BG, Phillips LL, Hamm RJ, Povlishock JT (1997) The effects of traumatic brain injury on inhibition in the hippocampus and dentate gyrus. Brain Res 757:119-132.

Reinert MM, Bullock R (1999) Clinical trials in head injury. Neurol Res 21:330-338.

Rho JY, Ashman RB, Turner CH (1993) Young's modulus of trabecular and cortical bone material: ultrasonic and microtensile measurements. J Biomech 26:111-119.

Ridet JL, Malhotra SK, Privat A, Gage FH (1997) Reactive astrocytes: cellular and molecular cues to biological function. Trends Neurosci 20:570-577.

Rink A, Fung KM, Trojanowski JQ, Lee VM, Neugebauer E, McIntosh TK (1995) Evidence of apoptotic cell death after experimental traumatic brain injury in the rat. Am J Pathol 147:1575-1583.

Robinson AP, Minev I, Graz IM, Lacour SP (2011) Microstructured silicone substrate for printable and stretchable metallic films. Langmuir 27:4279-4284.

Rodriguez Merzagora A, Izzetoglu M, Onaral B, Schultheis M (2014) Verbal working memory impairments following traumatic brain injury: an fNIRS investigation. Brain Imaging Behav 8:446-459.

Roitbak T, Sykova E (1999) Diffusion barriers evoked in the rat cortex by reactive astrogliosis. Glia 28:40-48.

Rolls A, Shechter R, Schwartz M (2009) The bright side of the glial scar in CNS repair. Nat Rev Neurosci 10:235-241.

Rosset S, Niklaus M, Dubois P, Shea HR (2009) Metal ion implantation for the fabrication of stretchable electrodes on elastomers. Adv Funct Mater 19:470-478.

Roth S, Raul JS, Willinger R (2010) Finite element modelling of paediatric head impact: global validation against experimental data. Comput Methods Programs Biomed 99:25-33.

Rowson S, Duma SM, Beckwith JG, Chu JJ, Greenwald RM, Crisco JJ, Brolinson PG, Duhaime AC, McAllister TW, Maerlender AC (2012) Rotational head kinematics in football impacts: an injury risk function for concussion. Ann Biomed Eng 40:1-13.

Saatman KE, Graham DI, McIntosh TK (1998) The neuronal cytoskeleton is at risk after mild and moderate brain injury. J Neurotrauma 15:1047-1058.

Sabet AA, Christoforou E, Zatlin B, Genin GM, Bayly PV (2008) Deformation of the human brain induced by mild angular head acceleration. J Biomech 41:307-315.

Salvemini D, Mollace V, Pistelli A, Anggard E, Vane J (1992) Cultured astrocytoma cells generate a nitric oxide-like factor from endogenous L-arginine and glyceryl trinitrate: effect of E. coli lipopolysaccharide. Br J Pharmacol 106:931-936.

Santhakumar V, Bender R, Frotscher M, Ross ST, Hollrigel GS, Toth Z, Soltesz I (2000) Granule cell hyperexcitability in the early post-traumatic rat dentate gyrus: the 'irritable mossy cell' hypothesis. J Physiol 524 Pt 1:117-134.

Sato M, Chang E, Igarashi T, Noble LJ (2001) Neuronal injury and loss after traumatic brain injury: time course and regional variability. Brain Res 917:45-54.

Savanthrapadian S, Wolff AR, Logan BJ, Eckert MJ, Bilkey DK, Abraham WC (2013) Enhanced hippocampal neuronal excitability and LTP persistence associated with reduced behavioral flexibility in the maternal immune activation model of schizophrenia. Hippocampus 23:1395-1409.

Scheff SW, Price DA (2006) Alzheimer's disease-related alterations in synaptic density: neocortex and hippocampus. Journal of Alzheimer's disease : JAD 9:101-115.

Schwartz TH, Rabinowitz D, Unni V, Kumar VS, Smetters DK, Tsiola A, Yuste R (1998) Networks of coactive neurons in developing layer 1. Neuron 20:541-552.

Schwarzbach E, Bonislawski DP, Xiong G, Cohen AS (2006) Mechanisms underlying the inability to induce area CA1 LTP in the mouse after traumatic brain injury. Hippocampus 16:541-550.

Sekitani T, Noguchi Y, Zschieschang U, Klauk H, Someya T (2008) Organic transistors manufactured using inkjet technology with subfemtoliter accuracy. Proc Natl Acad Sci U S A 105:4976-4980.

Sekitani T, Zschieschang U, Klauk H, Someya T (2010) Flexible organic transistors and circuits with extreme bending stability. Nat Mater 9:1015-1022.

Selassie AW, Zaloshnja E, Langlois JA, Miller T, Jones P, Steiner C (2008) Incidence of long-term disability following traumatic brain injury hospitalization, United States, 2003. J Head Trauma Rehabil 23:123-131.

Semple BD, Blomgren K, Gimlin K, Ferriero DM, Noble-Haeusslein LJ (2013) Brain development in rodents and humans: Identifying benchmarks of maturation and vulnerability to injury across species. Prog Neurobiol 106-107:1-16.

Sharp DJ, Scott G, Leech R (2014) Network dysfunction after traumatic brain injury. Nat Rev Neurol 10:156-166.

Sheiko SS, Xu H, Sun FC, Shirvanyants DG, Rubinstein M, Shabratov D, Beers KL, Matyjaszewski K (2007) Molecular pressure sensors. Adv Mater 19:2930-+.

Shih CY, Harder TA, Tai YC (2004) Yield strength of thin-film parylene-C. Microsyst Technol 10:407-411.

Shreiber DI, Bain AC, Ross DT, Smith DH, Gennarelli TA, McIntosh TK, Meaney DF (1999) Experimental investigation of cerebral contusion: histopathological and

immunohistochemical evaluation of dynamic cortical deformation. J Neuropathol Exp Neurol 58:153-164.

Sihver S, Marklund N, Hillered L, Langstrom B, Watanabe Y, Bergstrom M (2001) Changes in mACh, NMDA and GABA(A) receptor binding after lateral fluid-percussion injury: in vitro autoradiography of rat brain frozen sections. J Neurochem 78:417-423.

Silver J, Miller JH (2004) Regeneration beyond the glial scar. Nat Rev Neurosci 5:146-156.

Simon MJ, Gao S, Kang WH, Banta S, Morrison B, 3rd (2009) TAT-mediated intracellular protein delivery to primary brain cells is dependent on glycosaminoglycan expression. Biotechnol Bioeng 104:10-19.

Simon MJ, Kang WH, Gao S, Banta S, Iii BM (2011) TAT Is Not Capable of Transcellular Delivery Across an Intact Endothelial Monolayer In Vitro. Ann Biomed Eng 39:394-401.

Singh A, Lu Y, Chen C, Kallakuri S, Cavanaugh JM (2006) A new model of traumatic axonal injury to determine the effects of strain and displacement rates. Stapp Car Crash J 50:601-623.

Skandsen T, Finnanger TG, Andersson S, Lydersen S, Brunner JF, Vik A (2010) Cognitive impairment 3 months after moderate and severe traumatic brain injury: a prospective follow-up study. Arch Phys Med Rehabil 91:1904-1913.

Sloviter RS (1991) Feedforward and feedback inhibition of hippocampal principal cell activity evoked by perforant path stimulation: GABA-mediated mechanisms that regulate excitability in vivo. Hippocampus 1:31-40.

Sloviter RS (1994) On the relationship between neuropathology and pathophysiology in the epileptic hippocampus of humans and experimental animals. Hippocampus 4:250-253.

Smith-Thomas LC, Fok-Seang J, Stevens J, Du JS, Muir E, Faissner A, Geller HM, Rogers JH, Fawcett JW (1994) An inhibitor of neurite outgrowth produced by astrocytes. J Cell Sci 107 (Pt 6):1687-1695.

Snow AD, Mar H, Nochlin D, Sekiguchi RT, Kimata K, Koike Y, Wight TN (1990) Early accumulation of heparan sulfate in neurons and in the beta-amyloid protein-containing lesions of Alzheimer's disease and Down's syndrome. Am J Pathol 137:1253-1270.

Sofroniew MV (2005) Reactive astrocytes in neural repair and protection. Neuroscientist 11:400-407.

Sorg SF, Delano-Wood L, Luc N, Schiehser DM, Hanson KL, Nation DA, Lanni E, Jak AJ, Lu K, Meloy MJ, Frank LR, Lohr JB, Bondi MW (2014) White matter integrity in veterans with mild traumatic brain injury: associations with executive function and loss of consciousness. J Head Trauma Rehabil 29:21-32.

Sosin DM, Sniezek JE, Waxweiler RJ (1995) Trends in death associated with traumatic brain injury, 1979 through 1992. Success and failure. JAMA 273:1778-1780.

Spaepen F (2000) Interfaces and stresses in thin films. Acta Mater 48:31-42.

Spigolon G, Veronesi C, Bonny C, Vercelli A (2010) c-Jun N-terminal kinase signaling pathway in excitotoxic cell death following kainic acid-induced status epilepticus. Eur J Neurosci 31:1261-1272.

Staiger JF, Kotter R, Zilles K, Luhmann HJ (2000) Laminar characteristics of functional connectivity in rat barrel cortex revealed by stimulation with caged-glutamate. Neurosci Res 37:49-58.

Stam CJ, de Haan W, Daffertshofer A, Jones BF, Manshanden I, van Cappellen van Walsum AM, Montez T, Verbunt JP, de Munck JC, van Dijk BW, Berendse HW, Scheltens P (2009) Graph theoretical analysis of magnetoencephalographic functional connectivity in Alzheimer's disease. Brain 132:213-224.

Stam CJ, Jones BF, Nolte G, Breakspear M, Scheltens P (2007) Small-world networks and functional connectivity in Alzheimer's disease. Cereb Cortex 17:92-99.

Stanford IM, Wheal HV, Chad JE (1995) Bicuculline enhances the late GABAB receptor-mediated paired-pulse inhibition observed in rat hippocampal slices. Eur J Pharmacol 277:229-234.

Stichel CC, Muller HW (1998) The CNS lesion scar: new vistas on an old regeneration barrier. Cell Tissue Res 294:1-9.

Stirling DP, Liu J, Plunet W, Steeves JD, Tetzlaff W (2008) SB203580, a p38 mitogen-activated protein kinase inhibitor, fails to improve functional outcome following a moderate spinal cord injury in rat. Neuroscience 155:128-137.

Stoica BA, Faden AI (2010) Cell death mechanisms and modulation in traumatic brain injury. Neurotherapeutics 7:3-12.

Su JH, Cummings BJ, Cotman CW (1992) Localization of heparan sulfate glycosaminoglycan and proteoglycan core protein in aged brain and Alzheimer's disease. Neuroscience 51:801-813.

Subbaroyan J, Martin DC, Kipke DR (2005) A finite-element model of the mechanical effects of implantable microelectrodes in the cerebral cortex. J Neural Eng 2:103-113.

Sun W, Dan Y (2009) Layer-specific network oscillation and spatiotemporal receptive field in the visual cortex. Proc Natl Acad Sci U S A 106:17986-17991.

Sun YG, Wang HH (2007) High-performance, flexible hydrogen sensors that use carbon nanotubes decorated with palladium nanoparticles. Adv Mater 19:2818-+.

Sundstrom L, Morrison B, 3rd, Bradley M, Pringle A (2005) Organotypic cultures as tools for functional screening in the CNS. Drug Discov Today 10:993-1000.

Suo Z, Ma EY, Gleskova H, Wagner S (1999) Mechanics of rollable and foldable film-on-foil electronics. Appl Phys Lett 74:1177-1179.

Sze CI, Troncoso JC, Kawas C, Mouton P, Price DL, Martin LJ (1997) Loss of the presynaptic vesicle protein synaptophysin in hippocampus correlates with cognitive decline in Alzheimer disease. J Neuropathol Exp Neurol 56:933-944.

Takhounts EG, Eppinger RH, Campbell JQ, Tannous RE, Power ED, Shook LS (2003) On the development of the SIMon finite element head model. Stapp Car Crash J 47:107-133.

Takhounts EG, Ridella SA, Hasija V, Tannous RE, Campbell JQ, Malone D, Danelson K, Stitzel J, Rowson S, Duma S (2008) Investigation of traumatic brain injuries using the next generation of simulated injury monitor (SIMon) finite element head model. Stapp Car Crash J 52:1-31.

Tavalin SJ, Ellis EF, Satin LS (1997) Inhibition of the electrogenic Na pump underlies delayed depolarization of cortical neurons after mechanical injury or glutamate. J Neurophysiol 77:632-638.

Thibault KL, Margulies SS (1998) Age-dependent material properties of the porcine cerebrum: effect on pediatric inertial head injury criteria. J Biomech 31:1119-1126.

Thiebaud P, Beuret C, Koudelka-Hep M, Bove M, Martinoia S, Grattarola M, Jahnsen H, Rebaudo R, Balestrino M, Zimmer J, Dupont Y (1999) An array of Pt-tip microelectrodes for extracellular monitoring of activity of brain slices. Biosens Bioelectron 14:61-65.

Topp KS, Boyd BS (2006) Structure and biomechanics of peripheral nerves: nerve responses to physical stresses and implications for physical therapist practice. Phys Ther 86:92-109.

Toy D, Namgung U (2013) Role of glial cells in axonal regeneration. Exp Neurobiol 22:68-76.

Tsay C, Lacour SP, Wagner S, Morrison B (2005) Architecture, fabrication, and properties of stretchable micro-electrode arrays. Proc 4th IEEE Conf Sensors 1169-1172.

Tsirka V, Simos PG, Vakis A, Kanatsouli K, Vourkas M, Erimaki S, Pachou E, Stam CJ, Micheloyannis S (2011) Mild traumatic brain injury: graph-model characterization of brain networks for episodic memory. Int J Psychophysiol 79:89-96.

Tsujimoto S (2008) The prefrontal cortex: functional neural development during early childhood. Neuroscientist 14:345-358.

Tyagi M, Rusnati M, Presta M, Giacca M (2001) Internalization of HIV-1 tat requires cell surface heparan sulfate proteoglycans. J Biol Chem 276:3254-3261.

Ughrin YM, Chen ZJ, Levine JM (2003) Multiple regions of the NG2 proteoglycan inhibit neurite growth and induce growth cone collapse. J Neurosci 23:175-186.

van Bergen A, Papanikolaou T, Schuker A, Moller A, Schlosshauer B (2003) Long-term stimulation of mouse hippocampal slice culture on microelectrode array. Brain Res Brain Res Protoc 11:123-133.

Verna JM, Fichard A, Saxod R (1989) Influence of glycosaminoglycans on neurite morphology and outgrowth patterns in vitro. Int J Dev Neurosci 7:389-399.

Vespa PM, Nuwer MR, Nenov V, Ronne-Engstrom E, Hovda DA, Bergsneider M, Kelly DF, Martin NA, Becker DP (1999) Increased incidence and impact of nonconvulsive and convulsive seizures after traumatic brain injury as detected by continuous electroencephalographic monitoring. J Neurosurg 91:750-760.

Viano DC, Casson IR, Pellman EJ, Zhang L, King AI, Yang KH (2005) Concussion in professional football: brain responses by finite element analysis: part 9. Neurosurgery 57:891-916; discussion 891-916.

Viskontas IV, Knowlton BJ, Steinmetz PN, Fried I (2006) Differences in mnemonic processing by neurons in the human hippocampus and parahippocampal regions. J Cogn Neurosci 18:1654-1662.

Vives E, Brodin P, Lebleu B (1997) A truncated HIV-1 Tat protein basic domain rapidly translocates through the plasma membrane and accumulates in the cell nucleus. J Biol Chem 272:16010-16017.

Wada K, Chatzipanteli K, Busto R, Dietrich WD (1998a) Role of nitric oxide in traumatic brain injury in the rat. J Neurosurg 89:807-818.

Wada K, Chatzipanteli K, Kraydieh S, Busto R, Dietrich WD (1998b) Inducible nitric oxide synthase expression after traumatic brain injury and neuroprotection with aminoguanidine treatment in rats. Neurosurgery 43:1427-1436.

Waetzig V, Czeloth K, Hidding U, Mielke K, Kanzow M, Brecht S, Goetz M, Lucius R, Herdegen T, Hanisch UK (2005) c-Jun N-terminal kinases (JNKs) mediate pro-inflammatory actions of microglia. Glia 50:235-246.

Walker GC, Sun YJ, Akhremitchev B (2004) Using the adhesive interaction between atomic force microscopy tips and polymer surfaces to measure the elastic modulus of compliant samples. Langmuir 20:5837-5845.

Walker WC, Pickett TC (2007) Motor impairment after severe traumatic brain injury: A longitudinal multicenter study. J Rehabil Res Dev 44:975-982.

Wang W, Xu TL (2006) Chloride homeostasis differentially affects GABA(A) receptor- and glycine receptor-mediated effects on spontaneous circuit activity in hippocampal cell culture. Neurosci Lett 406:11-16.

Wang XJ (2001) Synaptic reverberation underlying mnemonic persistent activity. Trends Neurosci 24:455-463.

Wanner IB, Deik A, Torres M, Rosendahl A, Neary JT, Lemmon VP, Bixby JL (2008) A new in vitro model of the glial scar inhibits axon growth. Glia 56:1691-1709.

Watts DJ, Strogatz SH (1998) Collective dynamics of 'small-world' networks. Nature 393:440-442.

Welch KM, D'Andrea G, Tepley N, Barkley G, Ramadan NM (1990) The concept of migraine as a state of central neuronal hyperexcitability. Neurologic clinics 8:817-828.

Williams JC, Rennaker RL, Kipke DR (1999) Long-term neural recording characteristics of wire microelectrode arrays implanted in cerebral cortex. Brain Res Brain Res Protoc 4:303-313.

Williams R, Yao H, Dhillon NK, Buch SJ (2009) HIV-1 Tat co-operates with IFN-gamma and TNF-alpha to increase CXCL10 in human astrocytes. PLoS One 4:e5709.

Willinger R, Kang HS, Diaw B (1999) Three-dimensional human head finite-element model validation against two experimental impacts. Ann Biomed Eng 27:403-410.

Witgen BM, Lifshitz J, Smith ML, Schwarzbach E, Liang SL, Grady MS, Cohen AS (2005) Regional hippocampal alteration associated with cognitive deficit following experimental brain injury: a systems, network and cellular evaluation. Neuroscience 133:1-15.

Wright RM, Ramesh KT (2012) An axonal strain injury criterion for traumatic brain injury. Biomech Model Mechanobiol 11:245-260.

Wu JY, Guan L, Bai L, Yang Q (2001) Spatiotemporal properties of an evoked population activity in rat sensory cortical slices. J Neurophysiol 86:2461-2474.

Wu JY, Guan L, Tsau Y (1999) Propagating activation during oscillations and evoked responses in neocortical slices. J Neurosci 19:5005-5015.

Yamada A, Uesaka N, Hayano Y, Tabata T, Kano M, Yamamoto N (2010) Role of pre- and postsynaptic activity in thalamocortical axon branching. Proc Natl Acad Sci U S A 107:7562-7567.

Yang S, Zhang D, Yang Z, Hu X, Qian S, Liu J, Wilson B, Block M, Hong JS (2008) Curcumin protects dopaminergic neuron against LPS induced neurotoxicity in primary rat neuron/glia culture. Neurochem Res 33:2044-2053.

Yao J, Yang J, Otte D (2007) Head injuries in child pedestrian accidents--in-depth case analysis and reconstructions. Traffic Inj Prev 8:94-100.

Yi JH, Katagiri Y, Susarla B, Figge D, Symes AJ, Geller HM (2012) Alterations in sulfated chondroitin glycosaminoglycans following controlled cortical impact injury in mice. J Comp Neurol 520:3295-3313.

Yoo BK, Choi JW, Shin CY, Jeon SJ, Park SJ, Cheong JH, Han SY, Ryu JR, Song MR, Ko KH (2008) Activation of p38 MAPK induced peroxynitrite generation in LPS plus IFN-gamma-stimulated rat primary astrocytes via activation of iNOS and NADPH oxidase. Neurochem Int 52:1188-1197.

Young PR, McLaughlin MM, Kumar S, Kassis S, Doyle ML, McNulty D, Gallagher TF, Fisher S, McDonnell PC, Carr SA, Huddleston MJ, Seibel G, Porter TG, Livi GP, Adams JL, Lee JC (1997) Pyridinyl imidazole inhibitors of p38 mitogen-activated protein kinase bind in the ATP site. J Biol Chem 272:12116-12121.

Yu AC, Lee YL, Eng LF (1991) Inhibition of GFAP synthesis by antisense RNA in astrocytes. J Neurosci Res 30:72-79.

Yu AC, Lee YL, Eng LF (1993) Astrogliosis in culture: I. The model and the effect of antisense oligonucleotides on glial fibrillary acidic protein synthesis. J Neurosci Res 34:295-303.

Yu Z, Graudejus O, Tsay C, Lacour SP, Wagner S, Morrison B, 3rd (2009a) Monitoring hippocampus electrical activity in vitro on an elastically deformable microelectrode array. J Neurotrauma 26:1135-1145.

Yu Z, Graudejus O, Tsay C, Lacour SP, Wagner S, Morrison III B (2009b) Monitoring hippocampus electrical activity in vitro on an elastically deformable microelectrode array. J Neurotrauma 26:1135-1145.

Yu Z, McKnight TE, Ericson MN, Melechko AV, Simpson ML, Morrison B, 3rd (2007) Vertically aligned carbon nanofiber arrays record electrophysiological signals from hippocampal slices. Nano Lett 7:2188-2195.

Yu Z, Morrison B, 3rd (2010) Experimental mild traumatic brain injury induces functional alteration of the developing hippocampus. J Neurophysiol 103:499-510.

Yuste R, Peinado A, Katz LC (1992) Neuronal domains in developing neocortex. Science 257:665-669.

Zhang H, Uchimura K, Kadomatsu K (2006) Brain keratan sulfate and glial scar formation. Ann N Y Acad Sci 1086:81-90.

Zhang L, Rzigalinski BA, Ellis EF, Satin LS (1996) Reduction of voltage-dependent Mg2+ blockade of NMDA current in mechanically injured neurons. Science 274:1921-1923.

Zhang L, Yang KH, Dwarampudi R, Omori K, Li T, Chang K, Hardy WN, Khalil TB, King AI (2001a) Recent advances in brain injury research: a new human head model development and validation. Stapp Car Crash J 45:369-394.

Zhang L, Yang KH, King AI (2001b) Comparison of brain responses between frontal and lateral impacts by finite element modeling. J Neurotrauma 18:21-30.

Zhang L, Yang KH, King AI (2004) A proposed injury threshold for mild traumatic brain injury. J Biomech Eng 126:226-236.

Zhao X, Ahram A, Berman RF, Muizelaar JP, Lyeth BG (2003) Early loss of astrocytes after experimental traumatic brain injury. Glia 44:140-152.

Zheng F, He CQ, Fang PF, Wang JG, Xiong BY, Wang K, Liu FW, Peng XY, Xu XG, Xu ZH, Wang SJ (2013) The surface structure of UV exposed poly-dimethylsiloxane (PDMS) insulator studied by slow positron beam. Appl Surf Sci 283:327-331.

Zhu Z, Zhang Q, Yu Z, Zhang L, Tian D, Zhu S, Bu B, Xie M, Wang W (2007) Inhibiting cell cycle progression reduces reactive astrogliosis initiated by scratch injury in vitro and by cerebral ischemia in vivo. Glia 55:546-558.

Zucker RS (1989) Short-term synaptic plasticity. Annu Rev Neurosci 12:13-31.